Nanowire Arrays and 3D Porous Conducting Networks for Li-Ion Battery Electrodes

by

Miao Tian

B.S., Xi'an Jiaotong University, China, 2007

M.S., University of Colorado at Boulder, 2010

A thesis

Submitted to the Faculty of

the Graduate School of the University of Colorado

in partial fulfillment of the requirements for the degree of

Doctor of Philosophy

Department of Mechanical Engineering

April 2014

This thesis entitled:

Nanowire Arrays and 3D Porous Conducting Networks for Li-Ion Battery Electrodes

written by Miao Tian

has been approved for the Department of Mechanical Engineering

_____

(Professor Ronggui Yang, Chair)

_____

(Professor Se-Hee Lee)

Date_____

The final copy of this thesis has been examined by the signatories, and we

Find that both the content and the form meet acceptable presentation standards

Of scholarly work in the above mentioned discipline.

Abstract

Tian, Miao (Ph.D., Department of Mechanical Engineering)

Nanowire Electrodes and 3D Porous Conducting Networks for Li-Ion Batteries

Thesis directed by Associate Professor Ronggui Yang

There have been growing interests in developing high-capacity, high-power, and long-cycle-life lithium-ion (Li-ion) batteries due to the increasing power requirements of portable electronics and electrical vehicles. Various efforts have been made to utilize nano-structured electrodes since they can improve the performance of Li-ion batteries compared to bulk materials in many ways: fast electrode reaction due to the large surface area, efficient volume-change accommodation due to the small size, and fast Li-ion transport along the nanoscale gaps. Among various nanostructures, nanowire arrays present an excellent candidate for high performance lithium-ion battery electrodes, which have attracted intensive research over the past few years. However, problems such as the strain mismatch at the active/inactive material interface (A/I interface) and the agglomeration of nanowires hinder nanowire array-based electrodes from delivering superior battery performance. We found that the formation of a continuous Ni-Sn film at the base of the nanowires results in quick loss of electrical contact between the active material and the current collector because of the large strain mismatch at the large continuous A/I interface. By growing short Cu nanorods as a buffer layer before Ni-Sn nanowire growth, the formation of Ni-Sn film was inhibited and the A/I interface was scaled down to nanoscale islands. The strain mismatch is thus significantly reduced, which results in enhanced structural stability and the battery performance.

Another problem with nanowire array electrodes is that agglomeration in long nanowire arrays impedes them from delivering high areal capacity, by degrading the nanoscale wires to micron-sized bundles and reducing the mechanical stability. We develop a simple way to fabricate three-dimensional (3D) Ni-Sn nanowire networks by using 3D porous anodic alumina (PAA) templates synthesized from low-cost impure aluminum foils. By eliminating agglomeration, stable high-areal-capacity anodes are demonstrated with 3D self-supporting Ni-Sn nanowire network structures. With a nanowire length of 40 μm, the 3D Ni-Sn nanowire networks can deliver an areal capacity as high as 4.3 mAh cm^{-2} with a cycle life longer than 50 cycles when used as an electrode.

The 3D network has been envisioned as a superior electrode architecture of Li-ion batteries that can significantly enhance both ion and electron transport to improve battery performance. A 3D carbon nano-network is fabricated through chemical vapor deposition of carbon on a 3D PAA template, which serves as the conducting framework in Li-ion battery electrodes. The low conductivity active material, TiO_2, is then uniformly coated on the surfaces of the 3D carbon nano-network using atomic layer deposition. A large areal capacity of ~ 0.37 mAh cm^{-2} is achieved due to the large areal mass loading of the 3D C/TiO_2 electrodes. The electrodes also deliver a high gravimetric capacity of ~ 240 mAh g^{-1} based on the whole electrode at the test rate of C/5 and a long cycle life of over 1000 cycles at 1C. The effects of the electrical conductivity of carbon nano-network, ion transport in the active material, and the electrolyte permeability on the rate performance of these 3D C/TiO_2 electrodes are also systematically studied.

Keywords: Nanowire, Li-ion battery, active/inactive material interface, three-dimensional nano-network, carbon

Acknowledgements

I would like to thank Professor Ronggui Yang, Professor Yung-Cheng Lee, Professor Se-Hee Lee, Professor Kurt Maute, and Professor Steven M. George for their patience and commitment when serve as my thesis committee members. Advices with their expertise and insights are valuable for my current and future research.

In particular, I would like to express my gratefulness to my advisor Prof. Ronggui Yang for the guidance and support. Many thanks for the opportunity to work on this interesting and challenging project so that I learned how to be a great scholar and a great team player. Your great expertise and knowledge as well as your enthusiasm and passion for work will always enlighten my future life and career.

I would like to thank all of my labmates and friends at University of Colorado Boulder. You have been an excellent source of support, encouragement, and motivation, especially at tough times.

Contents

List of Tables

List of Figures

1. Introduction

1.1 Motivation

The global demand for energy is continuously on the rise. In the present scenario, most of the energy is obtained from non-renewable fossil resources such as coal, oil and natural gas. However, the dwindling oil and natural gas supplies and alleviated environmental concerns of global warming due to the use of fossil fuels require efforts in developing and utilizing renewable energy sources. The renewable energy sources such as solar and wind are intermittent and thus need a suitable energy storage technology to integrate them into our existing power grid. Compared with traditional secondary cells such as lead acid, nickel cadmium, and nickel metal hydroxide batteries, lithium-ion (Li-ion) batteries (LIBs) have become the leading energy source for various applications from smartphones and laptops to electric vehicles [1-4], benefited from their superior performance including high operating voltage, high energy, and high power density [5-11]. Figure **1.1** shows performance comparison of LIBs with other rechargeable batteries[1]. The major problem of using conventional batteries such as lead-acid and Ni-Cd batteries as power sources for portable electronics or electric vehicles is their low specific energy densities. This low specific energy density limits their portability. When the batteries are scaled up for high-energy use such as that in electric vehicles, heating could become a problem when packaging a large number of electrochemical cells together. High performance Li-ion batteries are in great need since its development drops behind related industries such as portable consumer electronic devices, implantable medical applications, storage of wind/solar power, and electric vehicles.

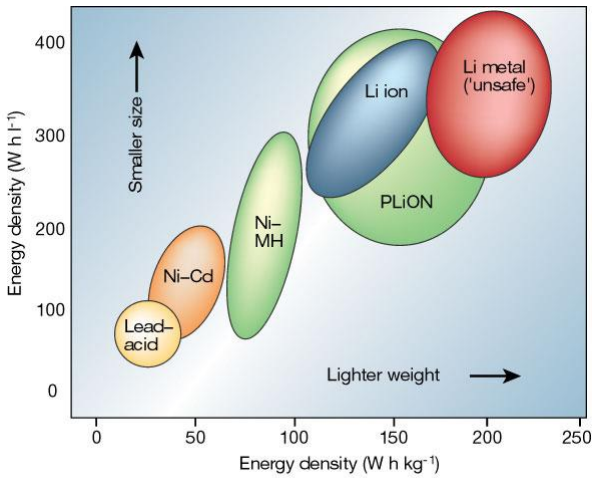

Figure 1.1 Comparison of the volumetric and gravimetric energy densities of different battery technologies [1].

Each LIB cell generally consists of four components as shown in Figure **1.2**: 1) The anode/negative electrode/reducing electrode, which gives up electrons to the external circuit and is oxidized during the electrochemical reaction. 2) The cathode/positive electrode/oxidizing electrode, which accepts electrons from the external circuit and is reduced during electrochemical reaction. 3) The electrolyte or the ionic conductor and electron insulator, which provides the medium for transfer of ions inside the cell between the anode and cathode. 4) The separator, which is a porous sheet that keeps the positive and negative electrodes apart. The anode is usually composed of lithium metal or lithium insertion/conversion compounds, whereas the cathode is made up of another Li^+ host materials possessing a much more positive redox potential [12]. The electrolyte is typically a liquid (an organic solvent, such as EC-DMC), with dissolved salts (such as $LiPF_6$) to impart ionic conductivity.

Rechargeable LIBs involve the exchange of lithium ions between two electrodes upon charging and discharging. Figure **1.2** demonstrates the operation principle of traditional

rechargeable Li-ion batteries. The lithium insertion and extraction processes occur with an ion flow through the electrolyte, accompanied by a reduction and oxidation (redox) reaction of the host matrix and the electron flow through an external circuit. This is called a "rocking-chair" design because the Li ions "rock" back and forth between the two electrodes. Li is the most favorable mobile ion species for batteries since it is the lightest of all metals and has the greatest electrochemical potential, providing the largest energy density per weight.

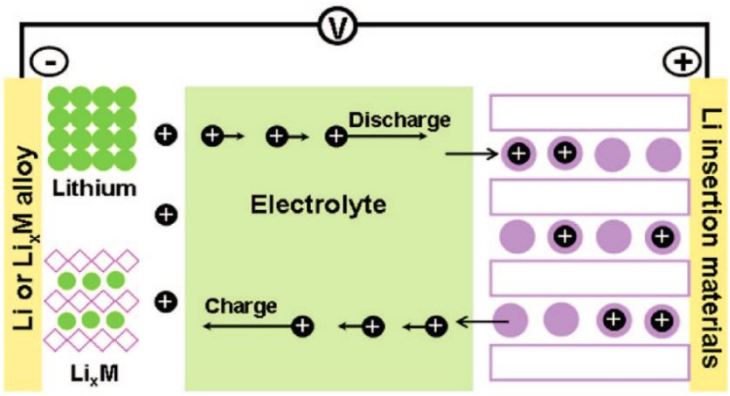

Figure 1.2 Schematic showing the operation principle of a rechargeable Li-ion batteries [4].

Currently, lithium-ion batteries use graphite as anode for reversible lithium intercalation and disintercalation. Lithium intercalates into the carbon layer to form Li_xC alloy, delivering a theoretical specific capacity of 372 mAh g^{-1} (LiC6) and a potential plateau lower than 0.5 V vs Li+/Li [13]. Despite the stability of carbon anode, the low theoretical capacity limits the development of high capacity Li-ion batteries. As typical cathode materials, lithiated transition metal oxides such as $LiCoO_2$ possess 2D layered crystal structure and exhibits high voltage approaching 4 V *vs.* Li metal [12]. But their low specific capacity (lower than 200 mAh g^{-1}), slow Li-ion transport, and low electrical conductivity drag down the performance of the whole batteries.

Nanostructured electrodes have great potential in significantly improving the performance of rechargeable Li-ion batteries. Among various nanostructures, nanowire electrodes have recently attracted great interests [14-16]. Many features of nanowires lead to significant improvements in battery performance: (1) the free spaces between nanowires provide easy access of the electrolyte to all the surfaces of the electrode and accommodate volume changes during lithium ion insertion; (2) the small diameter of nanowires allows for fast Li-ion diffusion and high power delivery; (3) direct connection of nanowires to the current collector ensures direct transportation of electrons to the current collector, which eliminates the necessity of any binder materials or conducting additives [17, 18]. Electrodes with nanowires of various materials such as Si, TiO_2, Fe_3O_4, SnO_2, Co_3O_4, and V_2O_5 [17],[19-23] have been studied and show improved performance compared to bulk electrodes.

However, nanowire electrodes are facing two critical problems. First, the interface between the active material and inactive material is not stable due to the strain mismatch during the battery cycling processes. The active materials expand and contract when Li ions are inserted into and extracted from them. On the other hand, the volume of current collector which is inactive does not change. The stress generated at the active/inactive material interface (A/I interface) would lead to delamination of the active material. The delaminated active material cannot contribute to the electrode performance anymore since the electrical connection to the system is cut off. Second problem with nanowire electrodes is agglomeration of long nanowires. The areal capacity of straight nanowire array electrodes could potentially be increased by increasing the length of the nanowires [24]. However, the high aspect ratio of long nanowires leads to severe agglomeration, which significantly degrades the electrochemical performance of

nanowire array electrodes due to the reduced surface area, blocked Li-ion diffusion, and the increased stress in the agglomerated nanowire arrays.

The interface between the active material and the inactive current collector has been found important for electrodes by many researchers. It has been shown that failure of Si film anode is due to delaminating of Si film from the Cu substrate, isolating the electronic pathways of Si to the underlying Cu [25]. Similar phenomenon was observed for Sn alloy films [26]. Annealing and modification of current collector surfaces could improve the adhesion between the active material and the current collector and thus make the reversible capacity high and stable [27-29]. On the other hand, battery stability can also be improved by scaling down the heterogeneous interface of Si and carbon nanotubes [30]. The critical role of the active/inactive material interfaces (A/I interfaces) in electrodes can be systematically studied using nanowires since their unique structure offers a way to tailor the A/I interface.

Three-dimensional (3D) micro/nanostructured networks present great benefits for high performance LIBs, such as a large surface area for fast Li ion insertion/extraction, interconnecting paths for fast electron conduction, and high porosity for fast electrolyte diffusion and volume change alleviation [31, 32]. High areal capacity and excellent rate performance have been achieved by incorporating 3D metal conducting networks with active materials [33-38]. However, the use of metallic conducting networks in these 3D electrodes comes with the intrinsic penalty of heavy inactive materials, which significantly reduces the gravimetric capacity in LIBs. Thus, 3D porous carbon, which has low mass density with interpenetrating network that facilitates both ion and electron transport, has been widely explored to overcome the density barrier [39-46]. Carbon aerogels are a kind of porous carbon consisting of meso-pores with a size of <10 nm, which offer very high surface areas for LIB and supercapacitors [39, 47-50]. The

diffusion of the electrolyte and transport of ions are greatly impeded due to the small pores in carbon aerogels, especially when the electrodes are thicker than 10 μm [51], which greatly harms the rate capability of the electrodes [52-54]. For example, mesoporous carbon/Co_3O_4 composite maintained only 32% of its capacity when the test current was increased by 10 times from 200 mA g^{-1} to 2000mA g^{-1} [54]. As such, porous carbon with large pore sizes (> 1 μm) were developed to introduce more porosity to the carbon network and to improve the rate capability of electrodes [55, 56]. A $LiFePO_4$/carbon composite electrode with 1 μm to 5μm pores retained 89% of its capacity when the test rate was increased by 10 times from C/10 to 1C [57, 58]. However, accompanying the improved power performance in these electrodes, the overall volumetric capacity and energy density of such electrodes are greatly reduced due to the large size of the pores and the thin active materials, which leaves most space in the electrodes empty.

A low mass density conducting network with pore size in the range of hundreds of nanometers needed to enhance the ion and electron transport without sacrificing energy density. Some efforts have been made to develop 3D conducting networks with pore size in the range of several hundred nanometers. Porous carbon with pore size of ~ 300 nm encapsulating sulfur retained 52% of its capacity when test rate was increased by 10 times from C/5 to 2C [59]. Nanoparticles entrapped in carbon inverse opal with 220 nm diameter pores maintained 50% of the capacity when the test current increased 10 times from 1 $A \cdot g^{-1}$ to 10 $A \cdot g^{-1}$ [60]. All these previous efforts demonstrate the importance of the 3D carbon network with appropriate pore size in the LIB electrodes.

1.2 Background overview

1.2.1 Anode materials

1.2.1.1 Carbonaceous Materials

Carbonaceous-based materials are the most attractive and widely investigated materials for use as anode in Li-ion batteries [61]. This has been mainly because of the high specific charges, the low cost, high safety, low redox potentials (~ 0.1 V vs. Li/Li+), and good cycling stability. With Li ions inserted, graphite forms LiC_6, which corresponding to a theoretical capacity of 373 mAh g^{-1}[62]. In other forms of carbon such as disordered carbon [63], carbon nanotube [64], and graphene [65], the specific capacities are higher because they have more sites for Li ion insertion. The insertion of Li ions into carbon is called *intercalation*, which means the insertion of a guest species into a host structure without causing any major structural distortion [61]. Since the crystal structure of carbon doesn't distort during Li ion intercalation, carbon can perform very long cycling life as anode of Li-ion batteries.

Although graphitic carbon is the major commercially available anode material, its specific capacity limits further development of Li-ion batteries. There are several ways have been developed to improve performance of carbon based anode electrode such as mild oxidation of graphite and composites with metals and metal oxides [66]. However, these methods can only to a limited scale. Anode materials with higher specific capacity are intensely needed to develop high-energy Li-ion batteries.

Carbon aerogels having large amounts of mesopores were prepared mostly by pyrolysis of the aerogels of resorcinol and formaldehyde [47]. Primary particles of carbon aerogels have

usually the size of about 4–9 nm and interconnected with each other to form a network, forming inter-particle mesopores. Pore size distributions in carbon aerogel (or carbon nanofoam) is in a large range but can be hardly tuned. As most of the pores are small (<10nm), flow resistance of electrolyte in the electrode is large. Power performance of the electrode would be limited. Moreover, the amount of the active materials can be loaded is limited by the small available space. Thus the capacity of the electrode would be low.

As one kind of porous carbon materials, carbon nanotubes (CNTs) and graphene have been extensively investigated as anode materials for Li-ion batteries due to their mesoporous character (higher electrode/electrolyte contact area leading to higher charge/discharge rates), high chemical stability, low resistance (short path lengths for electronic and Li^+ transport), strong mechanical strength, and high activated surfaces (better accommodation of the strain of Li+ insertion/removal, improving cycle life) [67-69]. The most direct way to improve the capacity of the CNT anodes is to fabricate composite electrodes of CNTs with other materials. In such hybrid systems, the CNTs function as an effective confining buffer of mechanical stress induced by volume changes in charging and discharging reactions, while the other nanomaterials provide a high capacity. [70, 71] Three-dimensional (3D) graphene-based hybrid structures were fabricated to improve the storage capacity of Li-ion batteries by increased specific surface area and more suitable layer spacing of graphene sheets. Some metal oxides, CNTs, fullerenes (C60), carbon nanofibers, and even organic agents could be introduced to fabricate 3D-structured grapheme. [72]

1.2.1.2 Silicon Based Materials

Since it has the highest known theoretical capacity (4200 mAh g−1), silicon would seem to be a superior anode material for high-energy-density Li-ion secondary cells. However severe

capacity fade during initial cycling has been found to be a limiting issue for Si anodes[73]. There are various approaches developed to overcome drawbacks of pure silicon and improve its electrochemical perfomance:

1. Reduce dimension of pure Si to micro- and nano-scale to decrease pulverization of Si results from anode's volume increase during Li-insertion and its shrinkage during extraction. A widely studied method is to reduce the Si particle size to nano-scale[74]. To improve electronic contact between particles during insertion and extraction, mixing conductive additives (CA) such as graphite flakes and/or nano-scale carbon black into micro-Si anodes is adopted[75]. While particle size reduction can reduce volume change to a certain degree, it cannot completely eliminate capacity fade. Therefore, other nanostructures such as nanoporous structure, nanowires, and nanotubes are studied.

2. Si dispersed in an inactive matrix. An inactive matrix used in the anode acts as a cushion and helps accommodate the volume change, thereby preventing pulverization of the anode. This inactive matrix must have a high mechanical strength to withstand the volume change of Si on cycling. Ideally, it should also have high electronic conductivity to allow charge transfer reactions to take place. Metallic compounds such as TiN [76], TiB2[77], SiC [78], and TiC[79] have been examined for this purpose as inactive host matrices.

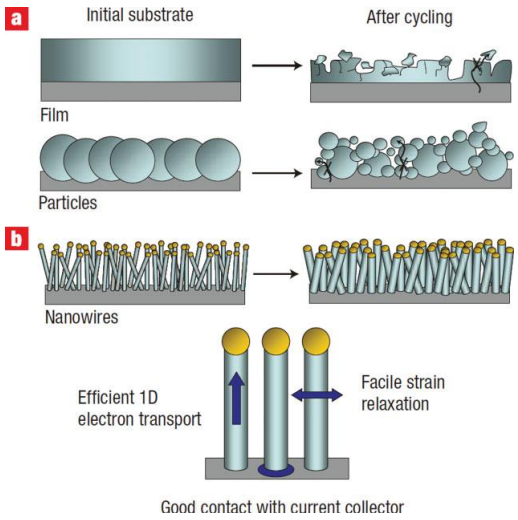

Figure 1.3 Schematic of morphological changes that occur in Si during electrochemical cycling. (a) Si films and particles tend to pulverize during cycling due to the volume change. (b) Si nanowires grown directly on the current collector do not pulverize or break into smaller particles after cycling [80].

3. Si dispersed in an active matrix. Active materials like silver and magnesium can reversibly react anodically with Li+ at room temperature and form alloys, but have little volume change during cycling. Mg_2Si alloy, for example was investigated as an anode material[81], which has several characteristics which make it an attractive candidate for lithium storage: First, lithium can be inserted electrochemically into magnesium, silicon and their alloy at room temperature[82], respectively. Second, both elements are naturally abundant and inexpensive. Third, large specific capacities may be achievable because both elements are light-weight. SiAg anodes prepared by ball milling Si and Ag for 2, 15, and 50 h have also been examined[83] and showed promising performance.

Since even relatively strong metals may not be able to sustain the 400% volume expansion of Si, and their pulverization will result in loss of interparticle electronic contact, carbon has

been used as an active matrix because of its softness and compliance, relatively low mass, good electronic conductivity, reasonable Li-insertion ability, and small volume expansion.[84]

1.2.1.3 Sn Based Materials

It has been shown that tin and tin-based materials are promising candidates to replace the carbon-based anode materials for Li-ion batteries because of their large theoretical capacity for lithium insertion (i.e., 990 mA h g-1, supposed the formation of Li4.4Sn alloy) and safety benefit for avoiding the formation of hazardous Li dendrite [85]. Besides the fact that pure Tin has very high specific charge, tin oxides, tin oxides and tin alloys are also potential for application in Li-ion batteries. Although their specific charge is not at high as pure tin, their structures help accommodate volume change during cycling process, improving cycling stability[86], as shown in Table **1.1**.

Table 1.1 Theoretical specific charges (with respect to the masses of the lithiated anode materials) and estimated practical cycling stabilities of various tin oxides and tin-based multiphase and composite hosts in comparison to metallic Sn and graphite[87] .

Anode material	Lithiated anode material	Specific charge (A h kg^{-1})	Practical cycling stability[c]
Graphite (C_6)	LiC_6	339.2	good
Sn	$Li_{4.4}Sn$	790.2	poor
SnO	$Li_{4.4}Sn/Li_2O$	658.4	fair
SnO_2	$Li_{4.4}Sn/2\ Li_2O$	564.2	fair
TCO, e.g. $Sn_{1.0}B_{0.56}P_{0.40}Al_{0.42}O_{3.6}$	$Li_{4.4}Sn/Li_2O/'B_{0.56}P_{0.40}Al_{0.42}O_{2.6}'$	475.8[a]	good
Sn_2Fe	$2\ Li_{4.4}Sn/Fe$	665.6	poor
$Sn_2Fe/SnFe_3C$ (25:75 w/w)	$0.25\ (2\ Li_{4.4}Sn/Fe)/0.75\ SnFe_3C$	188.8	good
Sn/SnSb, e.g. '$Sn_{0.88}Sb_{0.12}$'	$0.88\ Li_{4.4}Sn/0.12\ Li_3Sb$	764.1	fair

Since 1-D nanostructures have many advantages over nano particles such as superior electric conductivity to current collector and stable structure, tin oxide nanowires are broadly studied as anode materials. Martin et al. [88, 89] fabricated SnO_2 nanofibers using sol-gel template synthesis, which showed extraordinarily improved rate capability and cycling performance

because of the small grain size and the one dimensional current conductivity. Another attempt using SnO_2 nanotubes to overcome the problem of rapid capacity fading was reported by Lee and his co-workers[90]. Uniform polycrystalline SnO_2 nanotubes that have been fabricated through an infiltration route using SnO_2 nanoparticles as starting building units and AAO membranes as the template show a high specific capacity of 525 mA h g^{-1}, which was attained after 80 cycles, as shown in Figure **1.4**.

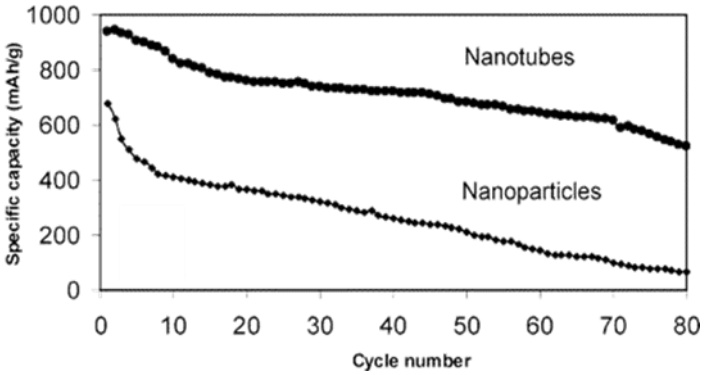

Figure 1.4 Cyclabilities of SnO_2 nanotube electrodes and SnO_2 nanoparticle electrodes (5 mV to 2 V, 0.05 mA/cm^2; voltage versus Li^+/Li) [90].

SnO_2 nanotubes with coaxially grown carbon-nanotube overlayers were prepared by the same group through a confined-space catalytic deposition process assisted by AAO membranes template[91]. The obtained SnO2-core/carbon-shell nanotubes exhibited highly reversible capacity (close to 600 mA h g-1) and excellent cyclability with capacity retention of 92.5% after 200 cycles.

Similar to silicon, alloys formed by tin and other inactive metal can accommodate volume change of Sn during charging/discharging process. The existence of inactive metal matrix which buffers the large volume change during cycling improves stability of the anode structure. Early

in 1999, Winter's group's study proved that tin alloys are much more stable than pure tin during cycling[87], as shown in Figure **1.5**. Inactive metals such as copper[92], nickel (Figure **1.6**) [93, 94], antimony[95] are researched and showed improved cycling stability. Nickel-tin (Ni-Sn) alloy nanowires have been widely studied as potential superior anode material due to the high capacity of Ni-Sn alloy and the easy fabrication process [96, 97].

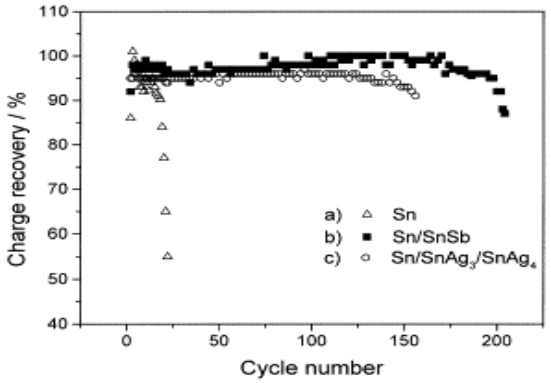

Figure 1.5 Cycle life performance of electroplated Sn, Sn/SnSb and $Sn/SnAg_3/SnAg_4$ on Cu substrates in 1 M $LiClO_4$/PC, $i_c=i_d=0.25$ mA cm^{-2}, charge input: 1.7 Li/M, cut-off: 1.2 V vs. Li/Li^+, typical particle sizes of the metallic materials: 0.2–0.4 μm [87].

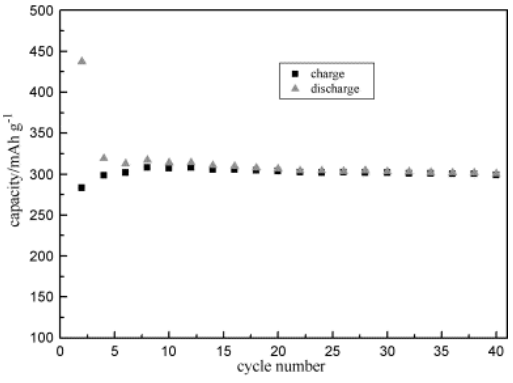

Figure 1.6 Cycle performance of crystalline Ni_3Sn_2 [94].

Recently, Winter's group[98] even studied three-metal alloy for anode material and it shows better performance than two-metal alloys (Figure **1.7**).

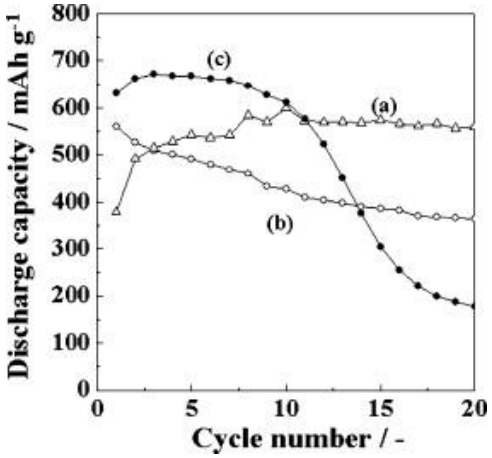

Figure 1.7 Cycle performances of (a) Sn–Sb–Co, (b) Sn–Co, and (c) Sn–Sb film electrodes[98].

1.2.1.4 Other Anode Materials

Many other kinds of materials have been researched due to advantages such as structural stability, low cost, low toxicity, easiness to fabricate, etc.

Special interests have been initiated by iron-based oxides such as Fe_3O_4 and Fe_2O_3 because of their low cost and low toxicity. Simon and his collaborators reported a Fe_3O_4-based Cu nanoarchitectured electrode for Li-ion batteries[99]. The electrode was prepared by using a two-step design: the electrochemically assisted template growth of Cu nanorods followed by electrodeposition of Fe3O4 (Figure **1.8**(a)). The obtained nanostructured electrodes were demonstrated to show a factor of 6 improvement in power density over planar electrodes.

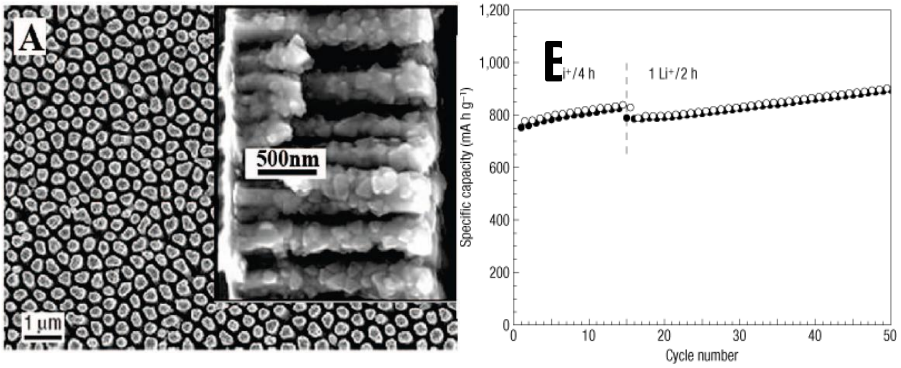

Figure 1.8 (a) Top view of the Cu current collector and cross-sectional view of current collector after Fe_3O_4 deposits; (b) The capacity retention of a Fe_3O_4 film cycled first at 1 Li^+/4 h for 15 cycles followed by a higher rate value of 1 Li^+/2 h [99].

Nanotubes of ironic oxide are also studied and stayed good structure after 100 cycles (Figure **1.9**).

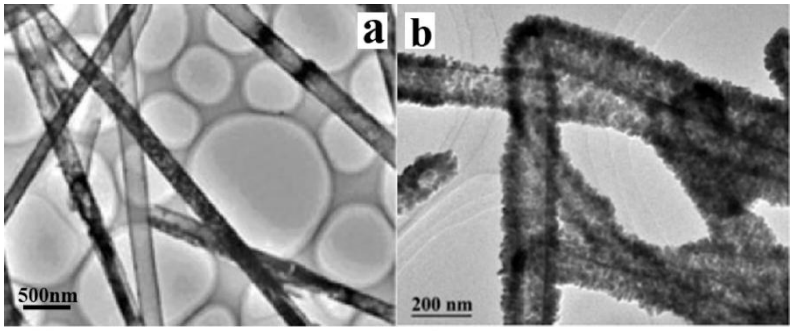

Figure 1.9 TEM images of the templated R-Fe_2O_3 nanotubes (a) before and (b) after 100 charge/discharge cycles [100].

Mesoporous nanowire arrays of Co3O4 are also studied recently as a new kind of anode materials[18], showing high capacity, good cycleability and high rate capability.

There is much current interest in investigating the lithium storage properties of nanotubes and nanowires based on titanium oxide or titanate because of their prominent advantages such as

high capacity, good kinetic characteristics, good robustness and safety, wide availability, and low toxicity [101]. P G. Bruce's group Pioneered researches about Ti based materials for li-ion batteries; they demonstrated TiO_2 nanowires and nanotubes to be promising anode materials for rechargeable lithium batteries [14, 102, 103].

Beside single nanostructure with single material, complex structures with different materials are developed recently. Ortiz et al. [104] reported tin and tin oxide nanowires grown onto titania nanotubes by anodization of titanium and tin electrodeposition for li-ion battery anode. The nanocomposite with this particular geometry has a remarkable reversible capacity of about 140 $\mu A\ h\ cm^{-2}$ which is kept about 85% over 50 cycles.

1.2.2 Active/Inactive Material Interface

Control of electrode–current collector interfacial structure is considered as another alternative resolution toward improved cycling performance of Si[105], considering that the electrochemical and mechanical disconnection between Si and Cu current collector during cycling is one of the causes for unstable cycling behavior of Si [106, 107]. Maranchi *et al.* studied Si film on flat Cu current collector and identified nucleation of a lithium compound based on the interdiffusion of Si and Cu as the most probable cause of the ultimate delamination failure of the deposited film [108].

A popular way to improve adhesion between Si and current collector is modifying the interface topography. Rough interface promotes interfacial contact area between Si and Cu and enhances electron transfer kinetics and cycling performance [28, 105, 109]. For example, in Figure **1.10**, both the etched Cu surface and the nodule-type surface as current collector show better performance than the flat surface. The silicon–graphite composite slurry was coated on the

current collector to form active material film. Although the active material film cracked during the charging/discharging processes, all the active material is still connected to the current collector and contributes to the electrode [107].

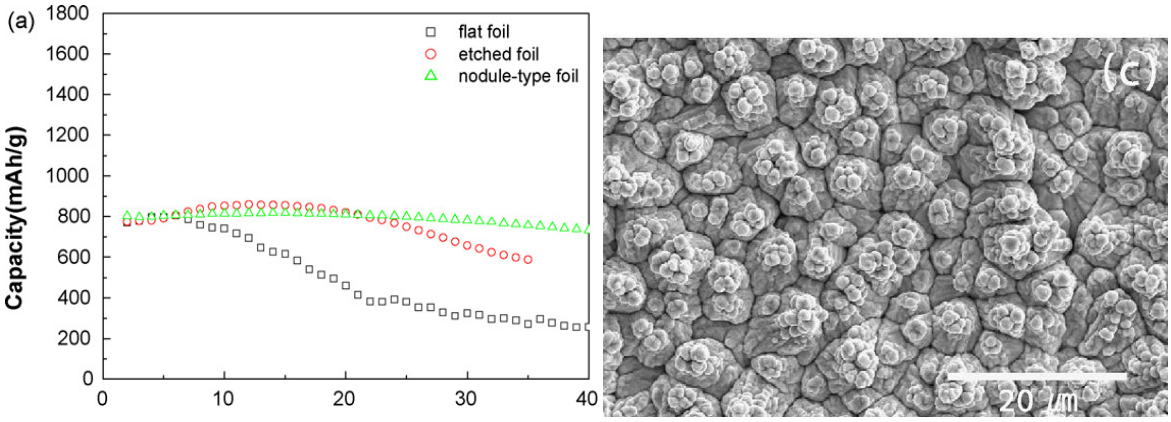

Figure 1.10 (a) Electrochemical performance of Si film on different Current collector surface; (b) nodule-type foil surface [107].

1.2.3 3D Network

3D network was introduced as a superior structure to enhance ion and electron transport kinetics. As discussed by Long and Rolison, the ideal electrode architecture for providing efficient ion and electron transport consists of a three-dimensional (3D) interpenetrating network of electron and ion pathways [39, 40]. By loading nanostructured active materials on a 3D conducting network, benefits of nanostructured active materials and 3D network can be combined. The prime advantages one expects with the proposed 3D architectures for energy storage in batteries, in addition to the small areal footprint, are the short transport lengths for ions in the solid-state electrode as well as between the anode and cathode. That the 3D design minimizes both distances yields concomitant improvements in power density.

There has been plenty of research on applying microscale 3D conduction network into Li-ion battery electrodes. Various 3D networks have been fabricated to serve as conductive pathways in battery cathodes and anodes. A foam-type nickel with pore size of hundreds microns was used as current collector to suppress the separation of the active materials from the current collectors caused by the large volumetric change of the active material powder during the charge/discharge process [33-35]. Porous 3D polymer scaffold was used as a framework to load silicon particles on in the electrodes [110]. The intentionally introduced cavities allow the Si particles to expand without deformation of the electrode structure so that the cycle stability of the Si electrode can be greatly improved. The inverse opals macroporous Li ion electrodes fabricated by means of colloid templating reduce the ion transport length and are particularly promising [36-38].

However, in these structures, long-range ion diffusion and electrical conductivity of the macroporous host can still hardly be improved to a satisfactory level. In general, only modest improvements in rate performance have been observed, because the mesoporous structures only partially address ion and electron transport kinetics.

Instead of using metals or polymer as either the conducting network or the porous framework, carbon is a promising material to construct the network both conductive and porous. By simply mixing carbon with other active materials, a coarse 3D carbon network can be incorporated into the electrodes [46, 111-113]. For example, carbon nanofiber can improve the conduction in electrode when mixed with active material $LiFePO_4$ [114]. Carbon nanotube network is also integrated in Si anodes as current collector [115]. However, the mixed composites do not offer enough porosity in the electrode for electrolyte access.

Carbon has ideal conductivity to serve as current collectors [43]. Conductivity of Si based electrodes has been effectively increased by carbon coating [44, 45]. Another benefit of using carbon as conducting network instead of metal current collectors is carbon can improve the gravimetric capacities of the electrodes due to its light weight [41]. Ductility of carbon help accommodate the volume change and improves the stability of the electrode made from carbon composite structures [46]. The use of Si/C composites to circumvent the limitations of pure Si power has been investigated for many years [111, 116]. However, the large volume changes in Si on Li insertion can be accommodated by the structure consisted of Si particles embedded in a dense carbon matrix only to a limited degree, thus offering only limited stability and capacity enhancements [116].

Carbon nanofoams are considered as one way to introduce porosity to the carbon composite electrodes. 3D carbon foams coated with olivine structured lithium iron phosphate is reported [55]. nanoscale MnO_2 loaded on nanofoam carbonaceous interpenetrating structures showed high volumetric capacitance as electrochemical capacitor [117].

1.3 Objectives

In this thesis, we identify the key challenges of using nanowire array as anodes of Li-ion batteries and address these challenges. By using a facile method with the assistance of free-standing PAA templates, we fabricate high-aspect-ratio Ni-Sn nanowire arrays directly on current collectors. Ni-Sn nanowire arrays with different active/inactive (A/I) interface areas have been realized to study the effect of A/I interface scaling on the electrochemical performance. We have proven that the structural stability and electrochemical performance of Ni-Sn nanowire

array electrode can be significantly improved by creating nanosized active/inactive interfaces at roots of nanowires to reduce the strain mismatch between active and inactive materials [118].

Agglomeration greatly degrades the capacity and the cycle life of nanowire arrays when the nanowire length increases, by degrading the nanoscale wires to micro-sized bundles and reducing the mechanical stability, as shown in Figure **1.11**(a). In this work, we study the effect of nanowire agglomeration on Li-ion battery performance by systematically investigating the electrochemical performance of straight Ni-Sn nanowire arrays with different lengths and construct three-dimensional (3D) self-supporting Ni-Sn nanowire network electrodes to mitigate agglomeration based on our recently-developed 3D PAA template technique [119]. We found that although the electrochemical performance of straight nanowire array electrodes degrades as the nanowire length increases, the electrochemical performance of the 3D Ni-Sn nanowire network electrodes are length-independent, which is attributed to their capability to mitigate agglomeration, as shown in Figure **1.11**(b).

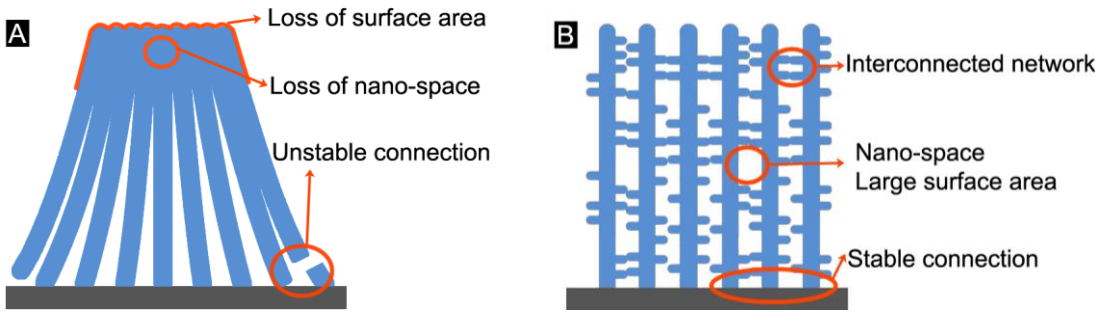

Figure 1.11 Schematics of (a) agglomerated nanowire bundle and (b) 3D nanowire network.

To further improve stability and power performance of the anodes, we built 3D carbon nano-network as conductive backbone of the electrode to load low-conductivity active materials, as demonstrated in Figure **1.12**. In our unique 3-D nanoporous structure, the native nano-scale gaps

allow the Li-ion flow to reach every surface of the electrodes, which means that the contact area between the electrolyte and the electrode is extremely high and can be engineered to be 100 times larger than the contacting surface of the conventional electrodes. Such extremely high contact area is equivalent to an extremely thin electrode which is well known to lead to an extremely high rate battery. In addition, the electrons generated in the electrodes are effectively transferred through a 3D carbon network to the current collectors, which are not planar as is the case with the conventional electrode design – and thus electronically ensure the extremely high rate performance of the battery [120].

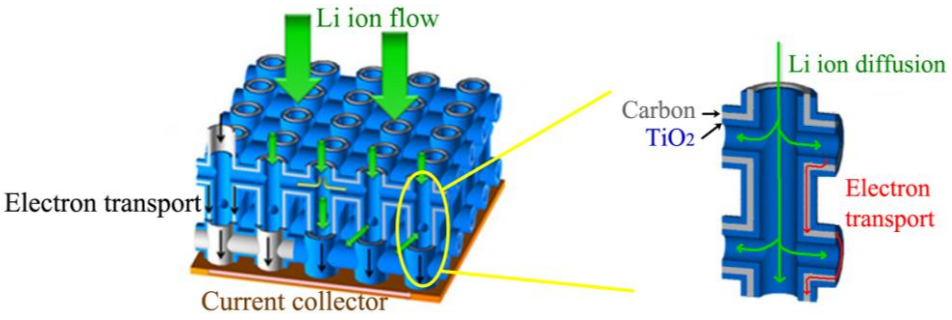

Figure 1.12 Schematics of the 3D C/TiO_2 electrode.

1. Porous Anodic Alumina (PAA) Template

2.1 Conventional PAA Template

2.1.1 Introduction

Porous anodic alumina (PAA) templates with self-ordered hexagonal arrays of cells containing cylindrical pores have been studied for decades. They are prepared by electrochemical oxidation of aluminum. The electrochemical oxidation of aluminum dates back to the beginning of the last century. Anodic treatment of aluminum was widely investigated to obtain protective or decorative films on the surface. Nowadays, porous alumina is one of the most prominent templates for synthesis of nanostructure with monodisperse and controllable dimensions, high aspect ratios, and high density. Moreover, they can be employed as 2D photonic crystals.

PAA templates have four main advantages as a foundation for nano-fabrication. 1) The control of their size in large areas achievable makes them valuable in many occasions. 2) Their high aspect ratio enables the possibility of fabrication of high-aspect-ratio nanowires and nanotubes. 3) Their high regularity of the pore arrays offer the possibility of manipulating nanostructures in a large range to act as an array. 4) Their chemical robustness enable their wide application different areas. Various nanostrucutres such as Ni nanowires[121], Ag nanowires [122], Ni nanoparticles [123], carbon nanotube [124], and even heterogeneous nanowires [125] have been successfully fabricated with the assistance of PAA templates.

The geometry of porous alumina can be schematically represented by a honeycomb structure of nanochannels. It contains an array of columnar hexagonal cells, each including a cylindrical

pore at the center, as demonstrated in Figure **2.1**. By changing the processing conditions, pore diameters ranging from 28 to 400 nm and template thickness from 0.1 to 200 μm can be obtained. In most applications, the Al layer and the barrier layer are removed by wet chemical etching in $CuCl_2$ solution and phosphoric acid in sequence. By tuning the etching time in phosphoric acid, the pore diameter can also be tuned in a certain range without changing the interpore distance.

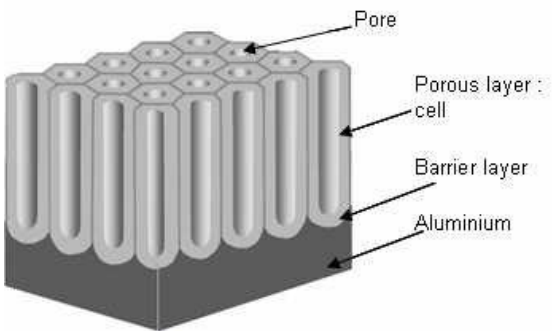

Figure 2.1 Schematic of the structure of PAA template

2.1.2 Fabrication of PAA Template

Porous alumina templates are in fact commercially available from Whatman Inc (www.whatman.com), as shown in Figure **2.2**. Anodisc^{TM} filters are available in three nominal sizes (47, 25 and 13 mm diameter) and three pore sizes (0.2, 0.1 and 0.02 μm) with average membrane thickness of 60 μm. The aspect ratio (pore depth divided by pore diameter) of these membranes is between 300 and 3000.

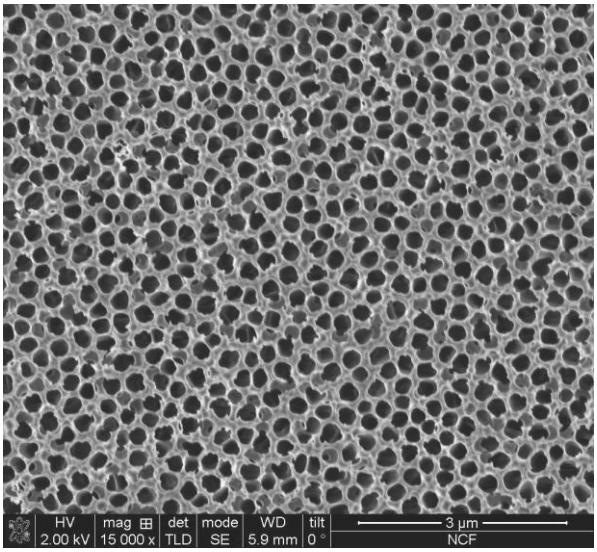

Figure 2.2 SEM image of commercial PAA template from Whatman Inc.

However, the commercial PAA templates do not offer enough variability for scientific researches. Porous alumina templates can be fabricated from aluminium foil or from deposited aluminium on desired substrates depending on the application. In an electrolytic cell with the aluminum as positive electrode, PAA templates are anodized gradually in acid solutions under an electric field between the two electrodes. Various electrolytes can be employed for the anodization process such as sulphuric acid (H_2SO_4), oxalic acid ($H_2C_2O_4$), and phosphoric acid (H_3PO_4). Different pore diameters and interpore distances can be obtained by using different electrolytes. The quality and feature of the porous alumina depend strongly on some physical parameters and the purity of the starting Aluminium. Voltage or current and the choice of acid and its concentration are the key parameters the process. In addition, temperature is another factor which can affect the specimen and even the design of the anodizing system. As shown in Table **2.1**, the pore diameter and inter-pore distance can be controlled not only by the types of electrolyte but also by the applied voltage.

Table 2.1 Anodization conditions and PAA template dimensions

Electrolyte	Voltage (V)	Pore diameter (nm)	Inter-pore distance (nm)
Sulphuric acid (H_2SO_4)	25-27	28-35	60-70
Oxalic acid ($H_2C_2O_4$)	30-80	40-100	80-200
Phosphoric acid (H_3PO_4)	100-195	130-250	250-500

Figure **2.3** shows the PAA templates we made with different diameters. In Figure **2.3**(a), pore diameter of 35 nm is made by anodizing Al in 0.15M sulphuric acid at voltage of 30 V. By anodizing Al in 0.3 M oxalic acid at 60 V, we got PAA template with pore diameter of 80nm, as shown in Figure **2.3**(b). When Al was anodized in 0.3M phosphoric acid at 160 V, PAA template with pore diameter of 200 nm is prepared, as shown in Figure **2.3**(c).

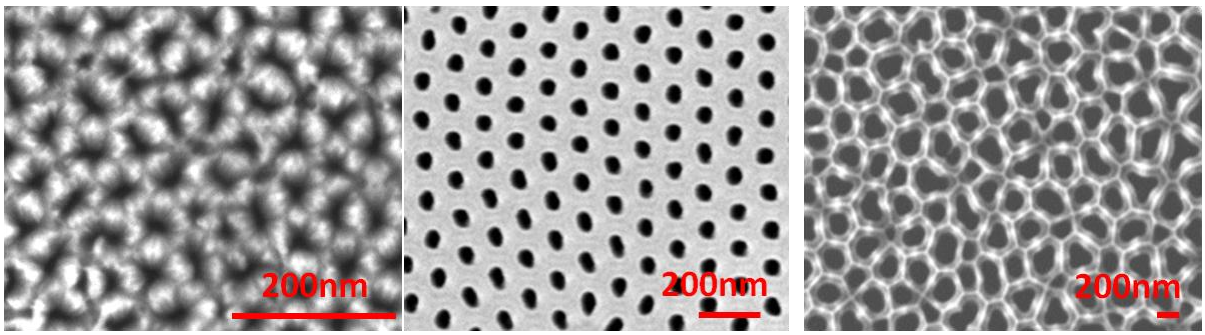

Figure 2.3 SEM images of PAA template with different diameters: (a) 35 nm, (b) 80 nm, and (c) 200 nm.

The chemical reactions involved in the anodization are:

$$Al(s) \rightarrow Al^{3+}(oxide) + 3e^{-} \quad (2.1)$$

$$3/2H_2O(l) \rightarrow 3H^+(aq) + 3/2O^{2-}(oxide) \quad (2.2)$$

As indicated in equation (2.1) and Figure **2.4**, Al^{3+} ions form at the metal/oxide interface and migrate into the oxide layer. Equation (2.2) shows that a water-splitting reaction occurs at the oxide/electrolyte interface, and the resulting O^{2-}(oxide) ions migrate within the oxide from the oxide/solution interface toward the metal/oxide interface under the electric field to form Al_2O_3. This process penetrates from the surface in to the Al and leaves the oxidized porous structure behind.

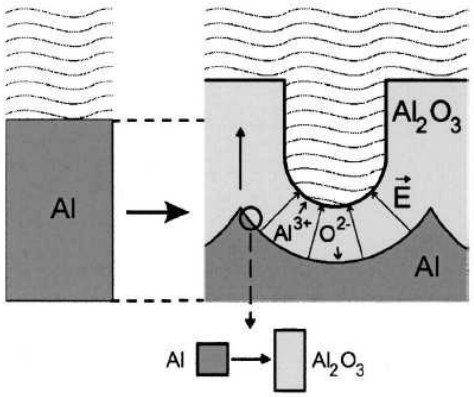

Figure 2.4 Schematic of the anodization reaction

High purity (99.999%) aluminium foils are normally immersed into acids and then the pores propagate through the surface of aluminium. To get self-ordered nanochannel arrays, two-step anodization is introduced. Masuda and Fukuda reported that the pore regularity can be improved by a long anodization time under appropriate conditions [126]. Masuda and Sato also described that, after stripping away the thick oxides obtained from the first anodization, a thin alumina film with highly ordered pores can be obtained by a subsequent re-anodization.

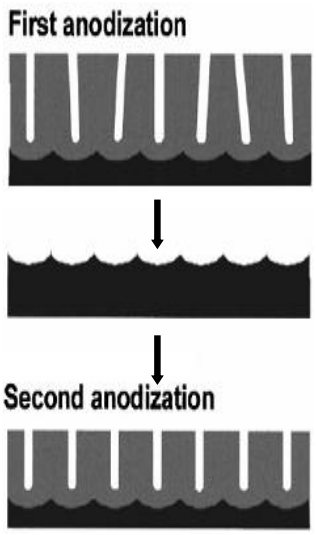

Figure 2.5 Illustration of the two-step anodization

Figure **2.5** illustrates the procedure of two-step anodization for fabricating a hexagonal pore structure. Since the pores initiate at almost random positions and order thereafter by selfadjusting during the anodizing process, pore arrangements on the surface are disordered and have a broad size distribution. Ordered pore domains can only be obtained at the bottom of the layers. Therefore, the pores produced in the first anodization step are not parallel to one another. To fabricate ordered nanopore arrays, the first porous oxide film, which contains the barrier layer at the bottom, has to be removed by wet chemical etching. The barrier layer is not flat but consists of periodically arranged crests and troughs. These fluctuations result in a dimpled and undulating surface that has the same spatial ordering as the barrier layer. After the removal of the porous film, the periodic concave patterns that remain act as a self-assembled template for the second anodization process. An ordered nanopore array is obtained during the second anodization if the same parameters are used as in the first anodization step.

Although the two-step anodization improves the regularity of the nanochannels, the complicated fabrication process hinters its application. One-step fast fabrication of long-range

ordered porous alumina membranes by oxidizing at high voltages, which is call “hard anodization” was invented [127].

2.2 3D PAA template

We use a process similar to the synthesis of straight nanowire arrays for the preparation of 3D Ni-Sn nanowire networks, but with unconventional PAA templates synthesized using low-cost impure Al sheets. Nano-indentations in nanochannels of PAA templates have been reported when anodizing low-purity Al sheets and are regarded as defects [128, 129]. Efforts have been made to fabricate PAA with well-aligned pores out of impure Al foil in various ways such as post-annealing,[130] pre-treatment,[129] and pulsed anodization [131]. Instead of avoiding the irregular pores, in this study, we utilize the defect-containing PAA templates to fabricate 3D Ni-Sn nanowire networks and 3D carbon nano-network to improve anode performance. To distinguish them from the conventional PAA templates used to fabricate straight nanowires, we call these defect-containing PAA templates synthesized from low-purity Al sheets 3D PAA templates. The 3D PAA templates were synthesized by anodizing commercial low-purity 1000 series (99% purity, McMaster 9060K16) Al sheets at 170V in 0.3 M phosphoric acid for 72 hours at 5 ℃, followed by channel widening in 3 wt.% phosphoric acid at 45 ℃ for 2 hours. Figure **2.6** shows the cross-sectional FE-SEM micrograph of a 3D PAA template we prepared. Beside the parallel nanochannels with diameters of ~ 240 nm, there are abundant nano-indentations with a characteristic size of ~ 80 nm on the walls of the straight nanochannels. Some of the nanochannels are even connected by the indentations. Such 3D PAA templates have been used to fabricate 3D Ni-Sn nanowire networks.

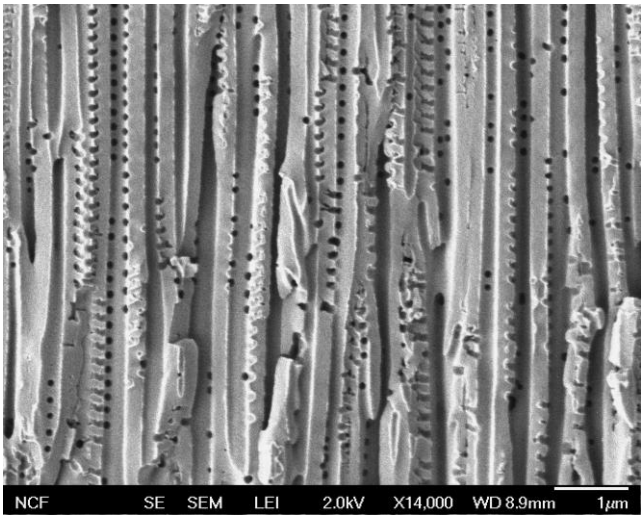

Figure 2.6 Cross-sectional SEM image of a 3D PAA template

Our group has studied the 3D PAA template fabrication of 3D nano-network system and found out that the 3D structure does improve battery performance of the electrodes [119]. The areal capacity of nanowire-based microbatteries can be potentially increased by increasing the length of nanowires. However, agglomeration of high aspect ratio nanowire arrays could greatly degrade the performance of nanowires for lithium ion (Li-ion) battery applications. In this work, a three-dimensional (3-D) Ni/TiO2 nanowire network was successfully fabricated using a 3-D porous anodic alumina (PAA) template-assisted electrodeposition of Ni followed by TiO2 coating using atomic layer deposition. Compared to the straight Ni/TiO2 nanowire arrays fabricated using conventional PAA templates, the 3-D Ni/TiO2 nanowire network shows higher areal discharging capacity. The areal capacity increases proportionally with the length of nanowires. With a stable Ni/TiO2 nanowire network structure, 100% capacity is retained after 600 cycles.

2.3 Summary of Porous Anodic Alumina Template

By controlling the anodization conditions, we are able to fabricate conventional PAA templates with various dimensions. They would be used in our study of nanowires as anode of Li-ion batteries. By using impure Al foil instead of expensive high-purity Al, we can prepare 3D PAA templates for innovative use of PAA template: 3D nanowire network.

2. Active/Inactive Material Interface in Ni-Sn Nanowires

3.1 Introduction

Control of electrode–current collector interfacial structure is considered as another alternative resolution toward improved cycling performance of Si[105], considering that the electrochemical and mechanical disconnection between Si and Cu current collector during cycling is one of the causes for unstable cycling behavior of Si [106, 107]. Maranchi *et al.* studied Si film on flat Cu current collector and identified nucleation of a lithium compound based on the interdiffusion of Si and Cu as the most probable cause of the ultimate delamination failure of the deposited film [108].

A popular way to improve adhesion between Si and current collector is modifying the interface topography. Rough interface promotes interfacial contact area between Si and Cu and enhances electron transfer kinetics and cycling performance [28, 105, 109]. For example, in Figure **1.10**, both the etched Cu surface and the nodule-type surface as current collector show better performance than the flat surface. The silicon–graphite composite slurry was coated on the current collector to form active material film. Although the active material film cracked during

the charging/discharging processes, all the active material is still connected to the current collector and contributes to the electrode [107].

For present commercial Li-ion batteries, carbon is broadly adopted as an anode material, but its low specific capacity limits further development of Li-ion batteries[132]. It has been shown that tin and tin-based materials are promising candidates to replace the carbon-based anode material for Li-ion batteries because of their large theoretical capacity (i.e., 990 mA h g^{-1}, the supposed formation of Li4.4Sn alloy) and safety benefit in avoiding the formation of hazardous Li dendrite [85]. Besides the fact that pure tin has a high specific charge, tin oxides, and tin alloys are also promising for application in Li-ion batteries [88, 133-135]. Although their specific charge is not as high as that of pure tin, their complex structures help accommodate volume change during the cycling process, because the inactive components act as a matrix to buffer volume variation [86, 136, 137]. Ni-Sn system is one of these. Besides improving accommodation of volume change during charging and discharging [138, 139], Ni can easily be deposited electrochemically to form an alloy with Sn [140]. Furthermore, Ni has good electrical conductivity, ensuring fast charge transfer. By fabricating nano-architectured intermetallic electrodes of Ni-Sn composite, promising results have been obtained [141]. However, the thin coating of active material on nanorods of Cu limits the capacity density of the electrode. Nanowires should solve this problem and provide high packaging capacity.

We used a facile method with the assistance of free-standing porous anodic alumina (PAA) templates to fabricate high-aspect-ratio Ni-Sn nanowire arrays directly on current collectors. PAA template, produced by electrochemical oxidation of aluminum, is widely used to fabricate nanowire arrays due to the tunability and the compatibility with various materials [122, 142].

Ni-Sn nanowire arrays with different A/I interface areas have been fabricated to study the effect of A/I interface scaling on the electrochemical performance.

3.2 Fabrication of Ni-Sn Nanowires with Different A/I Interfaces

Commercial and homemade porous anodic alumina (PAA) templates were used for the synthesis of Ni-Sn nanowire arrays. The commercial PAA templates (Anodisc 47, Whatman 6809-5522) have an average pore diameter of 200 nm. The homemade PAA templates with an average pore diameter of 80 nm were obtained by anodizing high-purity (5N) aluminum foil at 40V in 0.3 M oxalic acid for 24 hours at 5 ℃.

A two-step electrochemical deposition process was developed to directly grow nanowire arrays on Cu current collector.

The first step is to electrochemically deposit short nanorods to bond the PAA template onto the Cu substrate. Figure 3.1 shows a typical sandwich-structure setup for this step. A constant voltage was applied between the Cu substrate and the counter-electrode for a certain time to grow short nanorods, which serve as "nanoscrews" to bond the PAA template onto the Cu substrate for the second step three-electrode electrochemical deposition. Two kinds of materials, intermetallic Ni-Sn or Cu, were electroplated as the bonding materials for different Ni-Sn nanowire on Cu current collector samples. For Ni-Sn bonding, the deposition was conducted at voltage of -1 V for 10 minutes and the electrolyte consisted of 17.82 g L^{-1} $NiCl_2$ $6H_2O$, 39.4 g L^{-1} $SnCl_2$ $2H_2O$, 165.15 g L^{-1} $K_4P_2O_7$, and 9.38 g L^{-1} glycine, with an addition of NH_4OH 5 mL L^{-1} for pH value control [141]. For Cu bonding, the deposition was conducted at voltage of -0.8 V for 10 minutes and the electrolyte consisted of 6 g.L^{-1} cupric pyrophosphate ($Cu_2P_2O_7.xH_2O$;

Sigma-Aldrich 344699), 25 g.L^{-1} potassium pyrophosphate ($K_4P_2O_7$, Sigma-Aldrich 322431), and 2 g L^{-1} ammonium citrate ($C_6H_{17}N_3O_7$, Fluka 09831) [143]. Figure 3.1(b) shows the short Cu nanorods grown in this step with length of ~ 0.6 μm. Similar nanorods of Ni-Sn with a length of ~1 μm were observed when intermetallic Ni-Sn is deposited as the bonding material.

In the second step, Ni-Sn nanowires were fabricated by co-depositing Sn and Ni in a three-electrode glass cell filled with the same Ni-Sn electrolyte as that in the first step. An Ag/AgCl electrode immersed in the saturated KCl solution was used as a reference electrode, and a Pt coil was used as the counter-electrode for three-electrode electrochemical deposition. The potentiostatic deposition was performed on a CHI 760c electrochemical work station. After electrochemical deposition, the final Ni-Sn nanowire array samples were obtained after immersing in 1 M NaOH solution to dissolve the PAA templates and cleaning with DI water.

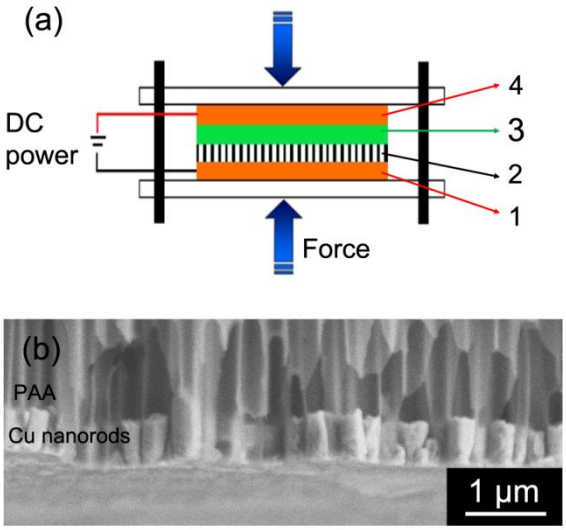

Figure 3.1 (a) Schematics of the sandwich structure used for electroplating short nanorods to bond the PAA template on the Cu substrate: 1-copper foil which serves as current collector and as the substrate of nanowire arrays, 2-PAA template, 3- filter paper saturated with electrolyte

solution, and 4- copper plate which serves as counter electrode. (b) Short Cu nanorods deposited in the PAA template which bonds PAA template on Cu substrate for the second electroplating step.

Figure **3.2** shows the difference between the Ni-Sn nanowire arrays with two kinds of PAA template bonding materials. When Ni-Sn nanorods were used for bonding in the first step (Figure **3.2**(a)), a thin film of intermetallic Ni-Sn was formed in the gap between the PAA template and the Cu substrate due to the roughness on copper surface, which resulted in a large continuous A/I interface. The FE-SEM image of Ni-Sn nanowires on Cu current collector confirms the formation of continuous Ni-Sn film. In the other structure, Cu nanorods were used to bond the PAA template onto Cu substrate (Figure 3.2(b)). Cu film was formed in the gap between the PAA template and the Cu substrate, followed by copper nanorods in nanopores of the PAA (Figure 3.1(b)), which reduces the A/I interface (Ni-Sn/Cu interface) to nanoscale islands on top of Cu nanorods. The FE-SEM image in Figure **3.2**(b) shows that the A/I interface is confined to the cross-section of each nanowire.

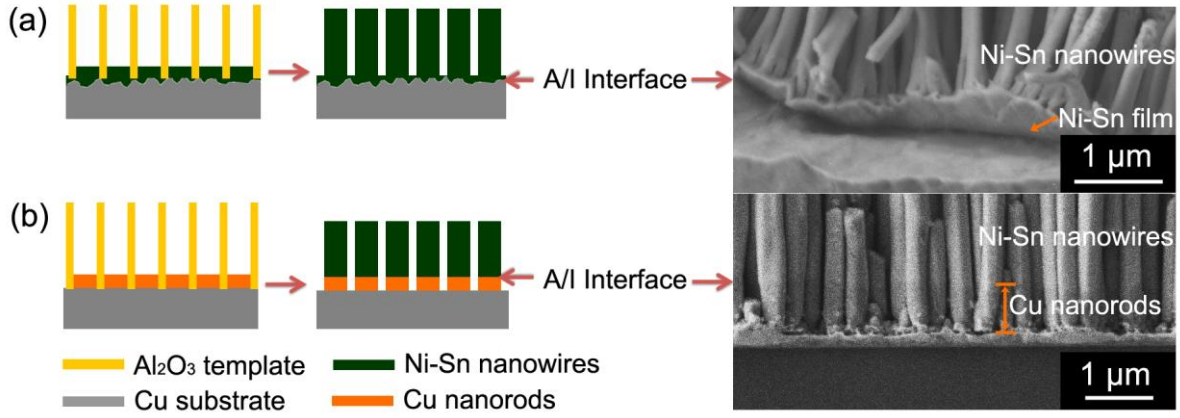

Figure 3.2 Schematics and FE-SEM images of Ni-Sn nanowire arrays with different bonding materials at base: (a) Ni-Sn bonding and (b) Cu bonding.

Figure **3.3**(a) and Figure **3.3**(b) show the FE-SEM images of Ni-Sn nanowire arrays with a characteristic nanowire diameter of ~200 nm and ~80 nm, respectively. The length of the nanowires is controlled by adjusting the electrochemical deposition time, and the diameter is determined by the pore size of PAA templates, as shown in the inset figures. The nanowires are agglomerated, and micro-scale gaps are formed between nanowire clusters due to the high aspect ratio. In the XRD spectrum of the as-prepared Ni-Sn nanowires in Figure **3.3**(c), peaks of Ni_3Sn_4 alloy can be clearly identified, indicating that Ni_3Sn_4 is the predominant phase in the intermetallic Ni-Sn, consistent with reported results of electrodeposited Ni-Sn [144, 145]. The peak of Cu comes from the Cu current collector. The EDS spectrum in Figure **3.3**(d) shows that the as-prepared Ni-Sn nanowire arrays contain about 82 wt% Sn.

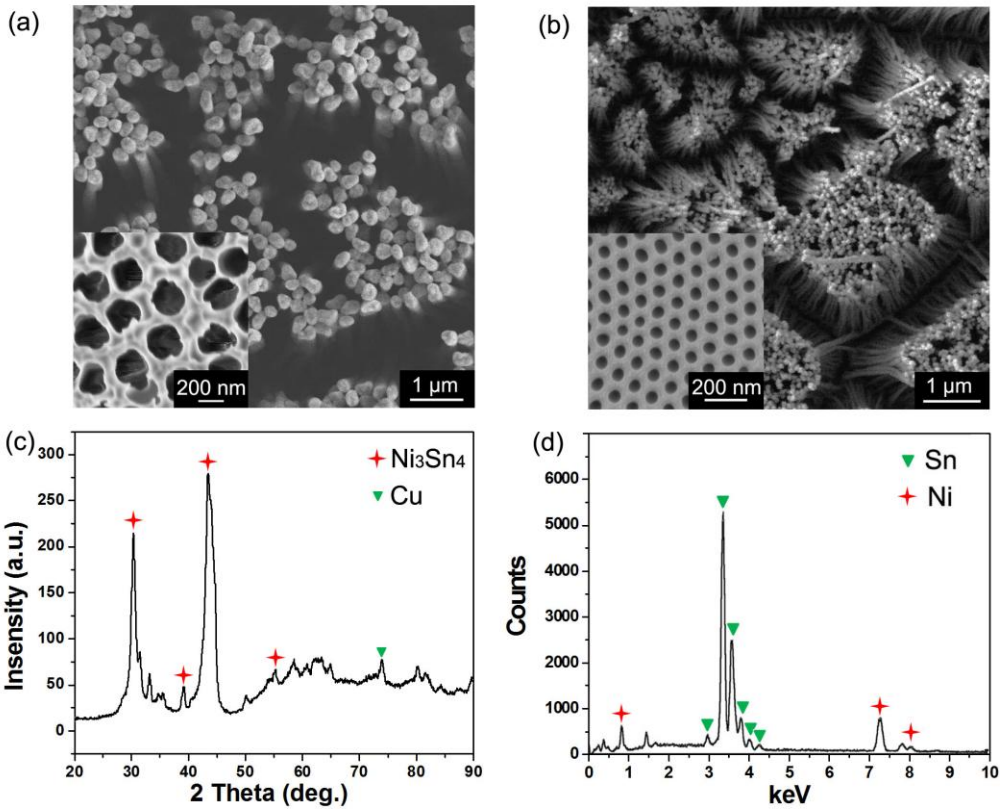

Figure 3.3 (a) Ni-Sn nanowire arrays with a nanowire diameter of ~200 nm using a commercial PAA template (Inset: PAA template with 200 nm pore diameter). (b) Ni-Sn nanowire arrays with a nanowire diameter of ~80 nm using a home-made PAA template (Inset: PAA template with 80 nm pore diameter). (c) X-ray diffraction (XRD) spectrum of ~200 nm Ni-Sn nanowire arrays. (d) Energy-dispersive X-ray spectroscopy (EDS) spectrum of ~200 nm Ni-Sn nanowire arrays.

3.3 Electrochemical Performance of Ni-Sn Nanowires with Different A/I Interfaces

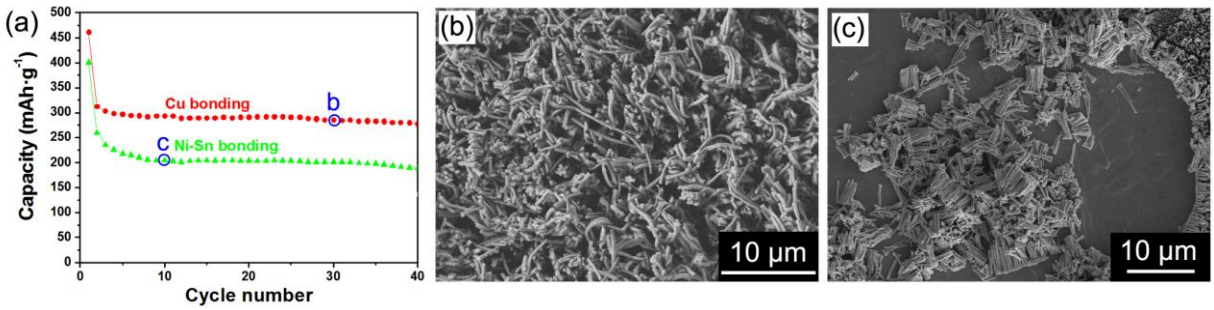

Figure 3.4 (a) Electrochemical performance of Li-ion batteries using Ni-Sn nanowires with Cu bonding and with Ni-Sn bonding as anodes. The nanowire diameter in both samples is around 200 nm, and the length is around 8 μm. Material load for both samples is 1.55 mg•cm-2. Test current is 50 mA•g-1. (b) FE-SEM image of the Cu bonded Ni-Sn nanowires after 30 cycles; (c) FE-SEM image of the Ni-Sn film bonded Ni-Sn nanowires after 10 cycles.

Figure **3.4**(a) shows the discharge capacity over cycle number for Ni-Sn nanowire array anodes with different bonding materials at the base. The capacities of the electrodes using both Ni-Sn nanowire arrays drop a lot after the first cycle. Similar observation has been reported for most Sn based materials [146], due to the formation of solid-electrolyte interphase (SEI) and the irreversible decomposition of intermetallic Ni-Sn during the activation step. Much higher capacity is observed for Ni-Sn nanowire arrays with Cu nanorods at the base than that of Ni-Sn nanowire arrays with Ni-Sn film bonding, especially after the second cycle. FE-SEM image in Figure **3.4**(b) shows that the Ni-Sn nanowires with Cu nanorods at the base maintain intact on the Cu current collector after 30 cycles. However, a large number of nanowires fell off from the Cu current collector after 10 cycles for the sample with Ni-Sn bonding film at the base, as shown in Figure **3.4**(c), although all the nanowires are still intact. Since the only difference between the two samples is the materials at the base of Ni-Sn nanowires, the comparison clearly shows that

the Ni-Sn film at the base resulted in the failure of Ni-Sn nanowires electrode. The reason for the failure could be due to the large strain mismatch resulted from the large A/I interface introduced by the continuous Ni-Sn film [116, 147]. However, in the Ni-Sn nanowire arrays with Cu bonding, the A/I interface area is reduced to nanoscale island as shown in Figure **3.2**, which significantly reduces the strain mismatch and thus improves the electrochemical performance of the Ni-Sn nanowire electrodes. The capacity was improved and the Ni-Sn nanowires were retained on Cu current collector after 30 cycles. We can preliminary conclude from the above comparison that electrode performance can be improved by scaling down A/I interface area.

To confirm the above observations and to further improve the battery performance, we further reduced the interface area between the active Ni-Sn nanowires and inactive Cu current collector by adjusting the nanowire diameters of the Cu nanorod-bonded Ni-Sn nanowire samples. When the diameter of nanowires decreases, the A/I interface area which is the same as cross-sectional area of the nanowires also decreases. Figure **3.5**(a) shows discharge capacities of electrodes using different diameter Ni-Sn nanowire arrays with Cu nanorod bonding. During the first 30 cycles, similar capacity was measured for nanowires with 200 nm and 80 nm diameters. However, the specific capacity of 200 nm-diameter nanowires drops dramatically after 30 cycles while that of 80 nm-diameter nanowires mostly retains. This indicates that Ni-Sn nanowires with smaller diameter have better cycle stability. One possible reason for the better cycle stability observed could be that smaller nanowires can accommodate better the volume change during lithium insertion and release processes because of the reduced diffusion-induced stress, as reported in theoretical studies [148]. However, this is not the main reason here. Figure **3.5**(b) shows the FE-SEM image of the 200 nm-diameter Ni-Sn nanowire electrode after 48 discharge-charge cycles. Ni-Sn nanowires (bundles on right side) lost contact from the current collector,

leaving short Cu nanorods (on left side) on the substrate. EDS spectrum taken from the position c in Figure **3.5**(b) confirms that the nanostructures remaining on the substrates are Cu nanorods, as shown in Figure **3.5**(c). From the above results, the well-retained nanowire structures confirm that pulverization from diffusion-induced stress is not the failure mechanism for the 200 nm-diameter Ni-Sn nanowires. Furthermore, comparing with Figure **3.4**(b), the drop of the capacity for the 200 nm-diameter nanowire sample after 35 cycles is due to the fall-off of Ni-Sn nanowires from the Cu current collector, which resulted from an unstable A/I interface. Ni-Sn nanowires swell and shrink during the charge-discharge process, causing the strain mismatch at the A/I interface since the inactive current collector experiences no volume change. The strain mismatch, which results in mechanical instability and hence the poor cycle stability, was reduced by reducing A/I interface area, which was realized by reducing diameter of Cu bonded Ni-Sn.

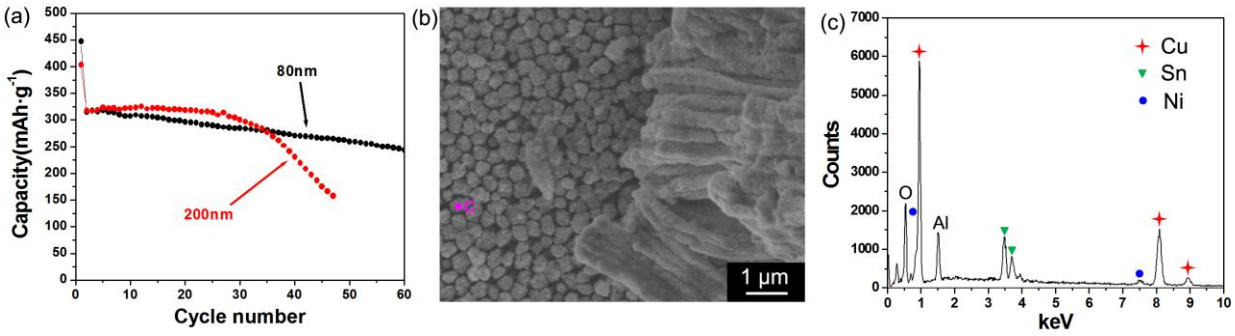

Figure 3.5 (a) Discharge capacity of Cu nanorod-bonded Ni-Sn nanowire arrays with different diameters. Test current is 50mA/g and Ni-Sn nanowire length is ~8 μm. (b) FE-SEM image of the electrode with 200 nm-diameter Cu nanorods-bonded Ni-Sn nanowire arrays after 48 cycles of test; (c) EDS spectrum from the position c in (b).

3.4 Summary of Ni-Sn Nanowires with Different A/I Interfaces

A porous anodic alumina (PAA) template-assisted electrochemical deposition method was used to directly synthesize Ni-Sn nanowire arrays on Cu current collectors. Formation of a continuous Ni-Sn film at the base introduces a large continuous (A/I) interface, which leads to the weak mechanical stability due to large strain mismatch. By growing short Cu nanoscrews as a buffer layer before Ni-Sn nanowire growth, the A/I interface was scaled down to nanoscale islands, which resulted in enhanced structural stability and battery performance. Further reduction of A/I interface by reducing the nanowire diameter of Cu-bonded nanowires results in even more stable electrode.

3. 3D Ni-Sn Nanowire Network

4.1 Introduction

Recently, there has been tremendous interest and effort in using nanowire arrays as electrodes for high capacity and high power Li-ion batteries. There are many advantages to using nanowire arrays as battery electrodes [14, 15, 19, 149]: (1) the spaces between nanowires provide not only easy access of electrolyte to active materials but also efficient volume-change accommodation during the charging/discharging processes; (2) the large specific surface area and the small diameter of nanowires facilitate Li-ion reaction with electrodes; (3) the direct connection of nanowires to the current collector allows efficient electron flow after electrons being generated, which eliminates the necessity of binder materials or conducting additives [17, 18, 150-152]. For example, gravimetric capacity higher than 1000 mAh g^{-1} with ~ 90% capacity

retention over 100 cycles has been recently realized by using Si nanowires [153]. Despite the promising improvements, low mass loading of active materials and low areal capacity still limits straight nanowire arrays as battery electrodes [106, 120, 154-156]. The areal capacity of straight nanowire array electrodes could potentially be increased by increasing the length of the nanowires [24]. However, the high aspect ratio of long nanowires leads to agglomeration, which can significantly degrade the electrochemical performance of nanowire array electrodes due to the reduced surface area, blocked Li-ion diffusion, and the increased stress in the agglomerated nanowire arrays.

Nickel-tin (Ni-Sn) alloy nanowires have been widely studied as potential superior anode material due to the high capacity of Ni-Sn alloy and the easy fabrication process [96, 97]. To develop of high areal capacity Ni-Sn nanowire electrodes using longer Ni-Sn nanowires, a big challenge, agglomeration, is unavoidable. In this section, we focus on two objectives: (1) understanding the effect of nanowire agglomeration on Li-ion battery performance by systematically investigating the electrochemical performance of straight Ni-Sn nanowire arrays with different lengths. and (2) constructing three-dimensional (3D) self-supporting Ni-Sn nanowire network electrodes to mitigate agglomeration based on our recently-developed 3D PAA template technique [119]. We found that although the electrochemical performance of straight nanowire array electrodes degrades as the nanowire length increases, the electrochemical performance of the 3D Ni-Sn nanowire network electrodes are length-independent, which is attributed to their capability to mitigate agglomeration.

4.2 Sample Preparation

The PAA templates were prepared by anodizing Al sheets in phosphoric acid. The conventional PAA templates with straight nanochannels were synthesized by anodizing high-purity (99.999%) Al sheets at 180V in 0.3 M phosphoric acid for 72 hours at -3 ℃, followed by channel widening in 3 wt.% phosphoric acid at 45 ℃ for 3 hours 15 min [157]. The resulting PAA template has channels with diameters of ~ 250 nm and an interchannel distance of ~ 480 nm. The 3D PAA templates with nano-indentations along the nanochannels were synthesized by anodizing commercial low-purity 1000 series (99% purity, McMaster 9060K16) Al sheets at 170V in 0.3 M phosphoric acid for 72 hours at 5 ℃, followed by channel widening in 3 wt.% phosphoric acid at 45 ℃ for 2 hours [119]. The resulting 3D PAA template has channels with diameters of ~ 240 nm and an interchannel distance of ~ 460 nm. The characteristic size of the indentations in the nanochannels is ~ 80 nm.

A two-step electrochemical deposition process was used to grow both straight Ni-Sn nanowire arrays and 3D Ni-Sn nanowire networks on Cu current collectors, which controls nanosized inactive/active interfaces by the growth of short Cu nanowires on the current collector before Ni-Sn electroplating [118]. The first step is to electrodeposit short Cu nanorods to bond the PAA template onto the Cu substrate (current collector). A sandwich structure that stacks the substrate (Cu current collector), PAA template, filter paper saturated with electrolyte, and counter-electrode in sequence was used in this step. A constant voltage of 0.8 V was applied between the Cu substrate and the counter-electrode for 10 minutes to grow short nanorods, which serve as "nanoscrews" to bond the PAA template onto the Cu substrate. The electrolyte consists of 6 g L^{-1} cupric pyrophosphate ($Cu_2P_2O_7.xH_2O$; Sigma-Aldrich 344699), 25 g L^{-1} potassium pyrophosphate ($K_4P_2O_7$, Sigma-Aldrich 322431), and 2 g L^{-1} ammonium citrate ($C_6H_{17}N_3O_7$,

Fluka 09831) [143]. In the second electrodeposition step, Ni-Sn nanowires were synthesized by co-depositing Sn and Ni in a three-electrode glass cell at -1 V (vs. Ag/AgCl reference electrode) with the Cu substrate bonded with the PAA template as working electrode and a Pt coil as the counter-electrode. The electrolyte consists of 17.82 g L^{-1} $NiCl_2$ $6H_2O$, 39.4 g L^{-1} $SnCl_2$ $2H_2O$, 165.15 g L^{-1} $K_4P_2O_7$, and 9.38 g L^{-1} glycine, with an addition of NH_4OH 5 mL L^{-1} for pH value control [96, 147]. The potentiostatic deposition was performed on a CHI 760c electrochemical work station. Finally, the Ni-Sn nanowire samples were immersed in 1 M NaOH solution to dissolve the PAA templates and cleaned with deionized water. The composition of both Ni-Sn nanowire arrays and 3D Ni-Sn nanowire networks are similar, with around 87 wt.% Sn, using this two-step electrochemical deposition process.

4.3 Performance Degradation of Straight Ni-Sn Nanowire Arrays

To study the effects of agglomeration on the electrochemical performance of straight Ni-Sn nanowire array electrodes, straight Ni-Sn nanowire arrays were fabricated by electrodeposition of intermetallic Ni-Sn into conventional porous anodic alumina (PAA) templates with straight nanochannels [70, 158-160], followed by dissoving the PAA templates in a NaOH solution . The high surface tension of water causes agglomeration of nanowires when the nanowires are released and dried. Figure **4.1**(a), Figure **4.1**(b), and Figure **4.1**(c) show top-view field emission scanning electron microscope (FE-SEM) micrographs of Ni-Sn nanowire arrays with lengths of 5 μm, 20 μm, and 40 μm. Clearly the nanowires agglomerated into micron-size bundles. More severe agglomeration is observed in longer nanowire arrays due to their higher aspect ratio and lower stiffness. The average diameters of the agglomerated nanowire bundles increase from 1.5 μm to 19 μm when the nanowire length increases from 5 μm to 40 μm. Apparently, more

nanowires are in contact with one another in larger agglomerated nanowire bundles, which results in larger surface area loss in longer nanowire arrays.

The as-prepared Ni-Sn nanowire samples were tested in an electrolyte containing 1 M $LiPF_6$ in ethylene carbonate (EC)/dimethyl carbonate (DMC) (1:1 volume ratio, Aldrich), with Li foil (Alfa Aesar) as counter-electrode. The CR2032 coin-type cells were assembled in an argon-filled glove box system (Vacuum Atmosphere Nexus model) and tested with a computer controlled potentiostats/galvanostats system (MTI, 5V1mA). The discharge-charge experiments were performed galvanostatically within the voltage window of 0.01-1.5 V (vs. Li/Li+). The gravimetric capacity is calculated with respect to the mass of the Ni-Sn alloy.

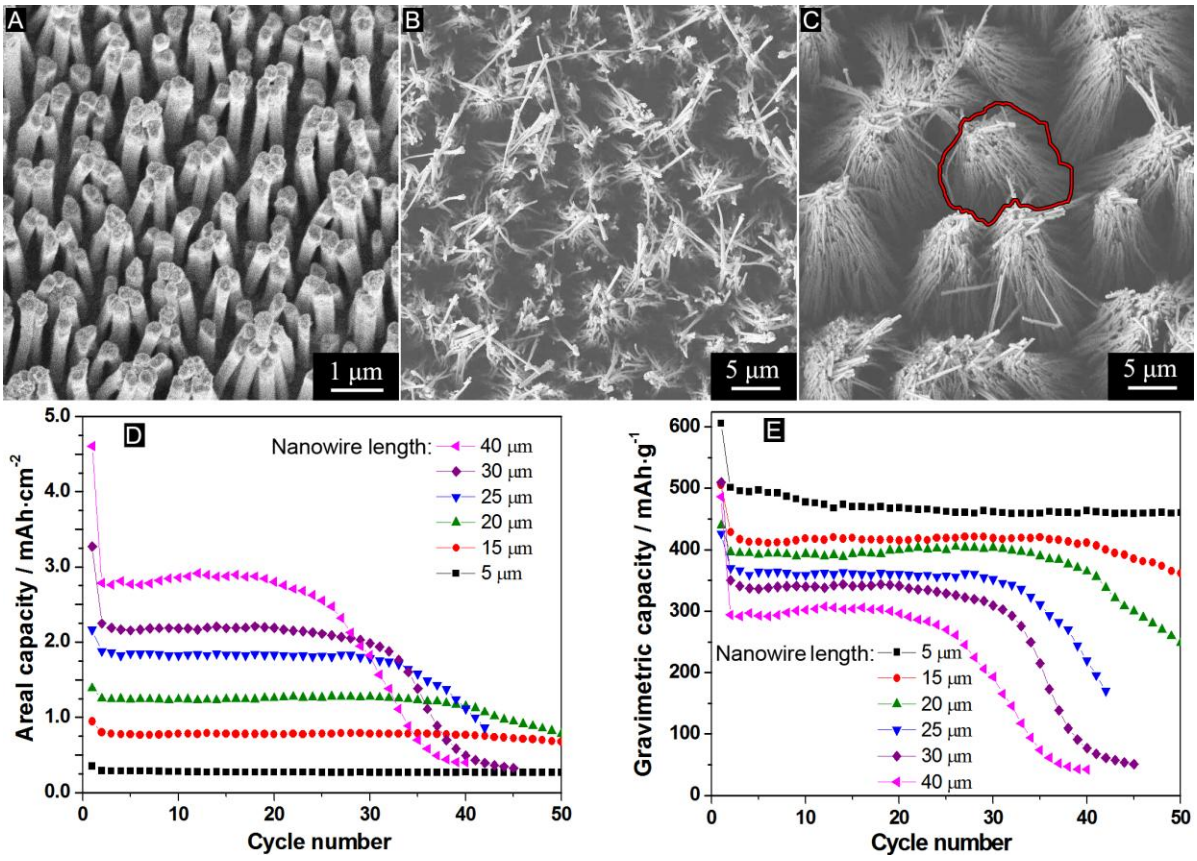

Figure 4.1 Top-view FE-SEM micrographs of straight Ni-Sn nanowire arrays with lengths of (a) 5 μm, (b) 20 μm, and (c) 40 μm. One agglomerated nanowire bundle is circled in red in (c). (d) Areal capacity and (e) gravimetric capacity of Ni-Sn straight nanowires with different lengths. The test rate is set at C/5.

In Figure **4.1**(d), areal discharging capacities of Ni-Sn nanowire arrays with different nanowire lengths are compared. In general, the areal capacity of Ni-Sn nanowire array electrodes increases when the nanowire length increases, due to the mass-loading increase of the active material. The 40-μm-long Ni-Sn nanowire electrode can deliver a reversible areal capacity as high as 2.8 mAh cm^{-2}, which is 6.2 times that of the Ni-Sn film reported by Hassoun *et al.* [161] (0.45 mAh cm^{-2}) and 10.4 times that of the 5-μm-long Ni-Sn nanowires (0.27 mAh cm^{-2}). This

observation confirms that longer Ni-Sn nanowires can increase the areal capacity of nanowire array electrodes.

However, because of the agglomeration of straight nanowire arrays, the gravimetric capacity and the cycle life of the electrodes degrade significantly when the nanowire length increases, as shown in Figure **4.1**(e). The gravimetric capacity of the Ni-Sn nanowire electrodes decreases from ~ 470 mAh g^{-1} to ~ 300 mAh g^{-1} when the nanowire length increases from 5 μm to 40 μm. The stability of the electrodes also decreases when the nanowire length increases. The 5-μm-long nanowire electrode lasted over 50 cycles with 92% of the second-cycle capacity retained, while the 40-μm-long nanowire electrode lasted only around 25 cycles before the capacity dropped dramatically. The loss of gravimetric capacity is due to (1) the limited access of the electrolyte to the active material caused by the loss of surface area, and (2) the long Li-ion diffusion path caused by the increase of the nanowire bundle size.

To understand the mechanisms underlying the degraded cycle life in the agglomerated Ni-Sn nanowires, we have carefully examined the agglomerated nanowire bundles. We use Figure **4.2**(a) to illustrate a micro-sized bundle of the agglomerated nanowires shown in Figure **4.1** (a)-(c). The cross section of an agglomerated nanowire bundle can be simplified as an isosceles trapezoid, with the long base a (the average diameter of agglomerated nanowire bundle), the height h (the length of the nanowires), and the short base b (the diameter of the bundle top area). The inclination angle α of the nanowires at the edge of bundles can be approximated as $\alpha = \tan^{-1}[(a-b)/2h]$. As summarized in Table 1, α becomes larger when the nanowire length increases. If we think of a nanowire bent by adhesion as a clamped beam subjected to a moment M at its free end, M is proportional to the inclination α. Clearly, the data presented in Table 1 indicate that longer nanowires are subjected to larger bending due to agglomeration.

We consider a two-dimensional Ni-Sn nanowire beam (Young's modulus of 100 GPa, Poisson's ratio 0.3[162]) on copper substrate (Young's modulus of 120 GPa, Poisson's ratio 0.34). The interface between the Ni-Sn nanowire and the copper substrate is regarded as perfect, i.e., no interfacial damage or failure due to mechanical loading is considered. A bending moment due to the adhesion in the agglomerated nanowires is applied at the free end of the beam. The calculation is performed by using the commercial finite element software Abaqus.[163] The maximum principal stress contour (Figure **4.2**(b)) is plotted to demonstrate that the most probable interfacial failure happens at the root of a nanowire, due to stress concentration. Based on linear elastic theory[164] and the experimental measurements given in Table **4.1**, longer nanowires have higher maximum principal stress at the root, which results in short life time of those nanowires when subjected to cyclic loading during charging/discharging processes.

In general, the most severe stress concentration occurs at the root of a bent nanowire, as demonstrated in the finite-element analysis shown in Figure **4.2**(b). The principal stress contour shows that the stress concentrates at the root of the nanowire due to agglomeration-induced bending. Bear in mind that the stress concentration level is proportional to the applied moment in linear elastic problems; higher stresses are concentrated at the root of longer nanowires due to the agglomeration. This mechanical analysis is confirmed by the micro-structural analysis. In Figure **4.2**(c), the 20-μm-long Ni-Sn nanowires have good connections to the substrate before the cycling processes. In contrast, in the 40-μm-long Ni-Sn nanowire sample shown in Figure **4.2**(d), we can clearly observe that some peeled off at the edge of the micro-sized bundles, which experience the most severe mechanical stress due to agglomeration. Earlier works on Ni-Sn nanowire array electrodes showed that reliable electrical connection between the nanowires and the current collector is one of the keys to obtaining a stable electrode [118, 165]. The mechanical

analysis here proves that the high stress-induced fatigue at the interface between the Ni-Sn nanowires and the Cu substrate is the cause of the shorter cycle life observed in the longer Ni-Sn nanowire arrays [166].

In short, agglomeration greatly degrades the capacity and the cycle life of straight Ni-Sn nanowire arrays when the nanowire length increases, by degrading the nanoscale wires to micro-sized bundles and reducing the mechanical stability.

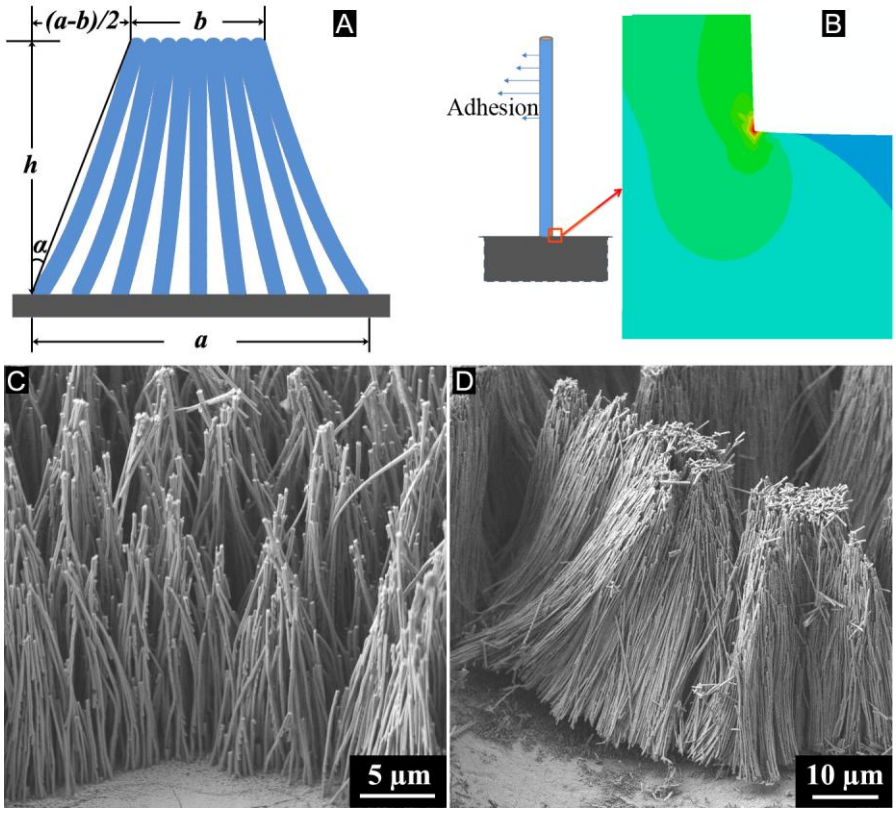

Figure 4.2 (a) Schematic of an agglomerated nanowire bundle. (b) The clamped beam model used to study the stress in a bent nanowire and the principal stress contours at the root of a nanowire. The colors from red to blue correspond to stress concentrations from highest to lowest. Cross-sectional FE-SEM micrographs of Ni-Sn nanowire bundles with nanowire lengths of (c) 20 µm and (d) 40 µm.

Table 4.1 Agglomeration-induced inclination of nanowire arrays

h / μm	*a* / μm	*b* / μm	α / °
5	1.5	0.85	3.7
20	6	2.3	5.3
25	9.5	4	6.3
40	19	5	10

4.4 Performance Improvement of 3D Ni-Sn Nanowire Networks

4.4.1 Capacity Improvement

Table 4.2 Mass loading of active material in Ni-Sn nanowire electrodes

Straight nanowire arrays		3D nanowire networks	
Lengh / μm	Mass loading / mg ·cm^{-2}	Length / μm	Mass loading / mg ·cm^{-2}
5	0.58	5	0.73
20	3.21	20	3.4
25	5.08	25	5.18
40	9.47	40	9.86

To mitigate the serious agglomeration of straight Ni-Sn nanowire arrays and to improve the electrochemical performance of nanowire electrodes, in this study we propose to use 3D Ni-Sn

nanowire networks as Li-ion battery electrodes. We use a process similar to the synthesis of straight nanowire arrays for the preparation of 3D Ni-Sn nanowire networks, but with unconventional PAA templates synthesized using low-cost impure Al sheets. Nano-indentations in nanochannels of PAA templates have been reported when anodizing low-purity Al sheets and are regarded as defects [128, 129]. In this study, we utilize the defect-containing PAA templates to fabricate 3D Ni-Sn nanowire networks. To distinguish them from the conventional PAA templates used to fabricate straight nanowires, we call these defect-containing PAA templates synthesized from low-purity Al sheets 3D PAA templates.

Figure **4.3**(a) shows the cross-sectional FE-SEM micrograph of a 3D PAA template we prepared by anodizing a 99% Al sheet. Beside the parallel nanochannels with diameters of ~ 240 nm, there are abundant nano-indentations with a characteristic size of ~ 80 nm on the walls of the straight nanochannels. Some of the nanochannels are even connected by the indentations, as indicated by an arrow in Figure **4.3**(a). Such 3D PAA templates have been used to fabricate 3D Ni-Sn nanowire networks. Figure **4.3**(b) and Figure **4.3**(c) show top-view and cross-sectional images of a 3D Ni-Sn nanowire network fabricated by electrodepositing Ni-Sn alloy in a 3D PAA template and subsequently removing the template. In contrast to the straight Ni-Sn nanowire arrays shown in Figure **4.1**(a)-(c), the 3D Ni-Sn nanowires are uniformly spaced as shown in Figure **4.3**(b), which clearly demonstrates the elimination of agglomeration. We note that 3D Ni-Sn nanowire networks with different nanowire lengths from 5 μm to 40 μm have similar top-view images. In Figure **4.3**(c), the straight vertical nanowires are clearly connected with each other by the horizontal “bridges” which result from the nano-indentations in the 3D PAA templates. These bridges not only stiffen the nanowire network structures and prevent agglomeration, but also provide connections between nanowires to facilitate the electron

transport in the electrodes of Li-ion batteries [11, 165, 167-169]. In addition, the elimination of agglomeration in 3D Ni-Sn nanowire networks releases the stress at the roots of the nanowires, stabilizing the connection of the nanowires to the current collector.

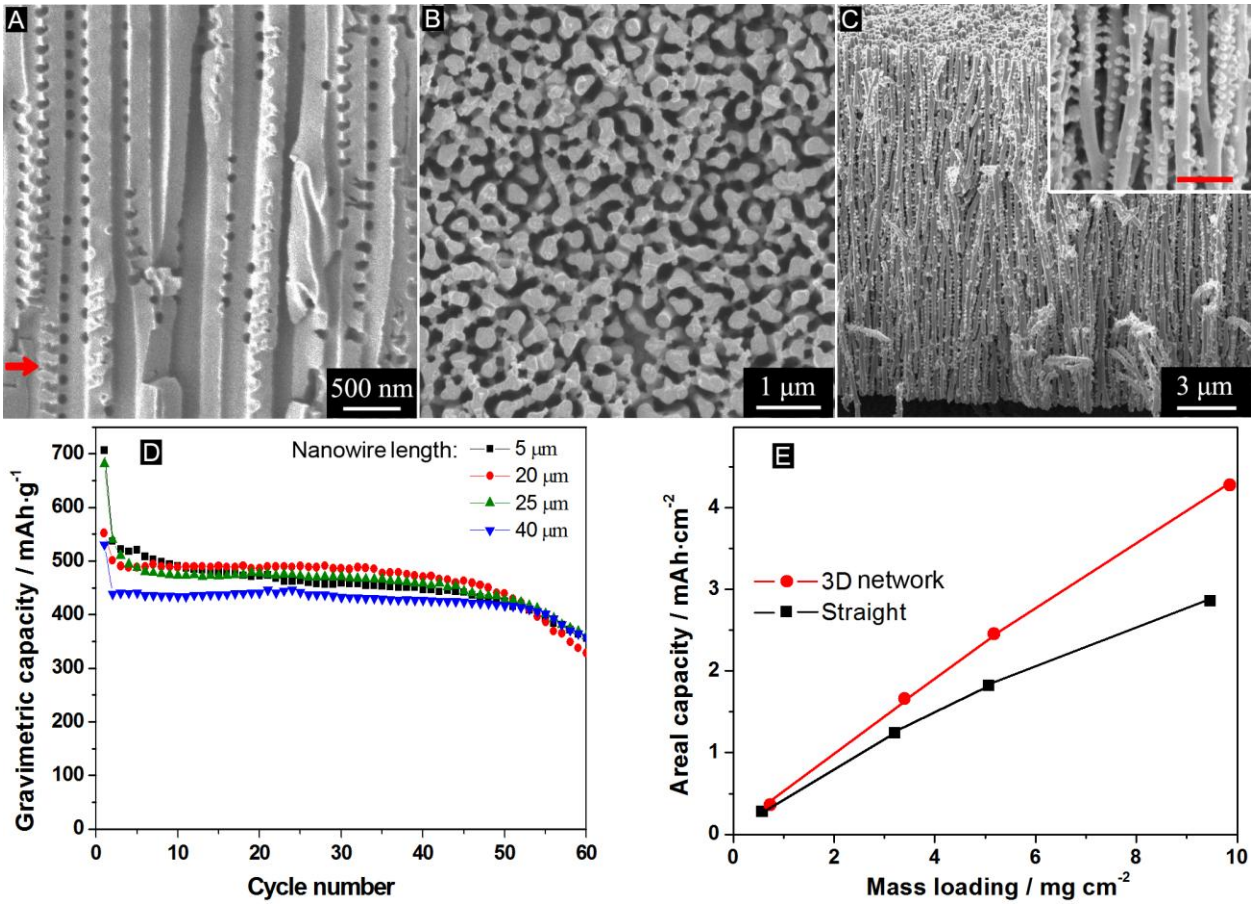

Figure 4.3 (a) Cross-sectional FE-SEM micrograph of a 3D PAA template. (b) Top-view and (c) cross-sectional FE-SEM micrographs of a 20-μm-long 3D Ni-Sn nanowire network. Inset: higher magnification image of nanowires with the scale bar indicating 1 μm. (d) Gravimetric capacities of 3D Ni-Sn nanowire networks with different lengths. (e) Areal capacity (at the 10th cycle) as a function of mass loading of active material in straight Ni-Sn nanowire arrays and 3D Ni-Sn nanowire networks. The test rate is set at C/5.

All the 3D Ni-Sn nanowire networks with different nanowire lengths from 5 μm to 40 μm deliver similar gravimetric capacity with similar cycle life as shown in Figure **4.3**(d), in contrast to the dramatic decrease of cycle life and gravimetric capacity when increasing the nanowire length in straight Ni-Sn nanowire arrays. Apparently, by eliminating agglomeration, the stress concentration at the roots of the nanowires due to bending has been effectively released, which improves the stability of the nanowires. High gravimetric capacity of ~ 450 mAh g^{-1} is retained in 3D Ni-Sn nanowire networks even when the nanowire length is increased to 40 μm. This improvement mainly comes from the preservation of the large specific surface area and the short Li-ion diffusion path in long nanowire networks [170]. The retention of high gravimetric capacity in long 3D Ni-Sn nanowire networks enables the realization of high areal capacity by increasing the mass loading of the active material.

Figure **4.3**(e) shows that the areal capacity of the 3D Ni-Sn nanowire networks increases almost linearly with the mass loading of active material (see Table **4.2** for the mass loadings of nanowires with different lengths). In contrast, the rate of the areal capacity increase drops when the mass loading is increased in the straight Ni-Sn nanowire array electrodes. For example, the areal capacity of the 40-μm-long 3D Ni-Sn nanowire network is 4.3 mAh cm^{-2}, which is 1.5 times that of the 40-μm-long straight Ni-Sn nanowire arrays (2.8 mAh cm^{-2}), although the mass loadings are similar in these two long nanowire samples.

4.4.2 Galvanostatic Charging/Discharging Curves of the Nanowire Electrodes

The main phase in the intermetallic Ni-Sn is Ni_3Sn_4 alloy. The electrochemical processes of Ni_3Sn_4 are:

$$Ni_3Sn_4 + 17.6Li^+ + 17.6e^- \rightarrow 4Li_{4.4}Sn + 3Ni \quad (4.1)$$

$$Li_{4.4}Sn \rightarrow Sn + 4.4\,Li^+ + 4.4e^- \quad \text{(charge)} \quad (4.2)$$

$$Sn + 4.4\,Li^+ + 4.4e^- \rightarrow Li_{4.4}Sn \quad \text{(discharge)} \quad (4.3)$$

Figure **4.4** shows the galvanostatic charging/discharging curves of 20-μm-long straight Ni-Sn nanowire arrays and 3D Ni-Sn nanowire network against Li metal counter electrode at a current density of 50mA/g. The two structures show similar potential profile. Large irreversible capacity drops can be observed in both samples during the first cycles, due to two possible reasons: 1) the irreversible activation step of Ni-Sn alloy (chemical equation (4.1)); 2) formation of solid-electrolyte-interphase(SEI) [96]. After the second cycle, reversible capacities of the electrodes are observed, corresponding to the chemical equations (4.2) and (4.3) [3]. Broad voltage bands between 1.0V and 0.01V are consistent with the observations for the electrodeposited Ni-Sn nanostructured electrodes in literature [94, 147, 171].

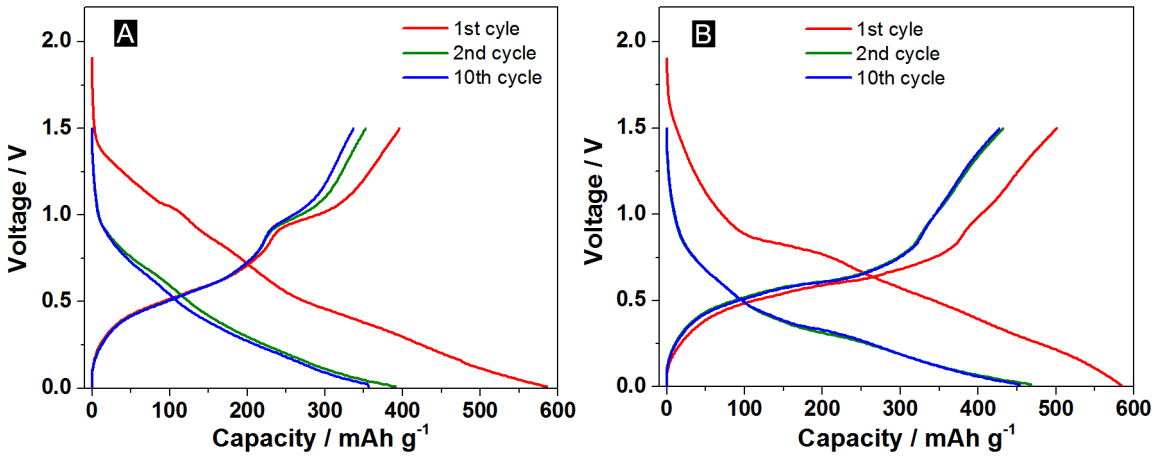

Figure 4.4 Galvanostatic charging/discharging curves of 20 μm (a) straight Ni-Sn nanowire arrays and (b) 3D Ni-Sn nanowire network against Li metal counter electrode at a current density of 50mA/g.

4.4.3 Rate Capability

Besides the enhanced capacity and much longer cycle life, the 3D Ni-Sn nanowire networks also show much better rate capability than the straight nanowire arrays, as shown in Figure **4.5**. When increasing the test rate from C/10 to 6C, the 20-μm-long straight Ni-Sn nanowire array electrode can only retain 15% of its initial capacity. In contrast, the 20-μm-long 3D Ni-Sn nanowire network electrode can keep 72% of its initial capacity. The excellent rate capability of 3D Ni-Sn nanowire networks is a result of fast Li-ion transfer to the electrode due to the stable nanoscale space between nanowires, fast electrode reactions due to the large surface area, and the short Li-ion diffusion paths due to the small diameters [38].

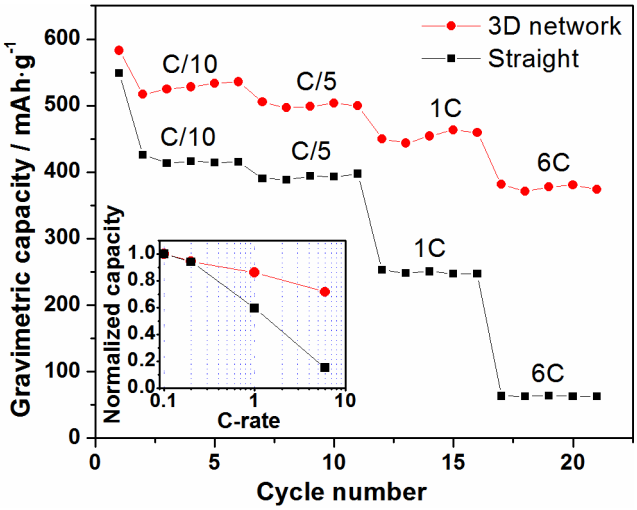

Figure 4.5 Areal discharging capacities of the 20-μm-long straight Ni-Sn nanowire array and 3D Ni-Sn nanowire network at different test rates. Inset: normalized capacity versus test rate.

4.5 Summary of 3D Ni-Sn Nanowire Network

In summary, to mitigate the agglomeration of nanowire arrays, we have successfully fabricated 3D Ni-Sn nanowire networks. With preservation of the uniform spacing between nanowires and the nanoscale Li-ion diffusion paths, we have realized linear increase of areal capacity with respect to mass loading of active material in 3D Ni-Sn nanowire network electrodes. The cycle life of the 3-D nanowire network electrodes has been prolonged due to the release of the stress at the roots of the self-supporting nanowire networks. An areal capacity as high as 4.3 mAh cm^{-2} has been demonstrated in the 3D Ni-Sn nanowire network electrode with a nanowire length of 40 μm, which is 1.5 times that of the straight nanowire array electrode with the same length. The cycle life has been doubled to be longer than 50 cycles. In addition, the 3D Ni-Sn nanowire network exhibits an excellent rate capability with 72% of the capacity retained when the test rate increases from C/5 to 6C.

4. 3D Carbon Nano-Network

5.1 Introduction to 3D Nanoporous Carbon Networks

The rapid development of portable electronics and electric vehicles has led to a great demand for high energy density, high power, and long cycle-life lithium-ion batteries (LIBs). Since energy is released or stored in LIBs by the flow of Li ions and electrons between the anode and cathode electrodes [7, 172, 173], the efficient transport of Li ions and electrons is the key to the energy and power density of LIBs. Three-dimensional (3D) micro/nanostructured networks present great benefits for high performance LIBs, such as a large surface area for fast Li ion

insertion/extraction, interconnecting paths for fast electron conduction, and high porosity for fast electrolyte diffusion and volume change alleviation [31, 32]. For example, the ultra-high rate of over 1000C LIB was a result of using porous Ni framework with pore size of ~ 2 μm loaded with lithiated MnO_2 [11]. High areal capacity and excellent rate performance have also been achieved in $LiCoO_2$ [174], Fe_3O_4 [120], TiO_2 [175], silicon [176], *etc.* with the help of 3D metal networks [33-38]. However, the use of metallic conducting networks in these 3D electrodes comes with the intrinsic penalty of heavy inactive materials, which significantly reduces the gravimetric capacity in LIBs. Thus, 3D porous carbon, which has low mass density with interpenetrating network that facilitates both ion and electron transport, has been widely explored to overcome the density barrier [39-46]. Carbon aerogels are a kind of porous carbon consisting of meso-pores with a size of <10 nm, which offer very high surface areas for LIB and supercapacitors [39, 47-50]. The diffusion of the electrolyte and transport of ions are greatly impeded due to the small pores in carbon aerogels, especially when the electrodes are thicker than 10 μm [51], which greatly harms the rate capability of the electrodes [52-54]. For example, mesoporous carbon/Co_3O_4 composite maintained only 32% of its capacity when the test current was increased by 10 times from 200 mA g^{-1} to 2000mA g^{-1} [54]. As such, porous carbon with large pore sizes (> 1 μm) were developed to introduce more porosity to the carbon network and to improve the rate capability of electrodes [55, 56]. A $LiFePO_4$/carbon composite electrode with 1 μm to 5μm pores retained 89% of its capacity when the test rate was increased by 10 times from C/10 to 1C [57, 58]. However, accompanying the improved power performance in these electrodes, the overall volumetric capacity and energy density of such electrodes are greatly reduced due to the large size of the pores and the thin active materials, which leaves most space in the electrodes empty.

A low mass density conducting network with pore size in the range of hundreds of nanometers are in great need which could potentially enhance the ion and electron transport without sacrificing energy density. Some efforts have been made to develop 3D conducting networks with pore size in the range of several hundred nanometers. Porous carbon with pore size of ~ 300 nm encapsulated with sulfur retained 52% of its capacity when test rate was increased by 10 times from C/5 to 2C [59]. Nanoparticles entrapped in carbon inverse opal with 220 nm diameter pores maintained 50% of the capacity when the test current increased 10 times from 1 $A \cdot g^{-1}$ to 10 $A \cdot g^{-1}$ [60]. All these previous efforts demonstrate the importance of the 3D conducting network with appropriate pore size in the LIB electrodes.

In this section, we develop a novel 3D carbon nano-network as highly efficient current collector for the high-power and long-cycle-life LIB electrodes. The 3D carbon nano-network, synthesized by chemical vapor deposition (CVD) of carbon on 3D PAA templates [177], consists of parallel trunk carbon tubes connected together by numerous branch tubes to form an interconnected network, as shown in Figure **5.1**(a). The diameters of both the trunk carbon tubes and the branch tubes are in the range of hundreds of nanometers, which are ideal as 3D porous current collector for the LIB electrodes as proposed. The thickness of these carbon tube walls is controllable from a few nanometers to tens of nanometers depending on the carbon CVD time. The active material, TiO_2, is then loaded on the 3D carbon nano-network using the atomic layer deposition (ALD) process. A large areal capacity of ~ 0.37 mAh cm^{-2} is achieved due to the large areal mass loading of the 60-μm thick 3D C/TiO_2 electrodes. At a test rate of C/5, the electrode with 18 nm TiO_2 coating on the 3D carbon nano-network delivers a high gravimetric capacity of ~ 240 mAh g^{-1} using the mass of the whole electrode in the calculation. A long cycle life of over 1000 cycles is demonstrated at 1C with a capacity retention of 91%. The effects of

the electrical conductivity of carbon nano-network, ion diffusion in the active material, and the electrolyte permeability on the rate performance of these 3D C/TiO_2 electrodes are systematically studied, which gives insights on high performance LIB electrodes with 3D architecture.

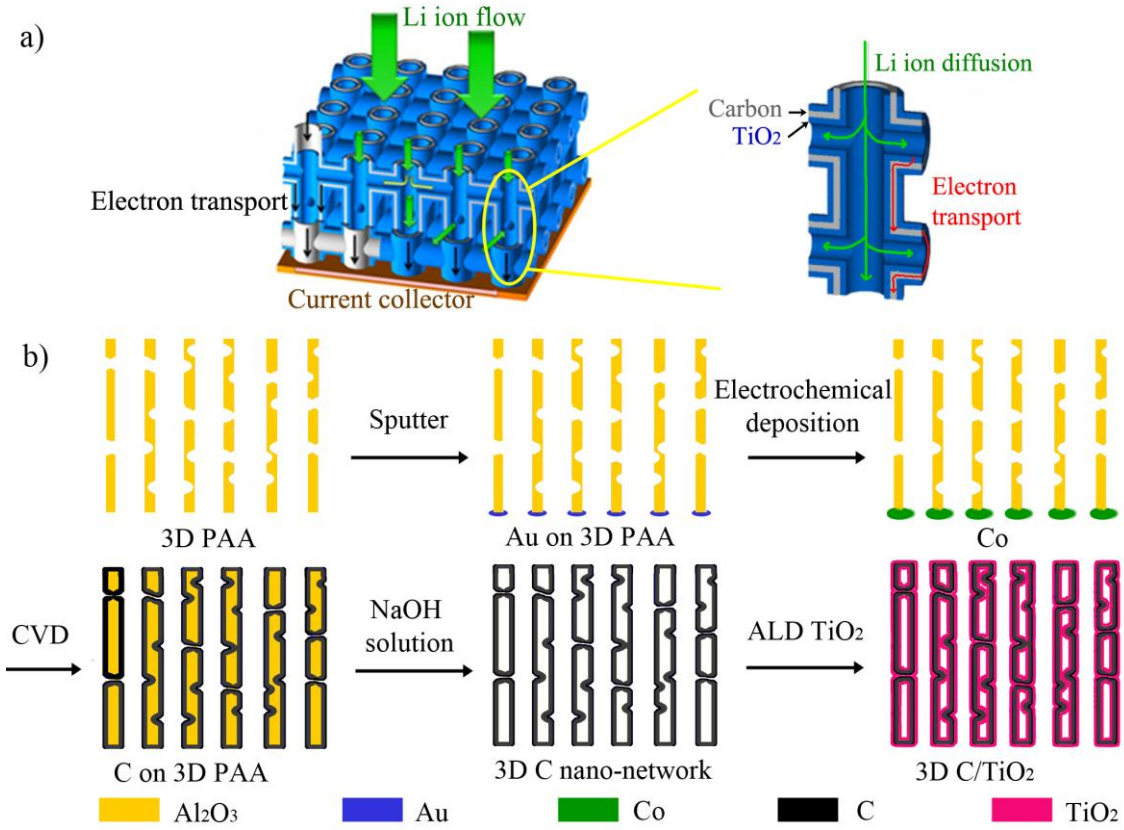

Figure 5.1 (a) Schematics of the 3D C/TiO_2 electrode. (b) Fabrication process of 3D C/TiO_2 electrode.

5.2 Fabrication of 3D Carbon Nano-Network

5.2.1 Sample Preparation

A 3D carbon nano-network was fabricated through chemical vapor deposition (CVD) of carbon on the 3D porous anodic alumina (PAA) templates. In an earlier work, we discussed the fabrication of 3D PAA templates using low purity 1000 series (99% purity, McMaster 9060K16) Al foils [178]. The 3D PAA template was first sputtered with a 100 nm thick Au layer for electrical conductance and then electrodeposited with Co at -1.2V *vs.* Ag/AgCl for 1 min as the catalyst for the later carbon CVD process [179]. The CVD process with gas flow of 262 sccm Ar, 90 sccm H_2, and 60 sccm C_2H_4 at 700 °C is used to uniformly deposit carbon on the 3D PAA template at ambient pressure.[180] The PAA template was then removed by wet etching of Al_2O_3 in 1M NaOH solution for 5 hours, which leaves the free standing 3D carbon nano-network ready to be used for loading active materials to form 3D nanostructured electrodes after supercritical drying. The thickness of the CVD carbon layer is quite linear with the deposition time. 3.5 hours of CVD is corresponding to 3 nm thick carbon layer coating.

Atomic layer deposition (ALD) is used to load the active LIB material, TiO_2, on the 3D nanoporous carbon in kinetic mode with ultra high purity (UHP) grade N_2 as the carrier gas. Base pressure of the reactor was kept below 1 Torr. An Al_2O_3 (alumina) seed layer of 2 nm was pre-deposited by 50 cycles of sequential dosing of trimethylaluminum (TMA) for 150 ms and water for 750 ms at 150 ℃. This layer is needed to ensure proper TiO_2 nucleation [178]. The thickness of this seed layer needed to be as thin as possible to reduce the electrical resistance caused by it. In Figure **5.2**(a), TEM image of 20 cycles of Al_2O_3 coating on the 3D carbon was shown. The Al_2O_3 forms particles and leaves the carbon tube surface incompletely covered. This would cause non-uniform coating of TiO_2. To increase the coverage, fifty cycles of Al_2O_3 are

ALD coated as the seed layer for better nucleation and growth of the TiO_2 layer. As shown in Figure **5.2**(b)**,** fifty cycles of ALD coated Al_2O_3 uniformly covers two interconnected carbon tubes. Thickness of tube wall, which includes one layer of carbon and two layers of ALD coated Al_2O_3, is around 7 nm. TiO_2 was then coated with sequential dosing of 200 ms Titanium tetrachloride ($TiCl_4$) and 750 ms water at 150 ℃.

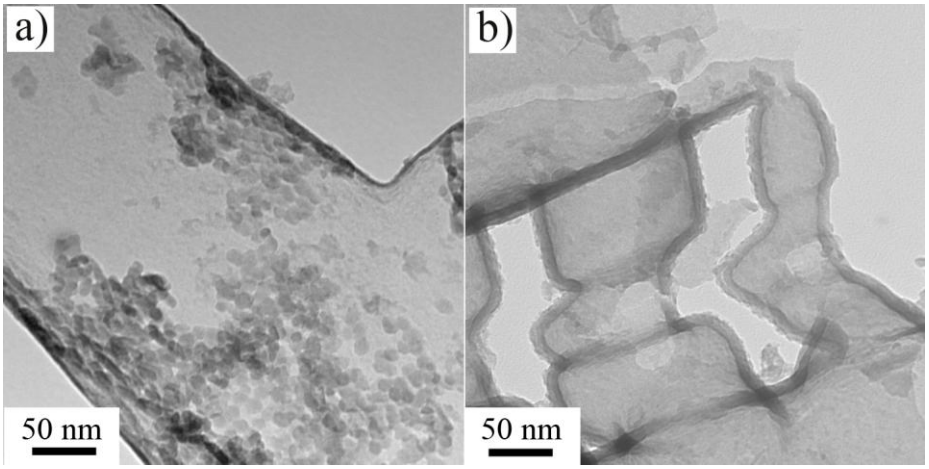

Figure 5.2 TEM images of the 3D carbon network with (a) 20 cycle and (b) 50 cycle Al_2O_3 ALD coating.

5.2.2 Structural and Electrical Characterization

The field emission scanning electron microscope (FE-SEM, JEOL JSM-7401F) was employed to study the morphology of the 3D carbon nano-networks and the 3D C/TiO_2 electrodes. Cross-sectional images of the 3D nano-networks were taken by tearing the samples apart with tweezers to expose fresh cross sections and mounting them on a tilted SEM stage. Transmission electron microscopy (TEM, Philips CM-10) and high resolution transmission electron microscopy (HR-TEM, FEI Tecnai F30) were used for structural characterizations.

Selected area electron diffraction (SAED) pattern was operated under 300keV electron beam with camera length of 1.2m. Electrical conductivities of the 3D nano-networks were tested with the four point probe method (Kulicke & Soffa model 3007). The electrodes after electrochemical cycling test were carefully taken out of the coin-cell battery in the glovebox and soaked and washed in DMC for 5 times to remove the electrolyte before characterization.

5.2.3 Electrochemical Characterizations

The as-prepared 3D carbon nano-network and 3D C/TiO_2 nanostructured anodes were tested by assembling half-cell in the CR2032 coin-type cell with an electrolyte containing 1 M $LiPF_6$ in ethylene carbonate (EC)/dimethyl carbonate (DMC) (1:1 volume ratio, Aldrich) and with Li foil (Alfa Aesar) as counter-electrode. The CR2032 coin-type cells were assembled in an argon-filled glove box system (Vacuum Atmosphere Nexus model) and tested with a computer controlled potentiostats/galvanostats system (MTI, 5V1mA). The discharge-charge experiments were performed galvanostatically within the voltage window of 1.0 - 2.6 V (vs. Li/Li+).

5.3 Structural and Electrical Characterization of 3D Carbon Nano-Network and 3D C/TiO_2 Electrodes

Figure **5.3**(a) shows the optical image of a 20 cm^2 free-standing 3D carbon nano-network. The size of these samples is scalable depending on the size of starting Al foils for PAA template fabrications. The sample has a thickness of 60 μm, which is determined by the thickness of the 3D PAA template. Figure **5.3**(b) shows the cross-sectional scanning electron microscope (SEM) image of a 3D carbon nano-network after 3.5 hour CVD carbon coating. The 3D carbon network consists of parallel trunk tubes (colored to red on left side), which are connected together by branch tubes (colored to green on left side) to form a freestanding film. No agglomeration of the

carbon tubes were observed due to the support of the branch tubes between the neighboring carbon tubes. The interconnection of carbon tubes inside the sample was also readily observable by the transmission electron microscope (TEM) characterization, as shown in Figure **5.3**(c) and 1d. The tube diameter is ~ 250 nm, which is dictated by the characteristics and the fabrication process of PAA templates [177]. The high-resolution TEM (HRTEM) image in Figure **5.3**(e) shows partially crystalline structure of the carbon layer. The selected area electron diffraction (SAED) pattern in the inset figure is consistent with the HRTEM image, showing both amorphous diffraction rings and crystalline diffraction points.

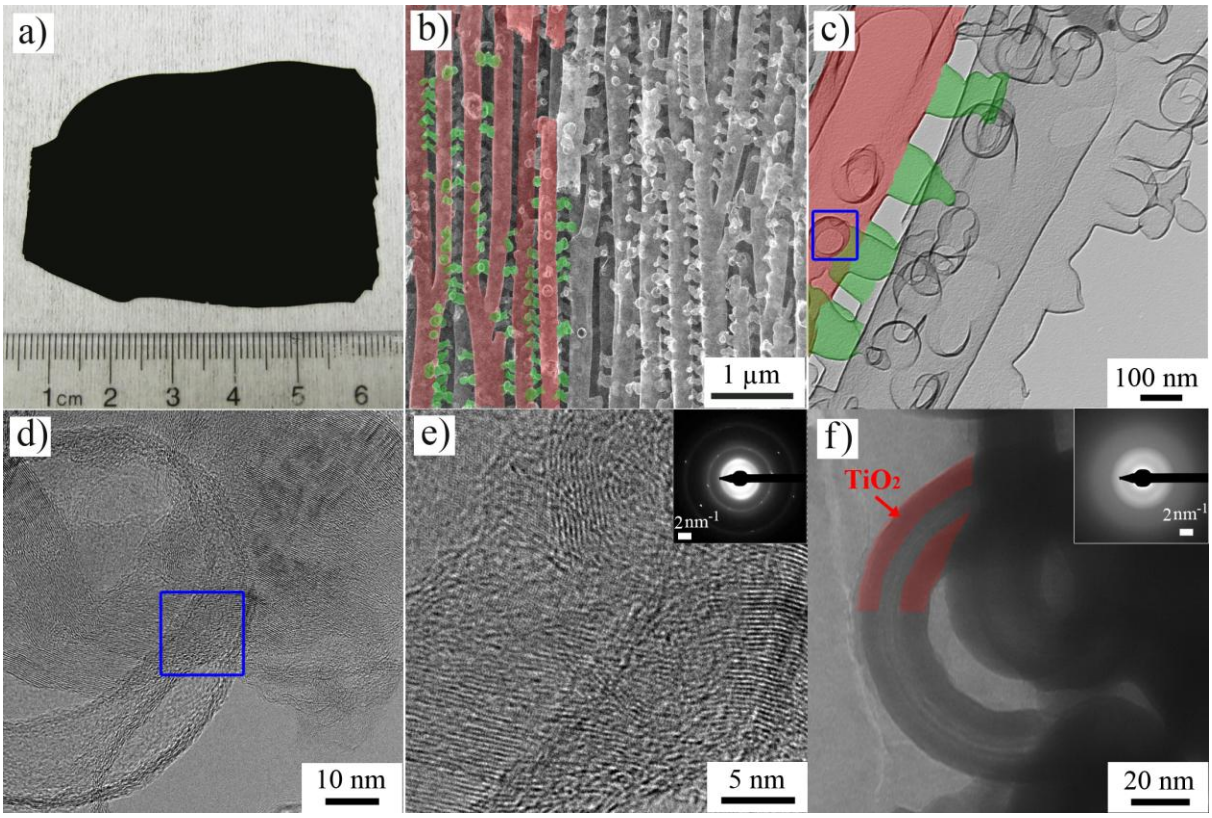

Figure 5.3 (a) Optical image of a free-standing 3D carbon nano-network. (b) cross-sectional SEM image and (c) TEM image of the 3D carbon nano-network from 3.5 hours of carbon CVD. (d) & (e) HR-TEM image of the 3D carbon nano-network from the marked area in (c) and (d),

respectively. Inset: electron diffraction pattern of the 3D carbon nano-network. (f) HR-TEM image of the 3D carbon nano-network with ALD TiO_2 coating. Inset: electron diffraction pattern of the 3D C/TiO_2 nano-network.

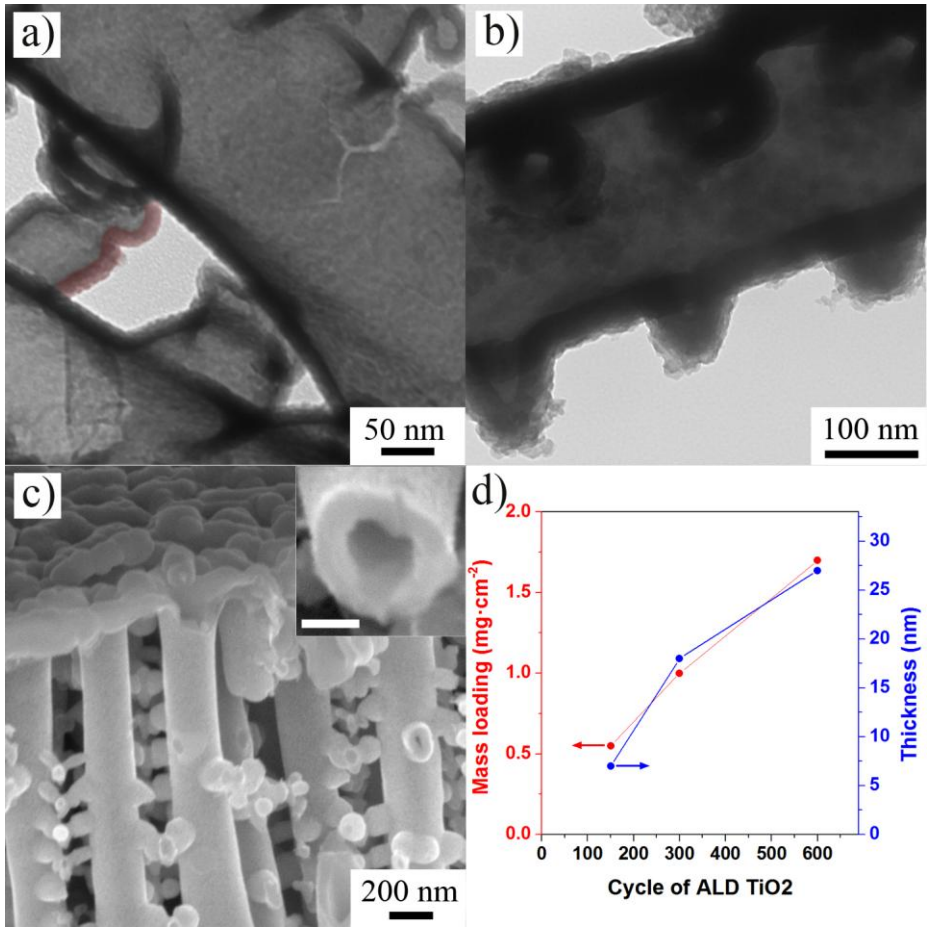

Figure 5.4 TEM images of the 3D carbon network with (a) 150 cycles, (b) 300 cycles, and (c) 600 cycle ALD TiO_2 coating. Inset in (c): cross-sectional view of a C/TiO_2 tube in c) with the scale bar of 100 nm. (d) Areal mass loadings and thicknesses of ALD TiO_2 vs. ALD cycle number.

TiO_2 layers with different thicknesses were coated on the 3D carbon nano-networks using the atomic layer deposition (ALD) process [181]. To facilitate the uniform ALD TiO_2 process, an

Al_2O_3 (alumina) seed layer of 2 nm was pre-deposited. Figure **5.3**(f) shows a HR-TEM image of the layered structure with the 7 nm TiO_2 coating with ALD coating of 150 cycles. The SAED pattern in inset Figure indicates the amorphous nature of TiO_2 coating, which is due to low deposition temperature (150 ℃) in the ALD coating process [182, 183].

Thickness of TiO_2 was increased to 18 nm and 27 nm by increasing the ALD coating cycle number to 300 and 600, respectively. Figure **5.4**(a) shows that the thickness of the tube wall is around 21 nm after 150 cycles of ALD TiO_2 coating. Subtracting the thickness of the carbon layer of 3 nm and the thickness of the 50 cycle Al_2O_3 seed layer of 2 nm (Figure S4b), the thickness of 150 cycles of ALD TiO_2 coating is around 7 nm. Similarly Figure **5.4**(b) shows that thickness of 300 cycle ALD TiO_2 coating is ~ 18 nm while Figure **5.4**(c) shows thatthe thickness of 600 cycles of ALD TiO_2 coating layer is around 27 nm , with the total wall thickness of 61 nm. With the 27 nm TiO_2 coating, the space between and inside the carbon tubes narrower but is still preserved, considering the tube diameter of 250 nm. Figure **5.4**(d) shows the thickness and mass loading of the TiO_2 layers corresponding to the number of the ALD coating cycles. With increased cycles, the thickness and mass loading increase with similar rates.

As the conducting network for LIB electrodes, the 3D carbon nano-network is expected to have high electrical conductivity. The in-plane (vertical to the main carbon tube direction) electrical conductivity of the 3D carbon nano-network with 3 nm thick of carbon layer was tested to be ~ 110 $S \cdot m^{-1}$ using the four-probe method, as shown in Figure **5.5**(b). The electrical conductivity of the 3D carbon nano-network can be readily tuned by adjusting the thickness of carbon coating *via* changing the CVD time. After 10 hours of CVD, the thickness of the carbon layer is increased to 8 nm and the electrical conductivity is increased to 159 $S \cdot m^{-1}$. In a typical LIB, the bottleneck of the transport comes from the ionic conductivity of the electrolyte, (1 M

$LiPF_6$ in ethylene carbonate (EC)/dimethyl carbonate (DMC) (1:1 volume ratio, Aldrich)), which is ~ 10^{-1} $s \cdot m^{-1}$ [184, 185]. Here, the electrical conductivity of the as-obtained carbon nano-network is much greater than the ionic conductivity. Thus, it should be able to meets the requirement of electron transport for high power performance in LIB electrodes [186]. Study on phospho-olivines shows that when the electrode conductivity increase from 10^{-7} $s \cdot m^{-1}$ to 10^{-1} $s \cdot m^{-1}$ through doping, the rate capability was significantly increased (about 57% capacity retention from C/10 to 10C) [187]. By incorporating the 3D carbon nano-network with low conductivity active materials, their rate capabilities should be increased by increasing the electrical conductivity.

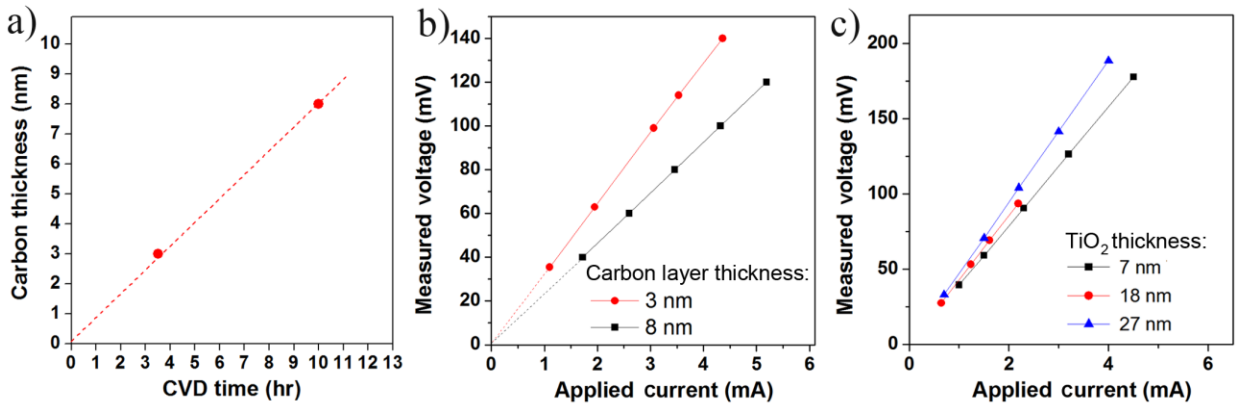

Figure 5.5 (a) Thickness of carbon layer with different CVD times. (b) Measured electrical conductivity of 3D carbon networks with different carbon layer thicknesses. (c) Current-voltage curve of 3D C/TiO_2 electrodes with 2 nm Al_2O_3 coating and different ALD TiO_2 coating thicknesses on a 3nm carbon nano-network.

As shown in Figure **5.5**(a), the carbon layer is around 3 nm thick after 3.5 hour CVD. After 10 hours of CVD, the thickness of the carbon layer is increased to around 8 nm. Figure **5.5**(b) presents the current-voltage curves of the 3D carbon networks with different carbon layer

thicknesses, using the four-point electrical measurement. Electrical conductivity of the 3nm thick 3D carbon network is ~ 110 s m^{-1}. The electrical conductivity increases to ~ 159 s m^{-1} when the carbon layer thickness is increased to 8nm. Figure **5.5**(c) shows the measured current-voltage curves of the C/TiO_2 electrodes with different TiO_2 thicknesses after coated with 2 nm Al_2O_3 ALD seeding layer on 3 nm carbon nano-network. The electrical conductivity values are 93.5 s m^{-1}, 86.2 s m^{-1}, and 78.1 s m^{-1} for 7 nm, 18 nm, and 27 nm TiO_2 layers, respectively.

To evaluate the performance of a 3D carbon nano-network as the 3D conductive network in an electrochemical cell, we conducted proof-of-concept studies using TiO_2 as the electrochemically active material, since TiO_2 has been considered as an attractive material for use in LIB anodes due to its low cost, safety, and environmental benignity [188, 189]. The electrical conductivity of amorphous TiO_2 is very low, ~ 10^{-12} s·m^{-1}, which significantly limits its electrochemical performance [190]. Many efforts have been made to increase the electrical conductivity of TiO_2-based anodes by carbon coating, mixing with single-wall carbon nanotubes, mixing with graphene, *etc.* [191-194]. In this work, by incorporating the 3D conducting carbon nano-network with TiO_2, the 3D C/TiO_2 electrodes have conductivities in the range of 78.1-93.5 s·m^{-1}, as shown in Figure **5.5**(c).

5.4 Areal and Gravimetric Capacities of 3D C/TiO_2 Electrodes

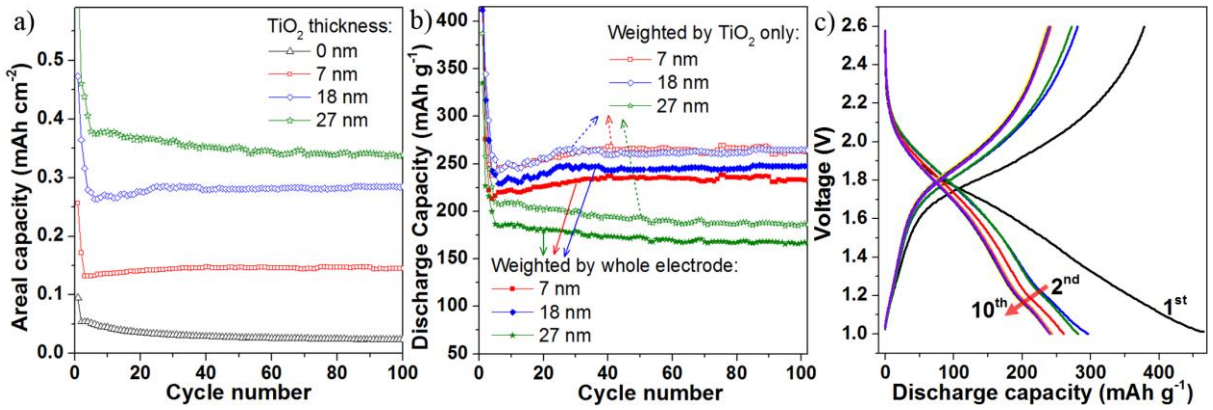

Figure 5.6 (a) Areal capacities of the 3D C/TiO_2 electrodes with different TiO_2 thicknesses on 3 nm 3D carbon nano-network where Coulombic efficiency of the 3D C/TiO_2 electrodes with 7 nm TiO_2 coating on 3 nm 3D carbon nano-network is shown to the right. (b) Gravimetric capacities of the 3D C/TiO_2 electrodes with different TiO_2 thicknesses on 3 nm 3D carbon nano-network. (c) Galvanostatic discharging/charging curves of the 3D C/TiO_2 electrode with 7 nm TiO_2 coating on 3 nm 3D carbon network. Test rate is C/10 for the first two cycles and then C/5 for the rest of the curves.

The electrochemical performances of the 3D C/TiO_2 electrodes with different TiO_2 thicknesses were studied systematically. As shown in Figure **5.6**(a), the 3D carbon nano-network with thickness of 60 μm delivers an areal capacity of ~ 0.03 mAh cm^{-2} without any TiO_2 coating at C/5. With the ALD TiO_2 coating, the areal capacities of the electrode were significantly increased to ~ 0.15 mAh cm^{-2} for the 7 nm thick TiO_2 sample and ~ 0.37 mAh cm^{-2} for the 27 nm thick TiO_2 sample. In the previous works, anodized 9 μm long TiO_2 nanotube arrays performed an areal capacity of 0.45 mAh cm^{-2} at C/10 [195], and anodized 8.2 μm long TiO_2 nanotube arrays delivered an areal capacity of 0.15 mAh cm^{-2} at C/2 [196]. Although these nanotube arrays show high areal capacities, their gravimetric capacities and rate capabilities are

very poor due to the lack of electrical conducting medium. For example, the 9 μm long TiO_2 nanotubes delivered 170 mAh g^{-1} at C/10 and an even smaller capacity of 90 mAh g^{-1} at 2C [195]. Some efforts to increase the rate capability have been made by incorporating 3D conducting networks into TiO_2 electrodes. A 3D electrode of TiO_2 on Al nanorods reaches 0.01 mAh cm^{-2} at C/5[175] and a 32 μm thick 3D Ni nanowire network coated with ALD TiO_2 delivered an areal capacity of 0.13 mAh cm^{-2} at C/4 [178]. Although such 3D nanostructured TiO_2 electrodes achieved high areal capacities, the heavy metal conducting networks reduce the weight percentage of the active materials and thus reduced the overall gravimetric capacity of the electrodes. In comparison, our novel lightweight 3D carbon nano-network can potentially realize high areal capacity, high gravimetric capacity, and high rate capability simultaneously.

In Figure **5.6**(b), the gravimetric capacities of TiO_2 in the 3D nanostructured C/TiO_2 electrodes were calculated by subtracting the areal capacity of the 3D carbon network from the electrodes' areal capacity and divided by the mass loading of TiO_2. The gravimetric capacities of 7 nm and 18 nm thick TiO_2 coatings showed a similar value of ~ 260 mAh g^{-1} at C/5. This value is higher than earlier works on pure TiO_2 nanotubes (223 mAh g^{-1} at 1C) [197], TiO_2/carbon core-shell electrodes (161 mAh g^{-1} at C/5) [198], and porous TiO_2 nanowire arrays (191 mAh g^{-1} at 1C), benefitting from the conducting network [199]. For the 3D C/TiO_2 with the TiO_2 thickness of 27 nm, the reversible gravimetric capacity becomes smaller, ~ 195 mAh g^{-1}, than that of the thinner ones.

Figure **5.6**(b) shows the gravimetric capacity based on the whole electrode when we count in the capacity and mass of the 3D carbon network, which is ~ 228 mAh g^{-1} for the 7 nm TiO_2 electrode and ~ 235 mAh g^{-1} for the 18 nm TiO_2 electrode. By using light-weight carbon instead of a metallic conducting network, the gravimetric capacity of the whole electrode is increased

efficiently compared to earlier works on nanostructured TiO_2 electrodes. With only 15 wt% active material TiO_2 and 81 wt % inactive Ni, the overall gravimetric energy density of the electrodes was only ~ 37 mAh g^{-1} [178]. The gravimetric capacities based on whole electrodes are only 87 – 175 mAh g^{-1} in other nanostructured TiO_2 electrodes such as nanocrystallites, nanoparticle, nanowires, and nanotubes with 50% - 70% weight percentage of TiO_2 where carbon black and polymer binders are often added [200-205]. By using a light-weight carbon conducting network and eliminating polymer binder, the gravimetric capacity of the whole electrode is efficiently increased with our 3D C/TiO_2 electrodes.

Figure **5.6**(c) shows the galvanostatic discharging/charging curves of the 3D C/TiO_2 electrode with 3 nm thick carbon and 7 nm thick TiO_2 tested at C/5. Due to the amorphous nature of the ALD deposited TiO_2 [178], the electrode shows large irreversible discharging capacity at the first cycle with a broad plateau within 1.1 V- 1.7 V, which is different from crystallized TiO_2, which has a typical voltage plateau at 1.7 V [199]. Large irreversible capacities in the first cycles are due to the formation of a solid-electrolyte interface [206-208]. We also note that the capacity in the first cycle is larger than the theoretical capacity of TiO_2, 330 mAh·g^{-1}, due to the storage of Li ions in the grain boundary and interfaces of the nanostructured TiO_2 [209].

5.5 Cycle Lives of 3D C/TiO_2 Electrodes

Although the conducting additives and polymer binders are not used in the 3D C/TiO_2 electrodes, the as-obtained electrodes still show very long cycle life. Figure **5.7**(a) shows the prolonged electrochemical test of the 3D C/TiO_2 electrodes with different TiO_2 thicknesses at the test rate of 1C. The 3D C/TiO_2 electrode with 7 nm thick ALD TiO_2 shows very stable

performance and lasts more than 1000 cycles. However, as the thickness of the TiO_2 increases, the cycle life of the electrodes decreases. The capacity starts to degrade after 700 cycles for the 18 nm TiO_2 electrode and after 400 cycles for the 27 nm TiO_2 electrode. For comparison, 3D TiO_2 nano-network without any conducting network was fabricated by depositing TiO_2 on 3D PAA template through ALD and removing the 3D PAA template with NaOH solution. Without a 3D carbon nano-network, the 3D TiO_2 electrode with 7 nm TiO_2 layer delivers a small gravimetric capacity ~ 100 mAh g^{-1}, which degrades quickly to less than 50 mAh g^{-1} in 180 cycles. The fast degradation was also observed in earlier studies on nanostructured TiO_2 electrodes, which are plotted in the same figure for comparison [170, 200]. This comparison clearly proves that the 3D carbon network helps prolong the cycle life of the 3D C/TiO_2 electrodes.

An *ex-situ* TEM study of the electrodes was conducted to observe the change of the electrodes during the prolonged electrochemical test. The 3D C/TiO_2 electrode with 7 nm TiO_2 coating was carefully taken out of the coin cell after 150 cycles of electrochemical test and characterized with TEM. Figure **5.7**(b) shows that the tubular structures are retained in the electrodes after 150 cycles, confirming the structural stability of the 3D C/TiO_2 electrode. The TiO_2 layer is still attached to both inside and outside of the carbon tubes. The total wall thickness increases to 33 nm with the TiO_2 layer thickness increases to 12 nm (the middle layer consisted of carbon and ALD Al_2O_3 is increased to 9 nm) after lithiation. Figure **5.7**(c) shows the TEM images of the 3D C/TiO_2 electrode with 27 nm TiO_2 after 500 cycles. The carbon tube structure still remained, but some of the tubes lost the TiO_2 layer and the corresponding wall thickness reduced to ~ 14 nm. TiO_2 falling off from the carbon tubes leads to the capacity reduction.

Although the volume change of TiO_2 is only 3%, the repeating insertion/extraction of Li ions can cause the detachment of TiO_2 layer from the carbon network [210, 211].

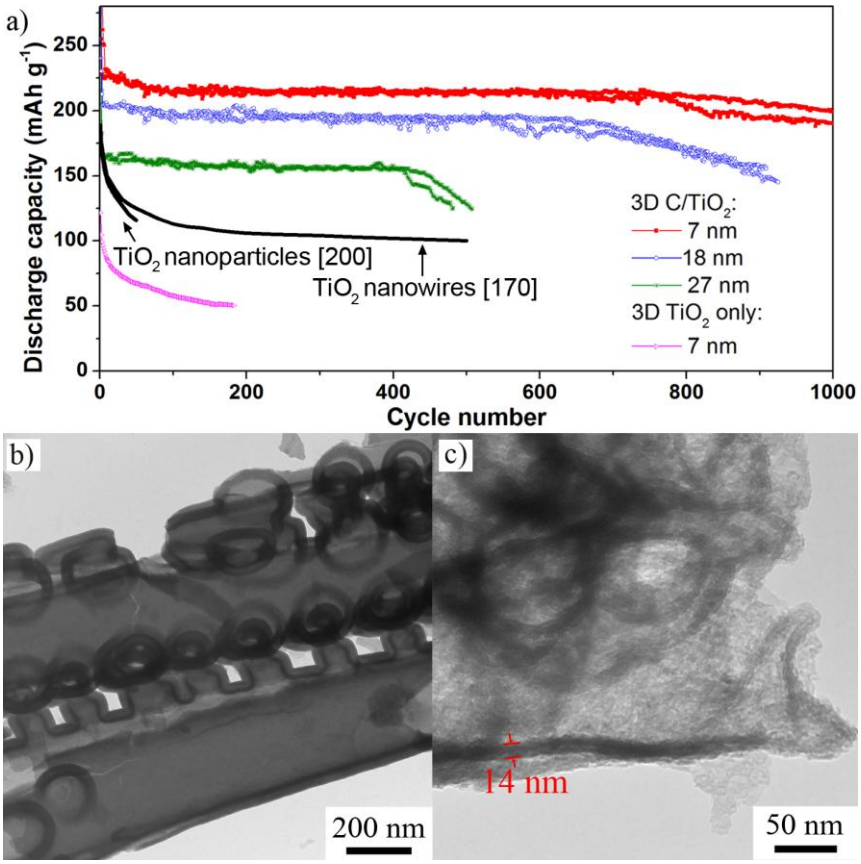

Figure 5.7 (a) Stability of the 3D C/TiO_2 electrodes with different thicknesses of TiO_2 on 3 nm carbon nano-network at test rate of 1C. Also shown on the figure are TiO_2 nanostructures from references [170, 200], and 3D TiO_2 without 3D carbon nano-network. (b) TEM image of the C/TiO_2 electrode with 7.5 nm TiO_2 on 3 nm C nano-network after 150 cycles. (c) TEM image of the C/TiO_2 electrode with 27 nm TiO_2 on 3 nm C nano-network after 500 cycles.

5.6 Rate Capabilities of 3D C/TiO_2 Electrodes

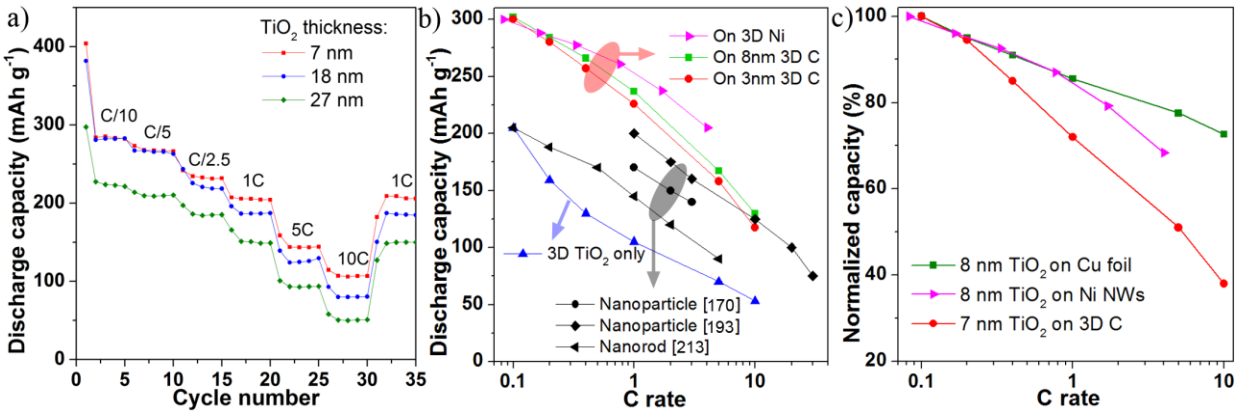

Figure 5.8 (a) Rate capability of 3D C/TiO_2 electrodes with different thicknesses of ALD TiO_2 coatings on 3 nm carbon nano-network. (b) Rate capabilities of TiO_2 electrodes with different conducting networks. (c) Rate capability of 3D C/TiO_2 electrodes with 3 nm carbon nano-network compared to the rate capability of TiO_2 film and 3D Ni/TiO_2.

One of the greatest advantages of the 3D nanostructured electrode is the ability to enhance the transport of Li ions and electrons and improve the rate performance. Although the point has been proven in other works, the detailed influence in the kinetic process was not clearly discussed. It is necessary to understand them and optimize electrode structure accordingly to further improve power performance of electrodes. Figure **5.8**(a) shows the measured rate capabilities of 3D C/TiO_2 electrodes with different TiO_2 thicknesses on a 3 nm carbon nano-network. Here, 1C yields 235 mA g^{-1} for 7 nm, 200 mA g^{-1} for 18nm and 140 mA g^{-1} for 27 nm thick TiO_2. During the first 30 cycles, the test current was controlled to increase the charging/discharging rate after every 5 cycles. When the test rates are slow ($\leq$ C/2.5), the 3D C/TiO_2 electrodes with 7 nm and 18 nm TiO_2 show very similar capacities, while the 28 nm TiO_2 electrode shows lower capacities. At low test rates, the thickness of the TiO_2 layers is so low that the Li ions are able to diffuse through the active materials without impacting the rate capability.

However, when the TiO_2 layer is thick enough, Li ion diffusion time through the solid TiO_2 is longer than the time at low test rate, which leads to the decrease of capacity. At higher rates, all three of the samples show considerable capacity loss and larger capacity loss with thicker TiO_2 layers. For example, at a test rate of 10C, the 7 nm TiO_2 sample only delivers a gravimetric capacity of ~117.5 mAh g^{-1}, which is 38% of its capacity at C/10. The thicker the TiO_2 coatings are, the less capacity is retained at high rates.

There are three different mechanisms that cause faster degradation in capacity at high rates: 1) Longer diffusion length and diffusion time of the Li ions in the thicker TiO_2 layer reduce the rate capability. 2) Current collection ability of the 3D carbon network may not be sufficient for the fast Li ion reaction. 3) Starting with the same pore size in the PAA templates, a thicker TiO_2 layer reduces the pore size in the electrode that greatly affects the permeability of Li ions, which ultimately consumes more Li ions and causes faster Li ion depletion.

The transport of electrons is becoming a more and more important factor for high power batteries as the dimension of active materials is reduced to nanometers with the help of nanotechnology [212]. We have compared rate capability of nanosized TiO_2 with different conducting networks in Figure **5.8**(b), along with a few examples of TiO_2 nanostructures from literature, which are mixed with carbon black or graphene for electrical conduction [170, 193, 213]. The data of TiO_2 on 3D Ni nanowire network are cited from our earlier work, where the conductivity of the 3D Ni nanowire network is ~ 10^6 s m^{-1} [178]. Both the TiO_2 without any conducting network and the cited TiO_2, made by mixing carbon black or graphene in conventional ways, show a lower capacity than our 3D C/TiO_2 network. Although the electrical conductivity of the 3D carbon network with 3 nm carbon layer is only ~ 110 s m^{-1}, it is more efficient than the random distributed carbon black or graphene for electron transport.

Furthermore, the rate capability can be improved with further increased conductivity by increasing carbon layer thickness from 3 nm to 8 nm. The rate capability of the Ni/TiO_2 electrode is even higher when the network electrical conductivity is further enhanced by the more conductive metal network. Considering that the metal conducting network would reduce the gravimetric capacity of the electrodes by introducing heavy inactive materials, further improvement of the power performance should be realized by methods such as crystallization of carbon to increase the conductivity of the 3D carbon network.

Large capacity loss still happens at high rates even when the highly conductive 3D Ni network is used, due to the Li ion permeation and depletion resulting from the 3D architecture. To thoroughly exam the effects of the permeation and depletion of the Li ions on rate capability, Figure **5.8**(c) compares the TiO_2 film, the 3D Ni/TiO_2 electrode, and the 3D C/TiO_2 with similar TiO_2 thicknesses. The TiO_2 film is directly coated by ALD on Cu foil as a current collector, the electrons are directly transported to the current collector and the electrolyte has direct access to the TiO_2 without any permeation resistance or depletion problem. At low rates (<1C), the 3D Ni/TiO_2 and the TiO_2 film exhibit similar capacity loss, which demonstrates that the permeation of Li ions in the 3D architecture is sufficient and does not harm the rate capability in this period. The 3D C/TiO_2 with lower electrical conduction shows much worse capacity loss, indicating that the transport of electrons play an important role in the rate capability at low rates. When the test rate is higher than 1C, the capacities of both 3D Ni/TiO_2 and 3D C/TiO_2 drop dramatically, while that of the TiO_2 film drops slightly. Thus, the permeation and depletion of Li ions resulting from the 3D configuration play a much more important role in the capacity loss at high test rates.

5.7 Summary of 3D Carbon Nano-Network

In summary, we have successfully fabricated a 3D carbon nano-network through CVD of carbon on 3D PAA template. The 3D carbon nano-network exhibits a strong ability to enhance the battery performance since its 3D network architecture and numerous gaps can facilitate the transport of Li ions and electrons. As a demonstration, ALD TiO_2 on the 3D carbon nano-network delivered a large areal capacity of ~ 0.37 mAh cm^{-2} due to the large areal mass loading of the 3D C/TiO_2 electrodes. The electrodes also delivered a high gravimetric capacity of ~ 240 mAh g^{-1} based on the whole electrode at the test rate of C/5 and a long cycle life of over 1000 cycles at 1C. The effects of the electrical conductivity of carbon nano-network, ion transport in the active material, and the electrolyte permeability on the rate performance of these 3D C/TiO_2 electrodes are systematically studied. This work provides a significant guide to build 3D electrodes for high performance LIBs.

Bibliography

[1] Tarascon, J. M., and Armand, M., 2001, "Issues and Challenges Facing Rechargeable Lithium Batteries," Nature, 414(6861), pp. 359-367.

[2] Arico, A. S., Bruce, P., Scrosati, B., Tarascon, J. M., and Van Schalkwijk, W., 2005, "Nanostructured Materials for Advanced Energy Conversion and Storage Devices," Nature Materials, 4(5), pp. 366-377.

[3] Guo, Y. G., Hu, J. S., and Wan, L. J., 2008, "Nanostructured Materials for Electrochemical Energy Conversion and Storage Devices," Advanced Materials, 20(15), pp. 2878-2887.

[4] Cheng, F., Tao, Z., Liang, J., and Chen, J., 2008, "Template-Directed Materials for Rechargeable Lithium-Ion Batteries," Chemistry of Materials, 20(3), pp. 667-681.

[5] Megahed, S., and Ebner, W., 1995, "LITHIUM-ION BATTERY FOR ELECTRONIC APPLICATIONS," Journal of Power Sources, 54(1), pp. 155-162.

[6] Prakash, S., Mustain, W. E., and Kohl, P. A., 2009, "Performance of Li-ion secondary batteries in low power, hybrid power supplies," Journal of Power Sources, 189(2), pp. 1184-1189.

[7] Karden, E., Ploumen, S., Fricke, B., Miller, T., and Snyder, K., 2007, "Energy storage devices for future hybrid electric vehicles," Journal of Power Sources, 168(1), pp. 2-11.

[8] Bruce, P. G., Scrosati, B., and Tarascon, J. M., 2008, "Nanomaterials for rechargeable lithium batteries," Angewandte Chemie-International Edition, 47(16), pp. 2930-2946.

[9] Li, N. C., Martin, C. R., and Scrosati, B., 2001, "Nanomaterial-based Li-ion battery electrodes," Journal of Power Sources, 97-8, pp. 240-243.

[10] Sides, C. R., Li, N. C., Patrissi, C. J., Scrosati, B., and Martin, C. R., 2002, "Nanoscale materials for lithium-ion batteries," Mrs Bulletin, 27(8), pp. 604-607.

[11] Zhang, H., Yu, X., and Braun, P., 2011, " Three-Dimensional Bicontinuous Ultrafast-Charge and -Discharge Bulk Battery Electrodes," nature nanotechnology, 6(5), pp. 277-281.

[12] Winter, M., Besenhard, J. O., Spahr, M. E., and Novak, P., 1998, "Insertion electrode materials for rechargeable lithium batteries," Advanced Materials, 10(10), pp. 725-763.

[13] Dahn, J. R., Zheng, T., Liu, Y. H., and Xue, J. S., 1995, "MECHANISMS FOR LITHIUM INSERTION IN CARBONACEOUS MATERIALS," Science, 270(5236), pp. 590-593.

[14] Armstrong, A. R., Armstrong, G., Canales, J., and Bruce, P. G., 2005, "TiO_2-B Nanowires as Negative Electrodes for Rechargeable Lithium Batteries," Journal of Power Sources, 146(1-2), pp. 501-506.

[15] Li, Y. G., Tan, B., and Wu, Y. Y., 2006, "Freestanding Mesoporous Quasi-Single-Crystalline Co_3O_4 Nanowire Arrays," Journal of the American Chemical Society, 128(44), pp. 14258-14259.

[16] Chan, C. K., Zhang, X. F., and Cui, Y., 2008, "High capacity Li ion battery anodes using Ge nanowires," Nano Letters, 8(1), pp. 307-309.

[17] Cui, Y., 2008, "High-performance lithium battery anodes using silicon nanowires," Nat. Nanotech., 3, p. 31.

[18] Li, Y. G., Tan, B., and Wu, Y. Y., 2008, "Mesoporous CO_3O_4 Nanowire Arrays for Lithium Ion Batteries with High Capacity and Rate Capability," Nano Letters, 8(1), pp. 265-270.

[19] Armstrong, A. R., Armstrong, G., Canales, J., Garcia, R., and Bruce, P. G., 2005, "Lithium-Ion Intercalation into TiO_2-B Nanowires," Advanced Materials, 17(7), pp. 862-865.

[20] Tabernal, P. L., and Mitra, S., 2006, "High rate capabilities Fe3O4-based Cu nano-architectured electrodes for lithium-ion battery applications," Nature materials, 5, p. 567.

[21] Park, M. S., Wang, G. X., Kang, Y. M., Wexler, D., Dou, S. X., and Liu, H. K., 2007, "Preparation and electrochemical properties of SnO2 nanowires for application in lithium-ion batteries," Angewandte Chemie-International Edition, 46(5), pp. 750-753.

[22] Nam, K. T., Kim, D. W., Yoo, P. J., Chiang, C. Y., Meethong, N., Hammond, P. T., Chiang, Y. M., and Belcher, A. M., 2006, "Virus-enabled synthesis and assembly of nanowires for lithium ion battery electrodes," Science, 312(5775), pp. 885-888.

[23] Chan, C. K., Peng, H. L., Twesten, R. D., Jarausch, K., Zhang, X. F., and Cui, Y., 2007, "Fast, completely reversible Li insertion in vanadium pentoxide nanoribbons," Nano Letters, 7(2), pp. 490-495.

[24] Lee, S. W., Yabuuchi, N., Gallant, B. M., Chen, S., Kim, B. S., Hammond, P. T., and Shao-Horn, Y., 2010, "High-Power Lithium Batteries From Functionalized Carbon-Nanotube Electrodes," Nature Nanotechnology, 5(7), pp. 531-537.

[25] Maranchi, J. P., Hepp, A. F., Evans, A. G., Nuhfer, N. T., and Kumta, P. N., 2006, "Interfacial properties of the a-Si/Cu : active-inactive thin-film anode system for lithium-ion batteries," Journal of the Electrochemical Society, 153(6), pp. A1246-A1253.

[26] Beaulieu, L. Y., Eberman, K. W., Turner, R. L., Krause, L. J., and Dahn, J. R., 2001, "Colossal reversible volume changes in lithium alloys," Electrochemical and Solid State Letters, 4(9), pp. A137-A140.

[27] Kim, B. M., Cho, G. B., Noh, J. P., Ahn, H. J., Choi, E. S., Miyazaki, S., and Nam, T. H., 2010, "Mechanical stability of Si thin film deposited on a Ti-50.3Ni(at%) alloy," Journal of Alloys and Compounds, 497(1-2), pp. L13-L16.

[28] Zhang, T., Zhang, H. P., Yang, L. C., Wang, B., Wu, Y. P., and Takamur, T., 2008, "The structural evolution and lithiation behavior of vacuum-deposited Si film with high reversible capacity," Electrochimica Acta, 53(18), pp. 5660-5664.

[29] Uehara, M., Suzuki, J., Tamura, K., Sekine, K., and Takamura, T., 2005, "Thick vacuum deposited silicon films suitable for the anode of Li-ion battery," Journal of Power Sources, 146(1-2), pp. 441-444.

[30] Wang, W., and Kumta, P. N., 2010, "Nanostructured Hybrid Silicon/Carbon Nanotube Heterostructures: Reversible High-Capacity Lithium-Ion Anodes," Acs Nano, 4(4), pp. 2233-2241.

[31] Shin, H. C., and Liu, M. L., 2005, "Three-dimensional porous copper-tin alloy electrodes for rechargeable lithium batteries," Advanced Functional Materials, 15(4), pp. 582-586.

[32] Kim, H., Han, B., Choo, J., and Cho, J., 2008, "Three-Dimensional Porous Silicon Particles for Use in High-Performance Lithium Secondary Batteries," Angewandte Chemie International Edition, 47(52), pp. 10151-10154.

[33] Yao, M., Okuno, K., Iwaki, T., Awazu, T., and Sakai, T., 2010, "Long cycle-life LiFePO4/Cu-Sn lithium ion battery using foam-type three-dimensional current collector," Journal of Power Sources, 195(7), pp. 2077-2081.

[34] Yao, M., Okuno, K., Iwaki, T., Kato, M., Tanase, S., Emura, K., and Sakai, T., 2007, "LiFePO4-based electrode using micro-porous current collector for high power lithium ion battery," Journal of Power Sources, 173(1), pp. 545-549.

[35] Yoshio, M., Tsumura, T., and Dimov, N., 2005, "Electrochemical behaviors of silicon based anode material," Journal of Power Sources, 146(1–2), pp. 10-14.

[36] Ergang, N. S., Lytle, J. C., Lee, K. T., Oh, S. M., Smyrl, W. H., and Stein, A., 2006, "Photonic Crystal Structures as a Basis for a Three-Dimensionally Interpenetrating Electrochemical-Cell System," Advanced Materials (Weinheim, Germany), 18(13), pp. 1750-1753.

[37] Wang, Z., Fierke, M. A., and Stein, A., 2008, "Porous Carbon/Tin (IV) Oxide Monoliths as Anodes for Lithium-Ion Batteries," Journal of the Electrochemical Society, 155(9), pp. A658-A663.

[38] Sakamoto, J. S., and Dunn, B., 2002, "Hierarchical Battery Electrodes Based on Inverted Opal Structures," Journal of Materials Chemistry, 12(10), pp. 2859-2861.

[39] Rolison, D. R., Long, J. W., Lytle, J. C., Fischer, A. E., Rhodes, C. P., McEvoy, T. M., Bourg, M. E., and Lubers, A. M., 2009, "Multifunctional 3D nanoarchitectures for energy storage and conversion," Chemical Society Reviews, 38(1), p. 226.

[40] Long, J. W., Dunn, B., Rolison, D. R., and White, H. S., 2004, "Three-dimensional battery architectures," Chemical Reviews, 104(10), pp. 4463-4492.

[41] Choi, J. W., Hu, L. B., Cui, L. F., McDonough, J. R., and Cui, Y., 2010, "Metal current collector-free freestanding silicon-carbon 1D nanocomposites for ultralight anodes in lithium ion batteries," Journal of Power Sources, 195(24), pp. 8311-8316.

[42] Mecklenburg, M., Schuchardt, A., Mishra, Y. K., Kaps, S., Adelung, R., Lotnyk, A., Kienle, L., and Schulte, K., 2012, "Aerographite: Ultra Lightweight, Flexible Nanowall, Carbon Microtube Material with Outstanding Mechanical Performance," Advanced Materials (Weinheim, Germany), 24(26), pp. 3486-3490.

[43] Baughman, R. H., Zakhidov, A. A., and de Heer, W. A., 2002, "Carbon Nanotubes--the Route Toward Applications," Science, 297(5582), pp. 787-792.

[44] Moskon, J., Dominko, R., Gaberscek, M., Cerc-Korosec, R., and Jamnik, J., 2006, "Citrate-derived carbon nanocoatings for poorly conducting cathode - A detailed study using TiO2 substrate materials," Journal of the Electrochemical Society, 153(10), pp. A1805-A1811.

[45] Magasinski, A., Dixon, P., Hertzberg, B., Kvit, A., Ayala, J., and Yushin, G., 2010, "High-performance lithium-ion anodes using a hierarchical bottom-up approach," Nature Materials, 9(4), pp. 353-358.

[46] Wang, C. S., Wu, G. T., Zhang, X. B., Qi, Z. F., and Li, W. Z., 1998, "Lithium Insertion in Carbon ‐ Silicon Composite Materials Produced by Mechanical Milling," Journal of the Electrochemical Society, 145(8), pp. 2751-2758.

[47] Inagaki, M., 2009, "Pores in carbon materials-importance of their control," New Carbon Materials, 24(3), pp. 193-232.

[48] Calvo, E. G., Ania, C. O., Zubizarreta, L., Menéndez, J. A., and Arenillas, A., 2010, "Exploring New Routes in the Synthesis of Carbon Xerogels for Their Application in Electric Double-Layer Capacitors†," Energy & Fuels, 24(6), pp. 3334-3339.

[49] Kistler, S. S., 1931, "Coherent expanded aerogels and jellies," Nature, 127, pp. 741-741.

[50] Lytle, J. C., Wallace, J. M., Sassin, M. B., Barrow, A. J., Long, J. W., Dysart, J. L., Renninger, C. H., Saunders, M. P., Brandell, N. L., and Rolison, D. R., 2011, "The right kind of interior for multifunctional electrode architectures: carbon nanofoam papers with aperiodic submicrometre pore networks interconnected in 3D," Energy & Environmental Science, 4(5), pp. 1913-1925.

[51] Zhu, Y., Hu, H., Li, W.-C., and Zhang, X., 2006, "Cresol–formaldehyde based carbon aerogel as electrode material for electrochemical capacitor," Journal of Power Sources, 162(1), pp. 738-742.

[52] Liu, N., Shen, J., and Liu, D., 2013, "A Fe2O3 nanoparticle/carbon aerogel composite for use as an anode material for lithium ion batteries," Electrochimica Acta, 97(0), pp. 271-277.

[53] Piao, Y., Kim, H. S., Sung, Y.-E., and Hyeon, T., 2010, "Facile scalable synthesis of magnetite nanocrystals embedded in carbon matrix as superior anode materials for lithium-ion batteries," Chemical Communications (Cambridge, United Kingdom), 46(1), pp. 118-120.

[54] Yang, X., Fan, K., Zhu, Y., Shen, J., Jiang, X., Zhao, P., and Li, C., 2012, "Tailored graphene-encapsulated mesoporous Co3O4 composite microspheres for high-performance lithium ion batteries," Journal of Materials Chemistry, 22(33), pp. 17278-17283.

[55] Dimesso, L., Spanheimer, C., Jacke, S., and Jaegermann, W., 2011, "Synthesis and characterization of three-dimensional carbon foams–LiFePO4 composites," Journal of Power Sources, 196(16), pp. 6729-6734.

[56] Johns, P., Roberts, M., and Owen, J., 2011, "Conformal electrodeposition of manganese dioxide onto reticulated vitreous carbon for 3D microbattery applications," Journal of Materials Chemistry, 21(27), pp. 10153-10159.

[57] Doherty, C. M., Caruso, R. A., Smarsly, B. M., Adelhelm, P., and Drummond, C. J., 2009, "Hierarchically Porous Monolithic LiFePO4/Carbon Composite Electrode Materials for High Power Lithium Ion Batteries," Chemistry of Materials, 21(21), pp. 5300-5306.

[58] Ji, H., Zhang, L., Pettes, M. T., Li, H., Chen, S., Shi, L., Piner, R., and Ruoff, R. S., 2012, "Ultrathin Graphite Foam: A Three-Dimensional Conductive Network for Battery Electrodes," Nano Letters, 12(5), pp. 2446-2451.

[59] Ding, B., Yuan, C., Shen, L., Xu, G., Nie, P., and Zhang, X., 2013, "Encapsulating Sulfur into Hierarchically Ordered Porous Carbon as a High-Performance Cathode for Lithium–Sulfur Batteries," Chemistry – A European Journal, 19(3), pp. 1013-1019.

[60] Huang, X., Chen, J., Lu, Z., Yu, H., Yan, Q., and Hng, H. H., 2013, "Carbon inverse opal entrapped with electrode active nanoparticles as high-performance anode for lithium-ion batteries," Scientific Reports, 3.

[61] Winter, M., Besenhard, J. O., Spahr, M. E., and Novak, P., 1998, "Insertion electrode materials for rechargeable lithium batteries," Advanced Materials (Weinheim, Germany), 10(10), pp. 725-763.

[62] Dresselhaus, S., and Division, N. A. T. O. S. A., 1986, Intercalation in layered materials, Plenum Press.

[63] Kinoshita, K., 1988, Carbon: electrochemical and physicochemical properties.

[64] Che, G. L., Lakshmi, B. B., Martin, C. R., and Fisher, E. R., 1999, "Metal-nanocluster-filled carbon nanotubes: Catalytic properties and possible applications in electrochemical energy storage and production," Langmuir, 15(3), pp. 750-758.

[65] Yoo, E., Kim, J., Hosono, E., Zhou, H., Kudo, T., and Honma, I., 2008, "Large reversible Li storage of graphene nanosheet families for use in rechargeable lithium ion batteries," Nano Letters, 8(8), pp. 2277-2282.

[66] Wu, Y. P., Rahm, E., and Holze, R., 2003, "Carbon anode materials for lithium ion batteries," Journal of Power Sources, 114(2), pp. 228-236.

[67] Claye, A. S., Fischer, J. E., Huffman, C. B., Rinzler, A. G., and Smalley, R. E., 2000, "Solid-State Electrochemistry of the Li Single Wall Carbon Nanotube System," Journal of the Electrochemical Society, 147(8), pp. 2845-2852.

[68] Barisci, J. N., Wallace, G. G., and Baughman, R. H., 2000, "Electrochemical quartz crystal microbalance studies of single-wall carbon nanotubes in aqueous and non-aqueous solutions," Electrochimica Acta, 46(4), pp. 509-517.

[69] Zhao, J., Buldum, A., Han, J., and Ping Lu, J., 2000, "First-Principles Study of Li-Intercalated Carbon Nanotube Ropes," Physical Review Letters, 85(8), pp. 1706-1709.

[70] Reddy, A. L. M., Shaijumon, M. M., Gowda, S. R., and Ajayan, P. M., 2009, "Coaxial MnO_2/Carbon Nanotube Array Electrodes for High-Performance Lithium Batteries," Nano Letters, 9(3), pp. 1002-1006.

[71] Ban, C., Wu, Z., Gillaspie, D. T., Chen, L., Yan, Y., Blackburn, J. L., and Dillon, A. C., 2010, "Nanostructured Fe3O4/SWNT Electrode: Binder-Free and High-Rate Li-Ion Anode," Advanced Materials (Weinheim, Germany), 22(20), pp. E145-E149.

[72] Yin, S., Zhang, Y., Kong, J., Zou, C., Li, C. M., Lu, X., Ma, J., Boey, F. Y. C., and Chen, X., 2011, "Assembly of Graphene Sheets into Hierarchical Structures for High-Performance Energy Storage," ACS Nano, 5(5), pp. 3831-3838.

[73] Kasavajjula, U., Wang, C. S., and Appleby, A. J., 2007, "Nano- and bulk-silicon-based insertion anodes for lithium-ion secondary cells," Journal of Power Sources, 163(2), pp. 1003-1039.

[74] Guo, Z. P., Wang, J. Z., Liu, H. K., and Dou, S. X., 2005, "Study of silicon/polypyrrole composite as anode materials for Li-ion batteries," Journal of Power Sources, 146(1-2), pp. 448-451.

[75] Liu, W. R., Guo, Z. Z., Young, W. S., Shieh, D. T., Wu, H. C., Yang, M. H., and Wu, N. L., 2005, "Effect of electrode structure on performance of Si anode in Li-ion batteries: Si particle size and conductive additive," Journal of Power Sources, 140(1), pp. 139-144.

[76] Kim, I., Kumta, P. N., and Blomgren, G. E., 2000, "Si/TiN nanocomposites - Novel anode materials for Li-ion batteries," Electrochemical and Solid State Letters, 3(11), pp. 493-496.

[77] Kim, I., Blomgren, G. E., and Kumta, P. N., 2003, "Nanostructured Si/TiB2 composite anodes for Li-ion batteries," Electrochemical and Solid State Letters, 6(8), pp. A157-A161.

[78] Kim, I. S., Blomgren, G. E., and Kumta, P. N., 2004, "Si-SiC nanocomposite anodes synthesized using high-energy mechanical milling," Journal of Power Sources, 130(1-2), pp. 275-280.

[79] Patel, P., Kim, I. S., and Kumta, P. N., 2005, "Nanocomposites of silicon/titanium carbide synthesized using high-energy mechanical milling for use as anodes in lithium-ion batteries," Materials Science and Engineering B-Solid State Materials for Advanced Technology, 116(3), pp. 347-352.

[80] Chan, C. K., Peng, H. L., Liu, G., McIlwrath, K., Zhang, X. F., Huggins, R. A., and Cui, Y., 2008, "High-performance lithium battery anodes using silicon nanowires," Nature Nanotechnology, 3(1), pp. 31-35.

[81] Kim, H., Choi, J., Sohn, H. J., and Kang, T., 1999, "The insertion mechanism of lithium into Mg2Si anode material for Li-ion batteries," Journal of the Electrochemical Society, 146(12), pp. 4401-4405.

[82] Weydanz, W. J., Wohlfahrt-Mehrens, M., and Huggins, R. A., 1999, "A room temperature study of the binary lithium–silicon and the ternary lithium–chromium–silicon system for use in rechargeable lithium batteries," Journal of Power Sources, 81–82(0), pp. 237-242.

[83] Hwang, S. M., Lee, H. Y., Jang, S. W., Lee, S. M., Lee, S. J., Baik, H. K., and Lee, J. Y., 2001, "Lithium Insertion in SiAg Powders Produced by Mechanical Alloying," Electrochemcal and Solid-State Letters, 4(7), p. 4.

[84] Kim, I. S., and Kumta, P. N., 2004, "High capacity Si/C nanocomposite anodes for Li-ion batteries," Journal of Power Sources, 136(1), pp. 145-149.

[85] Idota, Y., Kubota, T., Matsufuji, A., Maekawa, Y., and Miyasaka, T., 1997, "Tin-based amorphous oxide: A high-capacity lithium-ion-storage material," Science, 276(5317), pp. 1395-1397.

[86] Poizot, P., Laruelle, S., Grugeon, S., Dupont, L., and Tarascon, J. M., 2000, "Nano-sized transition-metaloxides as negative-electrode materials for lithium-ion batteries," Nature, 407(6803), pp. 496-499.

[87] Winter, M., and Besenhard, J. O., 1999, "Electrochemical lithiation of tin and tin-based intermetallics and composites," Electrochimica Acta, 45(1-2), pp. 31-50.

[88] Li, N. C., and Martin, C. R., 2001, "A high-rate, high-capacity, nanostructured Sn-based anode prepared using sol-gel template synthesis," Journal of the Electrochemical Society, 148(2), pp. A164-A170.

[89] Martin, C. R., Nishizawa, M., Jirage, K., and Kang, M., 2001, "Investigations of the transport properties of gold nanotubule membranes," Journal of Physical Chemistry B, 105(10), pp. 1925-1934.

[90] Wang, Y., Lee, J. Y., and Zeng, H. C., 2005, "Polycrystalline SnO2 nanotubes prepared via infiltration casting of nanocrystallites and their electrochemical application," Chemistry of Materials, 17(15), pp. 3899-3903.

[91] Wang, Y., Zeng, H. C., and Lee, J. Y., 2006, "Highly reversible lithium storage in porous SnO2 nanotubes with coaxially grown carbon nanotube overlayers," Advanced Materials, 18(5), pp. 645-+.

[92] Liu, S., Li, Q., Chen, Y. X., and Zhang, F. J., 2009, "Carbon-coated copper-tin alloy anode material for lithium ion batteries," Journal of Alloys and Compounds, 478(1-2), pp. 694-698.

[93] Guo, H., Zhao, S., Zhao, H. L., and Chen, Y. S., 2009, "Synthesis and electrochemical performance of novel loose structured submicro/micro-sized NiSnx alloy composites for lithium batteries," Electrochimica Acta, 54(16), pp. 4040-4044.

[94] Dong, Q. F., Wu, C. Z., Jin, M. G., Huang, Z. C., Zheng, M. S., You, J. K., and Lin, Z. G., 2004, "Preparation and performance of nickel-tin alloys used as anodes for lithium-ion battery," Solid State Ionics, 167(1-2), pp. 49-54.

[95] Wang, F., Zhao, M. S., and Song, X. P., 2009, "The improved electrochemical performance of SnSb-based alloy anode materials for Li-ion batteries," Journal of Alloys and Compounds, 472(1-2), pp. 55-58.

[96] Hassoun, J., Panero, S., Simon, P., Taberna, P. L., and Scrosati, B., 2007, "High-Rate, Long-Life Ni–Sn Nanostructured Electrodes for Lithium-Ion Batteries," Advanced Materials, 19(12), pp. 1632-1635.

[97] Kotobuki, M., Okada, N., and Kanamura, K., 2011, "Design of a micro-pattern structure for a three dimensionally macroporous Sn-Ni alloy anode with high areal capacity," Chemical Communications (Cambridge, United Kingdom), 47(21), pp. 6144-6146.

[98] Tabuchi, T., Hochgatterer, N., Ogumi, Z., and Winter, M., 2009, "Ternary Sn-Sb-Co alloy film as new negative electrode for lithium-ion cells," Journal of Power Sources, 188(2), pp. 552-557.

[99] Taberna, L., Mitra, S., Poizot, P., Simon, P., and Tarascon, J. M., 2006, "High rate capabilities Fe3O4-based Cu nano-architectured electrodes for lithium-ion battery applications," Nature Materials, 5(7), pp. 567-573.

[100] Chen, J., Xu, L. N., Li, W. Y., and Gou, X. L., 2005, "alpha-Fe2O3 nanotubes in gas sensor and lithium-ion battery applications," Advanced Materials, 17(5), pp. 582-+.

[101] Bavykin, D. V., Friedrich, J. M., and Walsh, F. C., 2006, "Protonated titanates and TiO2 nanostructured materials: Synthesis, properties, and applications," Advanced Materials, 18(21), pp. 2807-2824.

[102] Armstrong, A. R., Armstrong, G., Canales, J., and Bruce, P. G., 2004, "TiO2-B nanowires," Angewandte Chemie-International Edition, 43(17), pp. 2286-2288.

[103] Armstrong, G., Armstrong, A. R., Canales, J., and Bruce, P. G., 2005, "Nanotubes with the TiO2-B structure," Chemical Communications(19), pp. 2454-2456.

[104] Ortiz, G. F., Hanzu, I., Lavela, P., Knauth, P., Tirado, J. L., and Djenizian, T., 2010, "Nanoarchitectured TiO2/SnO: A Future Negative Electrode for High Power Density Li-Ion Microbatteries?," Chemistry of Materials, 22(5), pp. 1926-1932.

[105] Nguyen, C. C., and Song, S.-W., 2010, "Interfacial structural stabilization on amorphous silicon anode for improved cycling performance in lithium-ion batteries," Electrochimica Acta, 55(8), pp. 3026-3033.

[106] Takamura, T., Uehara, M., Suzuki, J., Sekine, K., and Tamura, K., 2006, "High capacity and long cycle life silicon anode for Li-ion battery," Journal of Power Sources, 158(2), pp. 1401-1404.

[107] Kim, Y.-L., Sun, Y.-K., and Lee, S.-M., 2008, "Enhanced electrochemical performance of silicon-based anode material by using current collector with modified surface morphology," Electrochimica Acta, 53(13), pp. 4500-4504.

[108] Maranchi, J. P., Hepp, A. F., Evans, A. G., Nuhfer, N. T., and Kumta, P. N., 2006, "Interfacial Properties of the a-Si / Cu:Active – Inactive Thin-Film Anode System for Lithium-Ion Batteries," Journal of The Electrochemical Society, 153(6), p. A1246.

[109] Yin, J., Wada, M., Yamamoto, K., Kitano, Y., Tanase, S., and Sakai, T., 2006, "Micrometer-Scale Amorphous Si Thin-Film Electrodes Fabricated by Electron-Beam Deposition for Li-Ion Batteries," Journal of the Electrochemical Society, 153(3), pp. A472-A477.

[110] Guo, J., and Wang, C., 2010, "A polymer scaffold binder structure for high capacity silicon anode of lithium-ion battery," Chemical Communications (Cambridge, United Kingdom), 46(9), pp. 1428-1430.

[111] Zhang, Y., Zhang, X. G., Zhang, H. L., Zhao, Z. G., Li, F., Liu, C., and Cheng, H. M., 2006, "Composite anode material of silicon/graphite/carbon nanotubes for Li-ion batteries," Electrochimica Acta, 51(23), pp. 4994-5000.

[112] Dimov, N., Kugino, S., and Yoshio, M., 2004, "Mixed silicon–graphite composites as anode material for lithium ion batteries: Influence of preparation conditions on the properties of the material," Journal of Power Sources, 136(1), pp. 108-114.

[113] Lee, H.-Y., and Lee, S.-M., 2004, "Carbon-coated nano-Si dispersed oxides/graphite composites as anode material for lithium ion batteries," Electrochemistry Communications, 6(5), pp. 465-469.

[114] Bhuvaneswari, M. S., Bramnik, N. N., Ensling, D., Ehrenberg, H., and Jaegermann, W., 2008, "Synthesis and characterization of Carbon Nano Fiber/LiFePO(4) composites for Li-ion batteries," Journal of Power Sources, 180(1), pp. 553-560.

[115] Cui, L. F., Hu, L. B., Choi, J. W., and Cui, Y., 2010, "Light-Weight Free-Standing Carbon Nanotube-Silicon Films for Anodes of Lithium Ion Batteries," ACS Nano, 4(7), pp. 3671-3678.

[116] Kasavajjula, U., Wang, C., and Appleby, A., 2007, "Nano- and bulk-silicon-based insertion anodes for lithium-ion secondary cells," Journal of Power Sources, 163(2), pp. 1003-1039.

[117] Fischer, A. E., Pettigrew, K. A., Rolison, D. R., Stroud, R. M., and Long, J. W., 2007, "Incorporation of Homogeneous, Nanoscale MnO2 within Ultraporous Carbon Structures via Self-Limiting Electroless Deposition: Implications for Electrochemical Capacitors," Nano Letters, 7(2), pp. 281-286.

[118] Tian, M., Wang, W., Lee, S. H., Lee, Y. C., and Yang, R. G., 2011, "Enhancing Ni-Sn Nanowire Lithium-Ion Anode Performance by Tailoring Active/Inactive Material Interfaces," Journal of Power Sources, 196(23), pp. 10207-10212.

[119] Wang, W., Tian, M., Abdulagatov, A., George, S. M., Lee, Y.-C., and Yang, R., 2011, "Three-Dimensional Ni/TiO2 Nanowire Network for High Areal Capacity Lithium Ion Microbattery Applications," Nano Lett., 12(2), pp. 655-660.

[120] Taberna, P. L., Mitra, S., Poizot, P., Simon, P., and Tarascon, J. M., 2006, "High Rate Capabilities Fe_3O_4-Based Cu Nano-Architectured Electrodes for Lithium-Ion Battery Applications," Nature Materials, 5(7), pp. 567-573.

[121] Nielsch, K., Muller, F., Li, A. P., and Gosele, U., 2000, "Uniform nickel deposition into ordered alumina pores by pulsed electrodeposition," Advanced Materials (Weinheim, Germany), 12(8), pp. 582-586.

[122] Sauer, G., Brehm, G., Schneider, S., Nielsch, K., Wehrspohn, R. B., Choi, J., Hofmeister, H., and Gösele, U., 2002, "Highly ordered monocrystalline silver nanowire arrays," Journal of Applied Physics, 91(5), p. 3243.

[123] Karmhag, R., Tesfamichael, T., Wäckelgård, E., Niklasson, G. A., and Nygren, M., 2000, "Oxidation Kinetics of Nickel Particles: Comparison Between Free Particles and Particles in an Oxide Matrix," Solar Energy, 68(4), pp. 329-333.

[124] Che, G., Lakshmi, B. B., Fisher, E. R., and Martin, C. R., 1998, "Carbon nanotubule membranes for electrochemical energy storage and production," Nature, 393(6683), pp. 346-349.

[125] Liu, R., Duay, J., and Lee, S. B., 2011, "Electrochemical Formation Mechanism for the Controlled Synthesis of Heterogeneous MnO2/Poly(3,4-ethylenedioxythiophene) Nanowires," ACS Nano, 5(7), pp. 5608-5619.

[126] Masuda, H., Yamada, H., Satoh, M., Asoh, H., Nakao, M., and Tamamura, T., 1997, "Highly Ordered Nanochannel-Array Architecture in Anodic Alumina," Applied Physics Letters, 71(19), pp. 2770-2772.

[127] Lee, W., Ji, R., Gosele, U., and Nielsch, K., 2006, "Fast fabrication of long-range ordered porous alumina membranes by hard anodization," Nature Materials, 5(9), pp. 741-747.

[128] Molchan, I. S., Molchan, T. V., Gaponenko, N. V., Skeldon, P., and Thompson, G. E., 2010, "Impurity-Driven Defect Generation in Porous Anodic Alumina," Electrochemistry Communications, 12(5), pp. 693-696.

[129] Lo, D., and Budiman, R. A., 2007, "Fabrication and Characterization of Porous Anodic Alumina Films from Impure Aluminum Foils," Journal of The Electrochemical Society, 154(1), p. C60.

[130] Chen, C. C., Chen, J. H., and Chao, C. G., 2005, "Post-treatment Method of Producing Ordered Array of Anodic Aluminum Oxide Using General Purity Commercial (99.7%) Aluminum," Japanese Journal of Applied Physics, 44(No. 3), pp. 1529-1533.

[131] Chung, C. K., Zhou, R. X., Liu, T. Y., and Chang, W. T., 2009, "Hybrid pulse anodization for the fabrication of porous anodic alumina films from commercial purity (99%) aluminum at room temperature," Nanotechnology, 20(5), p. 055301.

[132] Endo, M., Kim, C., Nishimura, K., Fujino, T., and Miyashita, K., 2000, "Recent development of carbon materials for Li ion batteries," Carbon, 38(2), pp. 183-197.

[133] Yang, J., Winter, M., and Besenhard, J. O., 1996, "Small particle size multiphase Li-alloy anodes for lithium-ion-batteries," Solid State Ionics, 90(1-4), pp. 281-287.

[134] Mao, O., Turner, R. L., Courtney, I. A., Fredericksen, B. D., Buckett, M. I., Krause, L. J., and Dahn, J. R., 1999, "Active/inactive nanocomposites as anodes for Li-ion batteries," Electrochemical and Solid State Letters, 2(1), pp. 3-5.

[135] Tirado, J. L., 2003, "Inorganic materials for the negative electrode of lithium-ion batteries: state-of-the-art and future prospects," Materials Science & Engineering R-Reports, 40(3), pp. 103-136.

[136] Kepler, K. D., Vaughey, J. T., and Thackeray, M. M., 1999, "LixCu6Sn5 ($0 < x < 13$): An intermetallic insertion electrode for rechargeable lithium batteries," Electrochemical and Solid State Letters, 2(7), pp. 307-309.

[137] Xia, Y. Y., Sakai, T., Fujieda, T., Wada, M., and Yoshinaga, H., 2001, "Flake Cu-Sn alloys as negative electrode materials for rechargeable lithium batteries," Journal of the Electrochemical Society, 148(5), pp. A471-A481.

[138] Qin, H. Y., Zhao, X. B., Jiang, N. P., and Li, Z. P., 2007, "Solvothermal synthesis and ex situ XRD study of nano-Ni3Sn2 used as an anode material for lithium-ion batteries," Journal of Power Sources, 171(2), pp. 948-952.

[139] Amadei, I., Panero, S., Scrosati, B., Cocco, G., and Schiffini, L., 2005, "The Ni3Sn4 intermetallic as a novel electrode in lithium cells," Journal of Power Sources, 143(1-2), pp. 227-230.

[140] Woo, S. W., Okada, N., Kotobuki, M., Sasajima, K., Munakata, H., Kajihara, K., and Kanamura, K., 2010, "Highly patterned cylindrical Ni-Sn alloys with 3-dimensionally ordered macroporous structure as anodes for lithium batteries," Electrochimica Acta, 55(27), pp. 8030-8035.

[141] Hassoun, J., Panero, S., Simon, P., Taberna, P. L., and Scrosati, B., 2007, "High-rate, long-life Ni-Sn nanostructured electrodes for lithium-ion batteries," Advanced Materials, 19(12), pp. 1632-+.

[142] Sapp, S. A., Lakshmi, B. B., and Martin, C. R., 1999, "Template Synthesis of Bismuth Telluride Nanowires," Advanced Materials (Weinheim, Germany), 11(5), pp. 402-404.

[143] Bund, A., and Thiemig, D., 2007, "Influence of Bath Composition and pH on the Electrocodeposition of Alumina Nanoparticles and Copper," Journal of Applied Electrochemistry, 37(3), pp. 345-351.

[144] Mukaibo, H., Sumi, T., Yokoshima, T., Momma, T., and Osaka, T., 2003, "Electrodeposited Sn-Ni alloy film as a high capacity anode material for lithium-ion secondary batteries," Electrochemical and Solid State Letters, 6(10), pp. A218-A220.

[145] Hassoun, J., Panero, S., and Scrosati, B., 2006, "Electrodeposited Ni-Sn intermetallic electrodes for advanced lithium ion batteries," Journal of Power Sources, 160(2), pp. 1336-1341.

[146] Zhang, J. J., and Xia, Y. Y., 2006, "Co-Sn alloys as negative electrode materials for rechargeable lithium batteries," Journal of the Electrochemical Society, 153(8), pp. A1466-A1471.

[147] Mukaibo, H., Momma, T., Mohamedi, M., and Osaka, T., 2005, "Structural and Morphological Moditications of a Nanosized 62 Atom Percent Sn-Ni Thin Film Anode During Reaction with Lithium," Journal of the Electrochemical Society, 152(3), pp. A560-A565.

[148] Deshpande, R., Cheng, Y. T., and Verbrugge, M. W., 2010, "Modeling diffusion-induced stress in nanowire electrode structures," J. Power Sources, 195(15), pp. 5081-5088.

[149] Chan, C. K., Patel, R. N., O'Connell, M. J., Korgel, B. A., and Cui, Y., 2010, "Solution-Grown Silicon Nanowires for Lithium-Ion Battery Anodes," ACS Nano, 4(3), pp. 1443-1450.

[150] Ferrara, G., Damen, L., Arbizzani, C., Inguanta, R., Piazza, S., Sunseri, C., and Mastragostino, M., 2011, "SnCo Nanowire Array as Negative Electrode for Lithium-Ion Batteries," Journal of Power Sources, 196(3), pp. 1469-1473.

[151] Ghassemi, H., Au, M., Chen, N., Heiden, P. A., and Yassar, R. S., 2011, "In Situ Electrochemical Lithiation/Delithiation Observation of Individual Amorphous Si Nanorods," ACS Nano, 5(10), pp. 7805-7811.

[152] Teki, R., Datta, M. K., Krishnan, R., Parker, T. C., Lu, T.-M., Kumta, P. N., and Koratkar, N., 2009, "Nanostructured Silicon Anodes for Lithium Ion Rechargeable Batteries," Small, 5(20), pp. 2236-2242.

[153] Cui, L.-F., Ruffo, R., Chan, C. K., Peng, H., and Cui, Y., 2008, "Crystalline-Amorphous Core−Shell Silicon Nanowires for High Capacity and High Current Battery Electrodes," Nano Letters, 9(1), pp. 491-495.

[154] Wu, X. D., Li, H., Chen, L. Q., and Huang, X. J., 2002, "Agglomeration and the Surface Passivating Film of Ag Nano-Brush Electrode in Lithium Batteries," Solid State Ionics, 149(3-4), pp. 185-192.

[155] Kim, J., Khanal, S., Islam, M., Khatri, A., and Choi, D., 2008, "Electrochemical Characterization of Vertical Arrays of Tin Nanowires Grown on Silicon Substrates as Anode Materials for Lithium Rechargeable Microbatteries," Electrochemistry Communications, 10(11), pp. 1688-1690.

[156] Bruce, P. G., Scrosati, B., and Tarascon, J.-M., 2008, "Nanomaterials for Rechargeable Lithium Batteries," Angewandte Chemie International Edition, 47(16), pp. 2930-2946.

[157] Sander, M. S., Prieto, A. L., Gronsky, R., Sands, T., and Stacy, A. M., 2002, "Fabrication of High-Density, High Aspect Ratio, Large-Area Bismuth Telluride Nanowire Arrays by Electrodeposition into Porous Anodic Alumina Templates," Advanced Materials (Weinheim, Germany), 14(9), pp. 665-667.

[158] Zhao, S., Chan, K., Yelon, A., and Veres, T., 2007, "Preparation of Open-Through Anodized Aluminium Oxide Films with a Clean Method," Nanotechnology, 18(24), p. 245304.

[159] Masuda, H., and Fukuda, K., 1995, "Ordered Metal Nanohole Arrays Made by A 2-Step Replication of Honeycomb Structures of Anodic Alumina," Science, 268(5216), pp. 1466-1468.

[160] Luo, B., Yang, D. C., Liang, M. H., and Zhi, L. J., 2010, "Large-Scale Fabrication of Single Crystalline Tin Nanowire Arrays," Nanoscale, 2(9), pp. 1661-1664.

[161] Hassoun, J., Panero, S., and Scrosati, B., 2006, "Electrodeposited Ni–Sn Intermetallic Electrodes for Advanced Lithium Ion Batteries," Journal of Power Sources, 160(2), pp. 1336-1341.

[162] Zhang, W., Clauss, M., and Schwager, F., 2011, "Growth Behavior of Meta-Stable NiSn(3) Intermetallic Compound and Its Potential Influence on the Reliability of Electronic Components," Ieee Transactions on Components Packaging and Manufacturing Technology, 1(8), pp. 1259-1268.

[163] 2008, "Abaqus Analysis User's Manual," Simulia Co.

[164] Muskhelishvili, N. I., 1953 Some basic problems of the mathematical theory of elasticity: fundamental equations, plane theory of elasticity, torsion, and bending 3rd ed/ Translated from the Russian by J. R. M. Radok, Groningen : P. Noordhoff

[165] Xie, J., Yang, X., Zhou, S., and Wang, D., 2011, "Comparing One- and Two-Dimensional Heteronanostructures As Silicon-Based Lithium Ion Battery Anode Materials," ACS Nano, 5(11), pp. 9225-9231.

[166] Rong, J. P., Masarapu, C., Ni, J., Zhang, Z. J., and Wei, B. Q., 2010, "Tandem Structure of Porous Silicon Film on Single-Walled Carbon Nanotube Macrofilms for Lithium-Ion Battery Applications," ACS Nano, 4(8), pp. 4683-4690.

[167] Biswas, K. G., El Matbouly, H., Rawat, V., Schroeder, J. L., and Sands, T. D., 2009, "Self-Supporting Nanowire Arrays Templated in Sacrificial Branched Porous Anodic Alumina for Thermoelectric Devices," Applied Physics Letters, 95(7), p. 073108.

[168] Rauber, M., Alber, I., Muller, S., Neumann, R., Picht, O., Roth, C., Schokel, A., Toimil-Molares, M. E., and Ensinger, W., 2011, "Highly-Ordered Supportless Three-Dimensional Nanowire Networks with Tunable Complexity and Interwire Connectivity for Device Integration," Nano Letters, 11(6), pp. 2304-2310.

[169] Yao, Y., Huo, K., Hu, L., Liu, N., Cha, J. J., McDowell, M. T., Chu, P. K., and Cui, Y., 2011, "Highly Conductive, Mechanically Robust, and Electrochemically Inactive TiC/C Nanofiber Scaffold for High-Performance Silicon Anode Batteries," ACS Nano, 5(10), pp. 8346-8351.

[170] Kubiak, P., Froschl, T., Husing, N., Hormann, U., Kaiser, U., Schiller, R., Weiss, C. K., Landfester, K., and Wohlfahrt-Mehrens, M., 2011, "TiO(2) Anatase Nanoparticle Networks: Synthesis, Structure, and Electrochemical Performance," Small, 7(12), pp. 1690-1696.

[171] Nishikawa, K., Dokko, K., Kinoshita, K., Woo, S. W., and Kanamura, K., 2009, "Three-dimensionally ordered macroporous Ni-Sn anode for lithium batteries," Journal of Power Sources, 189(1), pp. 726-729.

[172] Liu, C., Li, F., Ma, L.-P., and Cheng, H.-M., 2010, "Advanced Materials for Energy Storage," Advanced Materials, 22(8), pp. E28-E62.

[173] Nelson, R. F., 2000, "Power requirements for batteries in hybrid electric vehicles," Journal of Power Sources, 91(1), pp. 2-26.

[174] Shaijumon, M. M., Perre, E., Daffos, B., Taberna, P.-L., Tarascon, J.-M., and Simon, P., 2010, "Nanoarchitectured 3D Cathodes for Li-Ion Microbatteries," Advanced Materials (Weinheim, Germany), 22(44), pp. 4978-4981.

[175] Cheah, S. K., Perre, E., Rooth, M., Fondell, M., Hårsta, A., Nyholm, L., Boman, M., Gustafsson, T. r., Lu, J., Simon, P., and Edström, K., 2009, "Self-Supported Three-Dimensional Nanoelectrodes for Microbattery Applications," Nano Letters, 9(9), pp. 3230-3233.

[176] Zhang, H., and Braun, P. V., 2012, "Three-Dimensional Metal Scaffold Supported Bicontinuous Silicon Battery Anodes," Nano Letters, 12(6), pp. 2778-2783.

[177] Tian, M., Wang, W., Wei, Y., and Yang, R., 2012, "Stable high areal capacity lithium-ion battery anodes based on three-dimensional Ni–Sn nanowire networks," Journal of Power Sources, 211(0), pp. 46-51.

[178] Wang, W., Tian, M., Abdulagatov, A., George, S. M., Lee, Y.-C., and Yang, R., 2012, "Three-Dimensional Ni/TiO2 Nanowire Network for High Areal Capacity Lithium Ion Microbattery Applications," Nano Letters, 12(2), pp. 655-660.

[179] Yoon, J. C., Lee, J. S., Kim, S. I., Kim, K. H., and Jang, J. H., 2013, "Three-Dimensional Graphene Nano-Networks with High Quality and Mass Production Capability via Precursor-Assisted Chemical Vapor Deposition," Scientific Reports, 3.

[180] Sui, Y. C., González-León, J. A., Bermúdez, A., and Saniger, J. M., 2001, "Synthesis of multi branched carbon nanotubes in porous anodic aluminum oxide template," Carbon, 39(11), pp. 1709-1715.

[181] Jung, Y. S., Cavanagh, A. S., Riley, L. A., Kang, S. H., Dillon, A. C., Groner, M. D., George, S. M., and Lee, S. H., 2010, "Ultrathin Direct Atomic Layer Deposition on Composite Electrodes for Highly Durable and Safe Li-Ion Batteries," Advanced Materials (Weinheim, Germany), 22(19), pp. 2172-+.

[182] Abdulagatov, A. I., Yan, Y., Cooper, J. R., Zhang, Y., Gibbs, Z. M., Cavanagh, A. S., Yang, R. G., Lee, Y. C., and George, S. M., 2011, "Al2O3 and TiO2 Atomic Layer Deposition on Copper for Water Corrosion Resistance," ACS Applied Materials & Interfaces, 3(12), pp. 4593-4601.

[183] Huang, Y., Pandraud, G., and Sarro, P. M., 2013, "Characterization of low temperature deposited atomic layer deposition TiO[sub 2] for MEMS applications," Journal of Vacuum Science & Technology A: Vacuum, Surfaces, and Films, 31(1), pp. 01A148-148.

[184] Schmidt, M., Heider, U., Kuehner, A., Oesten, R., Jungnitz, M., Ignat'ev, N., and Sartori, P., 2001, "Lithium fluoroalkylphosphates: a new class of conducting salts for electrolytes for high energy lithium-ion batteries," Journal of Power Sources, 97–98(0), pp. 557-560.

[185] Dudley, J. T., Wilkinson, D. P., Thomas, G., LeVae, R., Woo, S., Blom, H., Horvath, C., Juzkow, M. W., Denis, B., Juric, P., Aghakian, P., and Dahn, J. R., 1991, "Conductivity of electrolytes for rechargeable lithium batteries," Journal of Power Sources, 35(1), pp. 59-82.

[186] Dees, D. W., Gallagher, K. G., Abraham, D. P., and Jansen, A. N., 2013, "Electrochemical Modeling the Impedance of a Lithium-Ion Positive Electrode Single Particle," Journal of the Electrochemical Society, 160(3), pp. A478-A486.

[187] Chung, S. Y., Bloking, J. T., and Chiang, Y. M., 2002, "Electronically conductive phospho-olivines as lithium storage electrodes," Nature Materials, 1(2), pp. 123-128.

[188] Fabregat-Santiago, F., Mora-Seró, I., Garcia-Belmonte, G., and Bisquert, J., 2002, "Cyclic Voltammetry Studies of Nanoporous Semiconductors. Capacitive and Reactive Properties of Nanocrystalline TiO2 Electrodes in Aqueous Electrolyte," The Journal of Physical Chemistry B, 107(3), pp. 758-768.

[189] Liang, H., Chen, F., Li, R., Wang, L., and Deng, Z., 2004, "Electrochemical study of activated carbon-semiconducting oxide composites as electrode materials of double-layer capacitors," Electrochimica Acta, 49(21), pp. 3463-3467.

[190] Chen, X., and Mao, S. S., 2007, "Titanium Dioxide Nanomaterials: Synthesis, Properties, Modifications, and Applications," Chemical Reviews (Washington, DC, United States), 107(7), pp. 2891-2959.

[191] Yang, Z., Du, G., Guo, Z., Yu, X., Chen, Z., Guo, T., and Liu, H., 2011, "TiO2(B)@carbon composite nanowires as anode for lithium ion batteries with enhanced reversible capacity and cyclic performance," Journal of Materials Chemistry, 21(24), pp. 8591-8596.

[192] Moriguchi, I., Shono, Y., Yamada, H., and Kudo, T., 2008, "Colloidal Crystal-Derived Nanoporous Electrode Materials of Cut SWNTs-Assembly and TiO2/SWNTs Nanocomposite†," The Journal of Physical Chemistry B, 112(46), pp. 14560-14565.

[193] He, L., Ma, R., Du, N., Ren, J., Wong, T., Li, Y., and Lee, S. T., 2012, "Growth of TiO2 nanorod arrays on reduced graphene oxide with enhanced lithium-ion storage," Journal of Materials Chemistry, 22(36), pp. 19061-19066.

[194] Park, S. J., Kim, Y. J., and Lee, H., 2011, "Synthesis of carbon-coated TiO_2 nanotubes for high-power lithium-ion batteries," Journal of Power Sources, 196(11), pp. 5133-5137.

[195] Wei, W., Oltean, G., Tai, C.-W., Edstrom, K., Bjorefors, F., and Nyholm, L., 2013, "High energy and power density TiO2 nanotube electrodes for 3D Li-ion microbatteries," Journal of Materials Chemistry A, 1(28), pp. 8160-8169.

[196] Ryu, W.-H., Nam, D.-H., Ko, Y.-S., Kim, R.-H., and Kwon, H.-S., 2012, "Electrochemical performance of a smooth and highly ordered TiO2 nanotube electrode for Li-ion batteries," Electrochimica Acta, 61(0), pp. 19-24.

[197] Liu, D., Zhang, Y., Xiao, P., Garcia, B. B., Zhang, Q., Zhou, X., Jeong, Y.-H., and Cao, G., 2009, "TiO2 nanotube arrays annealed in CO exhibiting high performance for lithium ion intercalation," Electrochimica Acta, 54(27), pp. 6816-6820.

[198] Shen, L., Li, H., Uchaker, E., Zhang, X., and Cao, G., 2012, "General Strategy for Designing Core–Shell Nanostructured Materials for High-Power Lithium Ion Batteries," Nano Letters, 12(11), pp. 5673-5678.

[199] Yiping, T., Xiaoxu, T., Guangya, H., Huazhen, C., and Guoqu, Z., 2012, "Synthesis of dense nanocavities inside TiO2 nanowire array and its electrochemical properties as a three-dimensional anode material for Li-ion batteries," Electrochimica Acta, 78(0), pp. 154-159.

[200] Hyun-Woo, S., Duk Kyu, L., In-Sun, C., Kug Sun, H., and Dong-Wan, K., 2010, "Facile hydrothermal synthesis of porous TiO 2 nanowire electrodes with high-rate capability for Li ion batteries," Nanotechnology, 21(25), p. 255706.

[201] Anji Reddy, M., Pralong, V., Varadaraju, U. V., and Raveau, B., 2008, "Crystallite Size Constraints on Lithium Insertion into Brookite TiO2," Electrochemical and Solid-State Letters, 11(8), pp. A132-A134.

[202] Wang, K., Wei, M., Morris, M. A., Zhou, H., and Holmes, J. D., 2007, "Mesoporous Titania Nanotubes: Their Preparation and Application as Electrode Materials for Rechargeable Lithium Batteries," Advanced Materials, 19(19), pp. 3016-3020.

[203] Xiong, H., Yildirim, H., Shevchenko, E. V., Prakapenka, V. B., Koo, B., Slater, M. D., Balasubramanian, M., Sankaranarayanan, S. K. R. S., Greeley, J. P., Tepavcevic, S., Dimitrijevic, N. M., Podsiadlo, P., Johnson, C. S., and Rajh, T., 2011, "Self-Improving Anode for Lithium-Ion Batteries Based on Amorphous to Cubic Phase Transition in TiO2 Nanotubes," The Journal of Physical Chemistry C, 116(4), pp. 3181-3187.

[204] Borghols, W. J. H., Lützenkirchen-Hecht, D., Haake, U., Chan, W., Lafont, U., Kelder, E. M., van Eck, E. R. H., Kentgens, A. P. M., Mulder, F. M., and Wagemaker, M., 2010, "Lithium Storage in Amorphous TiO2 Nanoparticles," Journal of The Electrochemical Society, 157(5), pp. A582-A588.

[205] Chunmei, B., Ming, X., Xiang, S., Jonathan, J. T., Gongkai, W., Hongtao, S., Anne, C. D., Jie, L., and Steven, M. G., 2013, "Atomic layer deposition of amorphous TiO 2 on graphene as an anode for Li-ion batteries," Nanotechnology, 24(42), p. 424002.

[206] Xu, J., Jia, C., Cao, B., and Zhang, W. F., 2007, "Electrochemical properties of anatase TiO2 nanotubes as an anode material for lithium-ion batteries," Electrochimica Acta, 52(28), pp. 8044-8047.

[207] Sun, X. D., Ma, C. L., Wang, Y. D., and Li, H. D., 2004, "Al 13 -pillared anatase TiO 2 as a cathode for a lithium battery," Nanotechnology, 15(11), p. 1535.

[208] Ortiz, G. F., Hanzu, I., Djenizian, T., Lavela, P., Tirado, J. L., and Knauth, P., 2008, "Alternative Li-Ion Battery Electrode Based on Self-Organized Titania Nanotubes," Chemistry of Materials, 21(1), pp. 63-67.

[209] Rahman, M. M., Wang, J.-Z., Hassan, M. F., Wexler, D., and Liu, H. K., 2011, "Amorphous Carbon Coated High Grain Boundary Density Dual Phase Li4Ti5O12-TiO2: A Nanocomposite Anode Material for Li-Ion Batteries," Advanced Energy Materials, 1(2), pp. 212-220.

[210] Wagemaker, M., Kearley, G. J., van Well, A. A., Mutka, H., and Mulder, F. M., 2002, "Multiple Li Positions inside Oxygen Octahedra in Lithiated TiO2 Anatase," Journal of the American Chemical Society, 125(3), pp. 840-848.

[211] Wang, D., Choi, D., Yang, Z., Viswanathan, V. V., Nie, Z., Wang, C., Song, Y., Zhang, J.-G., and Liu, J., 2008, "Synthesis and Li-Ion Insertion Properties of Highly Crystalline Mesoporous Rutile TiO2," Chemistry of Materials, 20(10), pp. 3435-3442.

[212] Zhang, L., Zhang, F., Yang, X., Long, G. K., Wu, Y. P., Zhang, T. F., Leng, K., Huang, Y., Ma, Y. F., Yu, A., and Chen, Y. S., 2013, "Porous 3D graphene-based bulk materials with exceptional high surface area and excellent conductivity for supercapacitors," Scientific Reports, 3, p. 1408.

[213] Wang, D. H., Choi, D. W., Li, J., Yang, Z. G., Nie, Z. M., Kou, R., Hu, D. H., Wang, C. M., Saraf, L. V., Zhang, J. G., Aksay, I. A., and Liu, J., 2009, "Self-Assembled TiO2-Graphene Hybrid Nanostructures for Enhanced Li-Ion Insertion," ACS Nano, 3(4), pp. 907-914.